Advanced Eddy Current and Hysteresis Loss Models for Steel Laminations of Rotating Electrical Machines

submitted as doctoral dissertation for obtaining the
academic degree of doctor of technical sciences
at the Graz University of Technology

by

Paul Handgruber

Supervisor/First reviewer: Prof. Oszkár Bíró
Second reviewer: Prof. Anouar Belahcen

Graz, 2015

Acknowledgements

This work has been carried out in the Christian Doppler Laboratory for Multiphysical Simulation, Analysis and Design of Electrical Machines at the Graz University of Technology between January 2011 and December 2014. At this point, I would like to thank all who supported me over the years.

First of all, I am most grateful to my supervisor Prof. Oszkár Bíró for his constructive guidance, devoted expertise, and continuous encouragement.

My deepest thanks go to all my colleagues form the Christian Doppler Laboratory and the Institute of Fundamentals and Theory in Electrical Engineering, for creating a warm and stimulating working environment and turning the years in the laboratory into an unforgettable time.

Thanks are also due to the team of the ELIN Motoren GmbH, in particular to Dr. Georg Ofner, who initiated this work, and to Dr. Andrej Stermecki for their decisive support and invaluable friendship.

Abroad, I would like to express my gratitude to the research team at the Department of Electrical Engineering and Automation at the Aalto University in Finland, where I worked from April 2011 to July 2011. Special thanks go to Prof. Anouar Belahcen for making my stay possible and for acting as a second reviewer. I am also indebted to Dr. Emad Dlala for sharing knowledge and interest by today.

I also gratefully acknowledge the financial support by the ELIN Motoren GmbH and the Christian Doppler Research Association (CDG).

I thank my family and friends for their constant help throughout my study years. Finally, I wish to thank Kathi for her patience, love and moral support.

Abstract

The development of energy efficient electrical machines requires accurate knowledge of the loss components already in the design stage. This thesis contributes to an improved iron loss estimation in the ferromagnetic steel laminations by developing novel numerical methods to deal with eddy current and hysteresis effects.

The presented eddy current model employs finite element methods to consider the three-dimensional current distribution in the steel sheets. Its computational efficiency is ensured by the separate treatment of the individual sheets combined with a harmonic decomposition method to bypass the original transient problem. The hysteresis losses are obtained from a vector Preisach model which has been generalized to anisotropic material characteristics by modifying its input projection. Both models are identified and validated against experimental hysteresis loops as well as iron loss measurements carried out on slip-ring induction machines. Compared to conventional methods, the introduced models have proven to accurately reproduce the measured results in a reliable and efficient manner.

Furthermore, some additional iron losses emerging under practical working conditions are investigated by applying and extending the methods proposed. Special attention is given first to the effects of loaded operation and the axial loss variation in skewed machines. Then, the loss characteristics under different inverter supply conditions as well as the effects of interlaminar short circuits are addressed in detail.

Keywords: eddy currents, electric machines, electromagnetic modeling, finite element methods, magnetic anisotropy, magnetic hysteresis, magnetic losses, magnetic materials, manufacturing processes, rotating machines

Kurzfassung

Erweiterte Wirbelstrom- und Hysteresemodelle für Elektrobleche in rotierenden elektrischen Maschinen

Die Entwicklung energieeffizienter elektrischer Maschinen erfordert bereits in der Auslegungsphase genaue Kenntnis der beteiligten Verlustkomponenten. Als Beitrag für eine verbesserte Eisenverlustberechnung in Elektroblechen werden in dieser Arbeit neue Methoden zur numerischen Analyse von Wirbelstrom- und Hystereseeffekten vorgestellt.

Das entwickelte Wibelstrommodell berücksichtigt die dreidimensionalen Stromverteilung in den Blechen unter Anwendung der Methode der finiten Elemente. Dabei garantiert die getrennte Behandlung der Einzelbleche, kombiniert mit einer Frequenzzerlegung des urprünglich transienten Problems, hohe rechentechnische Effizienz. Die Berechnung der Hystereseverluste erfolgt anhand eines vektorisierten Preisach-Modells, das zusätzlich um anisotrope Materialeigenschaften erweitert wurde. Die anisotrope Erweiterung basiert auf einer verallgemeinerten Projektion der vektoriellen Eingangsgrößen. Die Identifikation und Validierung beider Modelle erfolgt mit Hilfe von experimentell ermittelten Hysteresekurven sowie Eisenverlustmessungen für Asynchronmaschinen mit Schleifringläufer. Verglichen mit konventionellen Methoden, erlauben die präsentierten Modelle eine hochgenaue und zuverlässige Verlustbestimmung bei vergleichsweise geringem numerischen Aufwand.

Die vorgestellten Methoden werden anschließend zur Untersuchung von Zusatzverlusten unter praktischen Betriebsbedingungen verwendet und entsprechend erweitert. Besonderes Augenmerk liegt dabei zunächst auf den Auswirkungen des Lastbetriebes und der axialen Änderung der Verlustverteilung in geschrägten Maschinen. Des Weiteren werden auch das Verlustverhalten bei Umrichterspeisung sowie die Auswirkungen interlaminarer Kurzschlüsse im Detail diskutiert.

Schlagwörter: Wirbelströme, elektrische Maschinen, elektromagnetische Modellierung, finite Elemente Methoden, magnetische Anisotropie, magnetische Hysterese, magnetische Verluste, magnetische Materialien, Herstellungsprozesse, rotierende Maschinen

Statutory Declaration

I declare that I have authored this thesis independently, that I have not used other than the declared sources/resources and that I have explicitly marked all material which has been quoted either literally or by content from the used sources. The text document uploaded to TUGRAZonline is identical to the present doctoral dissertation.

Eidesstattliche Erklärung

Ich erkläre an Eides statt, dass ich die vorliegende Arbeit selbstständig verfasst, andere als die angegebenen Quellen/Hilfsmittel nicht benutzt und die den benutzten Quellen wörtlich und inhaltlich entnommenen Stellen als solche kenntlich gemacht habe. Das in TUGRAZonline hochgeladene Textdokument ist mit der vorliegenden Dissertation identisch.

Graz, ...

Signature

Contents

1 Introduction

With the steadily growing demand for electricity, electrical machines have become an integral part of our everyday life. On the consumption side, electric motor driven systems are the single largest end user of electricity accounting for about 45% of the global electricity consumption [1]. On the production side, electric generators provide almost exclusively the total electricity demand, whereby conventional generation units are increasingly sustained by decentralized renewable energy sources. Besides rotating electrical machines, stationary transformers are extensively used in electronic products and in the electric power distribution system, allowing for an efficient reduction of the transmission costs.

In all areas of application, systems operated by electrical machines offer large potentials for ecological and economical savings. On the one hand, the efficiency of the overall system can be significantly improved by using intelligent control systems, such as variable speed drives. On the other hand, advances in new technologies enable optimization possibilities for the machine design itself.

Despite the technological advances made, the design and manufacture of electrical machines remains one of the most challenging engineering tasks in modern industry. Their growing variety in applications accompanied by strict specifications lead to interdisciplinary problems involving electromagnetic, thermal, mechanical and chemical objectives. Within this multiphysical context, the development of energy efficient electrical machines constitutes a primary design goal, manifested in increasingly tightened efficiency requirements [2–5].

Developing highly efficient machines necessitates detailed information about the loss mechanisms involved. Aside from the mechanical losses due to friction or windage, a major part of the losses is of electromagnetic origin. According to their local occurrence, the emerging electromagnetic losses can be classified in resistive losses in the windings, iron losses in the core stacks, and additional losses in complementary construction parts. Due to the complicated geometrical structure, non-linear material behavior and partially interacting loss phenomena, the accurate prediction of losses still remains a difficult problem.

Owing to the fast development of computational resources in the past decades, numerical simulations are being used in an interdisciplinary way in the design process of electrical machinery. Regarding the electromagnetic design, the finite element analysis is nowadays a state-of-the-art tool. The basic field distribution in the machine is generally obtained by a two-dimensional (2-D) cross-sectional finite element analysis performed in the time or frequency domain. Most of the standard tools enable coupling of the field equations to an

external electrical circuit, the magnetic non-linearity of the iron core is usually considered by a non-hysteretic magnetization curve. More specific analyses employ three-dimensional (3-D) models allowing for an accurate evaluation of parasitic effects arising in the complex geometries.

Even though numerical methods readily enable to predict the operational performance of electrical machines, the exact determination of losses can rarely be achieved by standard numerical procedures. In particular, the assessment of the iron losses in the steel laminations of the core stacks is potentially exposed to considerable uncertainties. The complicated flux patterns arising make the associated eddy current, hysteresis and excess effects difficult to characterize, hindering the development of adequate iron loss models. Mostly, the complex problem is reduced to a simplified one by postprocessing the magnetic field solution and using predefined specific loss curves or analytical approaches. Although these techniques are believed to give reasonable results for specific applications and operating regimes, their limitations and shortcomings are generally acknowledged.

The limits of the simplified approaches are rapidly reached if they are applied to the core loss estimation of induction machines. The small air-gap of this machine type leads, in combination with the teeth structure, to slotting fields characterized by high frequencies and amplitudes. On the one hand, the high-order harmonics induce significant eddy currents. On the other, harmonics give rise to minor hysteresis loops inside the major loop resulting in additional hysteresis losses. These difficulties become even more severe when the machine is operated in conjunction with a frequency converter. Moreover, guiding magnetic flux in iron cores implies the emergence of fields which are rotating in space. In induction machines, rotational fields are primarily present in the tooth roots and the tooth tips of the laminations. The hysteresis losses under rotational flux differ from those under alternating fields requiring an extension of the scalar models.

For the reasons stated above, enhanced methods for the core loss estimation in general, and for induction machines in particular, are attracting academic and industrial interest. This thesis aims to contribute to this field by focusing on advanced methods for the eddy current as well as the hysteresis loss computation. The developed methods are applied to the loss prediction of induction machines, but can be utilized generally with any other topology of rotating electrical machines. The identification and validation of the new methods is continuously supported by experimental results.

1.1 Aim and focus of the work

The main objective of this thesis is to develop advanced iron loss models, which are intended to enable an accurate prediction of the efficiency of electrical machines. Numerical methods to simulate the two main iron loss components, namely the eddy current and hysteresis losses, are presented.

A main part of this thesis deals with 3-D eddy current models for steel laminations of rotating electrical machines. In most approaches known from literature, the effects of eddy currents are evaluated using simplified analytical methods, for instance the statistical loss theory [6]. More enhanced methods employ 3-D homogenization techniques or one-dimensional (1-D) lamination models. To overcome the restrictions of the simplified approaches, a new method to account for the true 3-D eddy current distribution in the sheets is developed.

In addition to the eddy current model, a hysteresis loss model proposed by others has been developed further. The approach is based on a vector Preisach model worked out previously, and has been extended in order to consider anisotropic material properties. The hysteresis model is identified and validated by means of measurements performed on a rotational single sheet tester.

The presented eddy current and hysteresis models are applied to the loss estimation of induction machines. After validating the models against no load iron loss measurements, the effects of loading in a skewed machine are investigated. Furthermore, the additional losses caused by inverter supply as well as interlaminar short circuits will be addressed.

Throughout this work, the loss models are implemented as a postprocessing method fed by a transient 2-D cross-sectional field analysis. Investigations in literature and the experience of the author have shown that, for machines with an air-gap, both the operational behavior and the loss computation itself are only marginally influenced by the losses.

1.2 Scientific contributions

The scientific contributions of this work are listed below. They summarize the main findings made in the publications [P1–P11], but also include some unpublished results.

- A finite element method to compute the 3-D eddy current distribution in steel laminations of electrical machines is developed and applied to the loss computation of slip-ring induction machines. The proposed method avoids full transient 3-D simulations of the whole machine by exciting the 3-D sheet models separately with boundary conditions obtained from a 2-D field analysis. The eddy current losses obtained by the 3-D model are compared to two simplified loss models and validated against no load iron loss measurements. These findings have been presented first at a conference [P1] and then published in [P2].
- Regarding hysteresis modeling, a vector Preisach hysteresis model known from literature is extended in order to simulate weak anisotropy present in non-oriented magnetic steel. The anisotropic material properties are incorporated by generalizing the input projection of the vector model. The generalization improves the rotational loss properties at saturation which are not satisfied properly by the original model. This work has been presented at a scientific meeting [P3] and published in [P4] in-

volving a discussion on the model identification and validation using measurements performed on a rotational single sheet tester.

- The time-stepping procedure of the 3-D eddy current model still exhibits the drawback of high computational costs, since the high frequencies require a dense mesh and sufficiently small time step sizes. In order to reduce the numerical burden, a frequency domain decomposition method has been introduced at a conference [P5] and published in [P6]. Thereby, the cumbersome non-linear transient 3-D simulation is successfully bypassed by solving a few linear time-harmonic problems and superimpose their solutions. The method is further used for studying the eddy current losses under different loading conditions.
- In [P7] and [P8], the developed methods have been applied to a skewed induction machine by coupling the loss models to a multi-slice machine model. It is found that, under load, skewing leads to a highly non-uniform iron loss distribution along the machine length. Compared to a machine with straight rotor bars, the sum of iron and copper losses increases slightly in the skewed machine.
- The conference contribution of [P9] has studied the effects of inverter supply on the machine's iron loss characteristics. Inverter supply on the stator side, as well as a doubly fed operating mode with rotor-sided inverter, are investigated. Under stator-sided inverter supply, the eddy current losses in the steel sheets do considerably increase when compared to sinusoidal feeding, contributing to a total iron loss increment of 10 % to 15 %. In doubly fed operation, the additional losses are generally lower owing to the winding topology of the machine studied.
- The capabilities of the 3-D eddy current model have been further extended in [P10] and [P11] to study the effects of interlaminar short circuits. In avoidance of full models consisting of multiple short circuited laminations, only a single sheet is considered and the interlaminar interaction is taken into account by boundary conditions on the contact surface. The interlaminar contact model allows a quantification of the additional losses due to interlaminar short circuits and has shown that especially shearing burrs occurring on the tooth edges can lead to a significant loss increase.

1.3 Collaborations with third parties

The methods presented in the contributions [P1–P11], and summarized in this thesis, were developed by the first author of those publications. The work was continuously supported by Prof. Oszkár Bíró through his expertise in finite element modeling. From outside the laboratory, various parties were jointly involved.

The industrial partner ELIN Motoren GmbH provided experimental data on the iron losses of the induction machines as well as data on the electrical steel used. Further, Dr. Georg Ofner and Dr. Andrej Stermecki collaborated closely with the author by contributing discussions and comments.

Prof. Anouar Belahcen and Dr. Emad Dlala from the Department of Electrical Engineering and Automation at the Aalto University in Finland supported the author in the early stage of his research. Dr. Dlala introduced the author into hysteresis modeling and provided the initial code for the vector Preisach model.

In collaboration with Mr. Viktor Goričan from Faculty of Electrical Engineering and Computer Science at the University of Maribor in Slovenia, measurements on a rotational single sheet tester have been carried out. The measurement results are employed to identify and validate the proposed hysteresis models.

1.4 Structure of the work

This thesis is subdivided into nine chapters. The current chapter has given a brief introduction by outlining the motivation of this work. The main objectives as well as the scientific contributions made have been emphasized.

Chapter 2 reviews relevant literature concerning eddy current and hysteresis loss modeling in electrical steel laminations. Special attention is given to additional losses caused by loading and skewing effects, inverter supply as well as interlaminar faults.

Fundamentals on losses in ferromagnetic materials, finite element methods and Preisach hysteresis modeling are discussed in chapter 3 by taking into consideration typical challenges encountered during modeling of rotating electrical machines.

The developed 3-D eddy current model for steel laminations is presented in chapter 4. The 3-D model is applied to a slip-ring induction machine and compared to simplified eddy current models as well as no load iron loss measurements.

Chapter 5 extends the vector Preisach hysteresis model to anisotropic properties and discusses the parameter identification for static and dynamic conditions. Furthermore, the effects of rotational fields on the machine's iron loss distribution are subjected to an in-depth analysis.

The variation of the iron loss characteristics due to loading and skewing is investigated in chapter 6, together with a harmonic decomposition method to reduce the computational effort of the transient 3-D eddy current analysis.

Some aspects on additional core losses caused by inverter supply as well as interlaminar short circuits are addressed in the next chapters. Chapter 7 examines different inverter supplied operating modes, while chapter 8 deals with interlaminar short circuits due to shearing burrs and conductive joints.

Chapter 9 gives a conclusion of the work, gathering the scientific achievements made. The key factors for a reliable and efficient iron loss estimation are elaborated and suggestions for future studies are given.

2 Literature review of relevant research

This chapter provides a background study on the topics related to this thesis. Starting with some simplified, experimental iron loss models, advanced methods for the eddy current and hysteresis loss computation will be reviewed. Due to the numerous publications in the related fields it is inconceivable to review them all. Therefore, the focus will be kept on methods which are preferably applied to rotating electrical machines. Moreover, latest achievements in modeling of additional core losses arising under practical working conditions are discussed. Based on the literature review made, a brief conclusion benchmarks the current work.

2.1 Experimental iron loss models

Steinmetz [7] has pioneered work on iron loss modeling by studying hysteretic effects in ferromagnetic laminations exposed to sinusoidal and unidirectionally alternating flux. Based on his experiments, he expressed the iron losses as a power function of the amplitude of the flux density $\hat{B}$ and the fundamental frequency f_s

$$P_{\mathrm{Fe}} = k f_s^{\alpha} \hat{B}^{\beta}. \tag{2.1}$$

The coefficients k, α and β are obtained by fitting the loss model to experimental data. By today, the original Steinmetz equation has undergone several modifications, for example to consider arbitrary flux density waveforms [8, 9], dc bias [10], or minor loops [11].

Based on Steinmetz' approach, two-component methods have been developed in [12] and [13], by splitting the total losses into contributions originating from hysteresis, P_{hys}, and eddy current effects. The statistical loss theory introduced by Bertotti [14], segregates the eddy current losses further into a classical part P_{cl} and an excess part P_{ex}, leading to the following three term expression

$$P_{\mathrm{Fe}} = P_{\mathrm{hys}} + P_{\mathrm{cl}} + P_{\mathrm{ex}} = c_{\mathrm{hys}} f_s \hat{B}^2 + c_{\mathrm{cl}} f_s^2 \hat{B}^2 + c_{\mathrm{ex}} f_s^{1.5} \hat{B}^{1.5}. \tag{2.2}$$

The parameters c_{hys}, c_{hys} and c_{ex} are material specific constants. Assuming sinusoidal excitation and uniform flux density distribution along the lamination thickness d, c_{cl} becomes $c_{\mathrm{cl}} = \sigma \pi^2 d^2/6$, wherein σ is the electrical conductivity of the sheet material [15]. The hysteresis losses originate from the hysteretic character of the magnetization process in

ferromagnetic materials. Contrary to the eddy current and excess effects, the hysteresis losses are static in nature, since the energy dissipated during magnetization is independent of the rate of the applied field. The classical losses are obtained from eddy current analysis on a homogenous conductive body without domain structure, whereas the excess losses account for microscopic local eddy currents caused by domain wall motion. In Bertotti's theory, the excess losses are also compensating for the skin effect at high frequencies, which is neglected in the classical term.

Bertotti's equation (2.2) has been derived for sinusoidally alternating flux. However, in magnetic cores of rotating electrical machines, the discrete winding distribution, slotting and saturation effects possibly combined with non-sinusoidal supply conditions, lead to distorted fields. In [16], the statistical loss theory has been extended for arbitrary flux waveforms by considering the time derivative of the magnetic flux density B

$$P_{\mathrm{Fe}} = P_{\mathrm{hys}} + \frac{c_{\mathrm{cl}}}{T}\int_0^T \left(\frac{\mathrm{d}B}{\mathrm{d}t}\right)^2 \mathrm{d}t + \frac{c_{\mathrm{ex}}}{T}\int_0^T \left|\frac{\mathrm{d}B}{\mathrm{d}t}\right|^{1.5} \mathrm{d}t, \tag{2.3}$$

in which t is time, and T is the time period of the fundamental frequency. Using this representation, one should note that $c_{\mathrm{cl}} = \sigma d^2/12$. A common simplification of (2.2) and (2.3) is obtained by superposition of the losses for each harmonic component

$$P_{\mathrm{Fe}} = \sum_{i=1}^{N_{\mathrm{h}}} \left(c_{\mathrm{hys}} i f_s \hat{B}_i^2 + c_{\mathrm{cl}} (i f_s \hat{B}_i)^2 + c_{\mathrm{ex}} (i f_s \hat{B}_i)^{1.5}\right) \tag{2.4}$$

where $\hat{B}_i$ is the amplitude of the ith harmonic of the flux density and N_{h} is the number of harmonics considered. Hereinafter, the model defined by (2.4) will be referred to as the traditional technique and will be compared to the advanced methods developed in this thesis.

The statistical loss separation theory has been further improved by taking into account the skin effect for higher frequencies [17], minor hysteresis loops [13, 18], or even by substituting the loss coefficients with flux- or frequency-dependent polynomials [19].

In general design practice of electrical machinery, the discussed empirical or semi-empirical models are employed a posteriori to the 2-D finite element solution. A first application of Bertotti's statistical loss theory has been presented in [20] by feeding the flux density distribution of a brushless dc motor element-wise to the loss model. In [21], five different statistical loss models have been compared to each other. None of the models has been found to be superior when adopted to the loss estimation of a permanent magnet synchronous motor.

Mostly, the losses are evaluated independently for each Cartesian component of the flux density, neglecting the rotational hysteretic behavior. Experiments have shown that the hysteresis losses under rotational excitation differ from those under alternating conditions

[22–24]. At low and medium flux densities, the rotational losses can be significantly higher than in the alternating case, until they start to decrease quickly near saturation. For instance, in induction machines, rotational fields do occur in the stator tooth roots and in tooth tips of the sheets. In order to account for rotational effects, the hysteresis losses have been modified by some correcting factors obtained from comparison of loss measurements under alternating and circular flux [25,26]. Other works treat the rotational losses separately by means of semi-empirical fitting functions [27–29].

2.2 Eddy current models

Besides the simplified eddy current terms appearing in the experimental models, physical eddy current models have been developed along with the advances made in computational resources. The electromagnetic field quantities in the laminations are thereby evaluated by discretizing Maxwell's equations. In the most general case, the resulting quasistatic eddy current problem is formulated as

$$\nabla \times \left(\frac{1}{\sigma} \nabla \times \boldsymbol{H} \right) = -\frac{\partial \boldsymbol{B}}{\partial t}, \tag{2.5}$$

whereby the flux density vector $\boldsymbol{B}$ is coupled through constitutive material relations to the magnetic field intensity $\boldsymbol{H}$.

2.2.1 Homogenization methods

The most common technique in dealing with laminated structures is to assume a bulk medium having anisotropic material properties. For instance in [30], the electric conductivity has been set to zero in the direction normal to the laminations, and the magnetic permeability has been modified according to the stacking factor. Instead of using anisotropic material quantities, a single component current vector potential has been introduced in [31] to consider the laminar character of the current density. This latter technique is not valid for any field formulation and restricted to a single orientation of the sheets within the stack.

The methods mentioned account only for the planar eddy currents caused by the flux density perpendicular to the sheets. Regarding studies on rotating electrical machines, they enable to evaluate the additional core losses due to axial stray fields caused by air-gap fringing and the end winding leakage. Such stray fields are potentially emerging at end regions of the core, where planar eddy currents can induce a significant loss increase accompanied by local overheating. In [32], the losses in the stator end region of a turbo-generator have been analyzed for the first time using a homogenized 3-D finite element model. Similar studies have been performed in [33] and [34] along with a thermal analysis for identification of possible hot spots. Recent works have also investigated additional

losses induced in inactive construction parts, such as clamping plates and fingers [35–37], or housing and end shields [38, 39].

In order to consider the eddy current loops confined by the sheet thickness, the homogenized bulk models have been combined with a separate analysis of the individual sheets. In [40], the eddy currents caused by parallel fluxes have been evaluated by analytical expressions. In [41] and [42], the bulk model has been combined with a 1-D eddy current analysis, whereas in [43] the 3-D models of the single laminations have been treated separately by exciting them with boundary conditions obtained from the continuum model.

2.2.2 1-D lamination models

The thickness of the steel sheets used in electrical machines is in general considerably smaller than their transversal dimension. Assuming a magnetic field entering in parallel to the sheets and neglecting the return paths of the eddy currents, the intrinsically 3-D eddy current problem can be approximated by a 1-D diffusion equation. The 1-D formulation has been introduced first in [44] and characterizes the penetration of the flux density along the lamination thickness. In [45], the approach has been extended to 2-D fields by solving the 1-D eddy current problem in each direction separately

$$\frac{\partial^2 H_x(z,t)}{\partial z^2} = \sigma \frac{\partial B_x(z,t)}{\partial t}, \qquad \frac{\partial^2 H_y(z,t)}{\partial z^2} = \sigma \frac{\partial B_y(z,t)}{\partial t}, \tag{2.6}$$

where the subscripts x and y refer to the directions to which the fields correspond to. The one-dimensional nature of the approach consists in evaluating the field quantities along the lamination thickness in z-direction only. The two equations are coupled through BH-relations and possibly also through boundary conditions.

The work of [46] has presented one of the first implementations of a 1-D model applied to the core laminations of an induction machine. The 1-D model has been excited by boundary conditions derived from the 2-D cross-sectional field solution, neglecting the reaction of the 1-D model on the 2-D one. Other applications of 1-D methods to various machine types can be found for instance in [47] and [48]. The coupling between the 2-D and 1-D models has been thoroughly addressed in [49] by utilizing nested iterative schemes. In [50], the latter method has been further extended to consider the interaction between the x- and y-components of the magnetic field via coupling terms in the Jacobian matrix.

Solving the 1-D diffusion equation usually requires a suitable space discretization along the lamination thickness. In order to avoid such a discretization, so-called mesh-free lamination models have been developed recently [51–53]. Thereby, the magnetic flux density is represented by a set of hyperbolic [51, 52] or polynomial [53] basis functions. In [53], the proposed mesh-free approach has been applied first to an induction machine and later, in [54], to a wound-field synchronous machine.

2.2.3 2-D and 3-D lamination models

The application limits of the 1-D approach have been studied in [55], [56] and [57] by comparison to a 2-D eddy current problem excited in z-direction:

$$\frac{\partial^2 H_z(x,y,t)}{\partial x^2} + \frac{\partial^2 H_z(x,y,t)}{\partial y^2} = \sigma \frac{\partial B_z(x,y,t)}{\partial t}. \tag{2.7}$$

All the works have come to the conclusion that the neglection of the edge effects in the 1-D model leads to an overestimation of the losses. The deviations increase with the frequency and the sheet thickness. In [57], it has been stated that the geometrical ratio between the sheet width and the thickness should be higher than 10 for obtaining satisfactory results with the 1-D formulation.

Lately, 3-D models taking account of each laminate have been set up by solving (2.5) in its full extent. Most of them are rather simple and serve as a benchmark basis for the various reduced models [43]. More complex 3-D models for laminated cores of rotating electrical machines have been employed in [58] and [59].

In [58], the 3-D eddy current distribution in a single sheet of an induction machine and a permanent magnet motor has been investigated. The 3-D model has been obtained by extruding the machine's cross section for a half of the sheet thickness. Axial fields have been neglected by setting appropriate boundary conditions. The motion of the rotor in the transient analysis has been considered by re-meshing the air-gap elements.

Moreover, [59] studied the effects of stray fields emerging at the stator core ends of a turbine generator. First, a 3-D non-conductive bulk model of a pole pitch of the end region has been examined using a transient analysis. Then, the time-harmonic 3-D model including each laminate has been analyzed by exciting it with the air-gap flux density derived from the transient analysis. The insulation between the sheets has been taken into account by doubly defined finite element nodes on the lamination surface.

2.3 Hysteresis models

Whereas the numerical treatment of non-linear magnetic material behavior can nowadays be tackled by standard procedures, modeling of hysteretic properties still remains a challenging subject. During the past decades, hysteresis modeling received increased attention manifested in numerous publications. In the following, fruitful approaches to including hysteretic properties in the iron loss analysis of electrical machines are reviewed.

2.3.1 Static hysteresis

Speaking about hysteresis generally implies static hysteretic effects, meaning that the magnetization behavior is rate-independent of the magnetic field applied. Hysteresis loops

are usually measured at low frequencies, for which the dynamic effects of the eddy currents are negligible.

One of the most popular approaches to hysteresis is the Preisach hysteresis model introduced originally in [60], and later interpreted mathematically in [61]. The model is based on a simple rectangular hysteresis operator $\gamma_{h_\alpha,h_\beta}$ defined by up- and down-switching values at h_α, h_β and giving the states ± 1 depending on the current input field $H(t)$. The shape of the hysteresis loop is determined by a Preisach distribution function $\mu(h_\alpha, h_\beta)$ covering all possible field intensity values. The output flux density $B(t)$ is obtained by accumulating the weighted elementary hysteresis operators over a physically meaningful range $h_\alpha \geq h_\beta$:

$$B(t) = \iint\limits_{h_\alpha \geq h_\beta} \mu(h_\alpha, h_\beta)\gamma_{h_\alpha,h_\beta}(H(t))\,\mathrm{d}h_\alpha \mathrm{d}h_\beta. \tag{2.8}$$

The Preisach distribution function is often obtained from an identification procedure based on a Gaussian or Lorentzian distribution [62, 63]. Mayergoyz [64] gave a geometrical interpretation of the classical Preisach model and simplified its numerical implementation and identification by means of Everett functions [65]. Using Everett functions allows a complete model identification with first-order reversal curves and avoids the double integral of (2.8).

The classical Preisach model in its phenomenological nature fulfils some essential features observed in experiments, such as the return-point memory and the wiping-out (deletion) property [66]. The return-point memory implies the closure of the minor hysteresis loops, the wiping-out property states that only the dominant input extrema are stored by the model. Additionally, the model also exhibits the congruency property, entailing that variations between the same two extremal values produce congruent minor loops. However, the congruency property could not be confirmed experimentally. Furthermore, it was observed in experiments that many cycles may be needed before a minor hysteresis loop forms a closed path, while the classical Preisach model immediately produces stable minor loops. Approaches considering the latter phenomenon of accommodation as well as a generalization of the congruency property can be found in [63] and [64].

An interesting alternative to the classical Preisach model has been described in [67]. The elementary hysteresis operators are thereby replaced by a play function. Using a stop-type model represents the inverse Preisach operator. The applicability of play- and stop-type models has been investigated for instance in [68] and [69], concluding that the play-type model predicts the hysteretic properties more accurately than the stop-type one.

In [70] and [71] a so-called history-dependent hysteresis model has been introduced, which is based on direct use of experimentally measured first-order reversal curves. The hysteretic behavior in the overall BH-plane is obtained as a weighted sum of shifted first-order reversal curves. The history-dependent model rigorously fulfills the return-point and wiping-out property, and further relaxes the congruency and accommodation problem.

Another common phenomenological hysteresis model has been proposed by Jiles and Atherton [72]. The Jiles-Atherton model describes the energetic behavior of the magnetic domains analytically. The resulting differential equation is based on an irreversible magnetization component resulting from the pinning effect, and a reversible component ensuing from domain wall bowing. The main advantage of the Jiles-Atherton model lies in its simplicity since it requires only five scalar parameters to be identified. In contrast, the model has been judged to give inaccurate results regarding the wiping-out property and the return-point memory leading to non-realistic minor hysteresis loops [73].

2.3.2 Dynamic hysteresis and excess effects

Only static hysteresis models have been reviewed thus far. The term static refers to the fact that the speed of the input variations has no effect on the shape of the hysteresis loop. However, in ferromagnetic materials, rate-dependent eddy current and excess effects lead to a broadening of the hysteresis loops depending on the rate of change of the magnetic field. The eddy current effects are usually associated with the conductivity of the material, whereas the microscopic excess effects are considered as part of the hysteretic law. Most dynamic hysteresis models are based on a dynamization of static models.

In [64], a dynamic Preisach model has been introduced by enforcing the distribution function to be dependent on the time derivative of the magnetization. Although an in-depth discussion on the identification procedure of the material parameters was given, the model has been found to achieve unsatisfactory agreement with experiments [74].

Another, more successful, dynamic generalization of the scalar Preisach model has been developed by Bertotti [75]. In his model, the dynamic excess effects are modeled by using rate-dependent elementary hysteresis operators whose switching rate is controlled by the input field. The results can be physically interpreted by means of the statistical loss theory [76]. Applications of the dynamic Preisach model of Bertotti can be found in [77], [78] as well as in [79], where the model has been coupled to the 1-D diffusion equation.

The dynamization of the history-dependent model of [70, 71] is derived from the concept of magnetic viscosity and formulated in [80]. The proposed viscous-type differential equation has been proven to give accurate results for a wide range of frequencies, and can be used in general with any other type of static hysteresis model.

The dynamic model of Jiles [81] is based on a linear second-order differential equation describing the motion of the domain walls. Compared to the static model, only two new additional material parameters are introduced specifying the resonance frequency and the damping coefficient of the resulting harmonic motion equation.

2.3.3 Vector hysteresis

Most of the models found in literature and discussed up to now are scalar in nature. However, in electrical machines, the flux patterns are locally rotating rather than unidirectionally alternating. This has led researchers to the development of vector hysteresis models accounting for the hysteretic behavior under rotational magnetization.

One of the first vector hysteresis models to appear was the Stoner-Wohlfarth model [82]. This model is physically based on the theory of particle assemblies consisting of identical particles with uniaxial anisotropy. The Stoner-Wohlfarth approach is generally useful for studying physical processes during magnetization, but fails to reproduce accurate results at a phenomenological level.

A general vector extension, which can be applied principally to any scalar hysteresis model, has been proposed by Mayergoyz [64]. In the Mayergoyz approach, the input field intensity is projected to N_φ discretized directions $\boldsymbol{e}_{\varphi_i}$, with $\varphi_i = {}^{i\pi}/_{N_\varphi}$. The output is obtained by applying the scalar model in each direction and summing up the outputs:

$$\boldsymbol{B}(t) = \sum_{i=1}^{N_\varphi} B[H_{\varphi_i}(t)]\boldsymbol{e}_{\varphi_i}. \tag{2.9}$$

Here, $B[H_{\varphi_i}]$ stands for the scalar Preisach function. Mayergoyz' vector extension of the scalar Preisach model has become widely known as the vector Preisach model and will be referred to as such here too. The vectorization of the scalar models enables to keep track of the input history in each direction. The model is identified so that it produces the same output as the scalar model when magnetized in one direction. Despite its ability to accurately predict hysteresis loops under alternating and circular conditions, the model has been criticized for not reproducing the rotational loss properties experimentally observed. At saturation, the model exhibits an irreversible hysteretic behavior entailing that the losses remain at a constant level instead of decreasing. To overcome this problem, a generalized vector model has been introduced in [83] and [84] by modifying the input projection, or by adjusting the losses using a weighting function [85].

A model that combines features of the Preisach model and the Stoner-Wohlfarth one has been presented in [86] by replacing the classical scalar Preisach function with a vector operator based on Stoner-Wohlfarth asteroids. In [63], the elementary hysteresis operators have been substituted by coupled ellipsoidal hysterons which interact according to predefined selection rules.

In [87] and [88], energy based vector models have been developed, which have similarities to the Prandtl-Ishlinskii hysteresis model [89] established in continuum mechanics. Magnetic hysteresis is thereby represented as a superposition of pseudoparticles whose pinning effect is modeled as a friction-like force. The model intrinsically satisfies vector properties and is well suited to study magnetic dissipation at a macroscopic scale.

Aiming towards a general prediction of the magnetodynamic effects under rotational magnetization, dynamic vector models have been proposed. A simplified and common dynamization of the static models can be achieved by adding dynamic field components to the static ones, neglecting the interaction between static and dynamic contributions [90, 91]. A more enhanced but computationally expensive approach has been studied in [92] and [93] by coupling the static vector Preisach model to the 1-D eddy current equation. Besides the Preisach-type models, a dynamical energy based vector hysteresis model has been introduced in [94] by extending the work of [88].

Considering applications to rotating electrical machines, hysteretic material behavior is usually included using the Preisach theory. One of the first works to employ a static vector Preisach model for the iron loss computation of an induction machine is given in [46]. The vector model is based on the Mayergoyz extension and has been coupled in the postprocessing stage to the 1-D diffusion equation. Other works to follow have been presented in [47] and [95]: in [47], the vector Preisach model of [46] has been extended to include rate-dependent hysteretic properties; in [95], the solution of the diffusion equation has been avoided by introducing a statistical-like eddy current term to the magnetic constitutive law.

A great deal of research on Preisach hysteresis modeling in rotating electrical machines has been carried out by a Finnish research group. In [96], a static vector Preisach model has been elaborated and incorporated into the 2-D finite element analysis of squirrel cage induction machines. The latter method has been extended in [74] by strongly coupling it to a 1-D lamination model and relaxing the rotational loss properties at saturation. Moreover, a simplified magnetodynamic vector hysteresis model has been introduced based on the evaluation of magnetization curves. The model combines the static vector Preisach model with a simplified expression for the dynamic field components, thus avoiding the computationally expensive solution of the 1-D equation.

2.3.4 Anisotropy

The majority of the proposed hysteresis models is inherently isotropic, neglecting any anisotropy effects on the field distribution and the ensuing losses. Besides grain-oriented material, even non-oriented steels can exhibit a certain extent of anisotropy, owing to inevitable crystal orientations during the rolling process.

An intuitive way to address anisotropic effects in electromagnetic finite element analyses is the introduction of an anisotropic reluctivity tensor [97]. The reluctivities are obtained from measurements performed on two-dimensional setups enabling magnetization in different directions. Other approaches are based on the energy/coenergy concept which represents the vectorial BH-relationship with the aid of measurements in the rolling and transverse direction only [98, 99].

Regarding hysteresis modeling, limited attention has been paid to anisotropic behavior. In [83], an anisotropic Preisach hysteresis model has been presented by generalizing the input projection of the vector model. The generalized model considers the effects of biaxial anisotropy exhibiting two perpendicular magnetic easy axes which are equally pronounced.

Modeling of uniaxial anisotropy, defined by a sole magnetic easy axis, into Preisach-type vector models has been studied in [100–105]. In [100], weak anisotropy has been considered by direction-dependent elementary hysteresis operators implemented by means of neural networks. In [101–103], angularly dependent distribution functions have been introduced. Their angular dependence can be handled by Fourier expansion [101, 102] or by assembling them as a product of Lorentzian's functions [103]. A simple anisotropic generalization of a vector play-model has been given in [104] by multiplying the isotropic model with an anisotropy matrix. This work has been extended further in [91] to account for dynamic effects. In [105], the elementary Preisach operator has been replaced by a four-state vector operator which incorporates microcrystalline anisotropy by adopting the Stoner-Wohlfarth theory.

The friction-like hysteresis model of [87] is easily extendable to anisotropy effects since it intrinsically exhibits anisotropic properties. The model identification has been discussed in [106] and [107] by examples of weakly anisotropic non-oriented steel sheets.

2.4 Additional iron losses

In this thesis, special attention is given to additional losses arising under practical working conditions, such as loaded operation or inverter supply. Furthermore, the effects of interlaminar short circuits caused by imperfect sheet insulation will be addressed. These additional losses are in general rather difficult to assess, owing to their complex origin and the lack of reliable measurement methods. In conventional machine design, they are attributed to the so-called stray load losses defined as a global quantity with no insight into the physics of their formation [2–4]. Without focusing on the concept of stray load losses, methods to compute these loss components will be reviewed in the following.

2.4.1 Effects of loading and skewing

The evaluation of iron losses is usually performed under no load conditions due to the feasibility of measurements based on the input-output method. Under load, the conventional input-output method is no longer suitable for studying high efficiency machines, since even small measurement errors in the input and output powers lead to large errors in the results. Better accuracy can be achieved by using rather complicated calorimetric setups which determine the losses from the heat dissipated [108].

In [109] and [110] it has been pointed out that the field harmonics in the iron core of an induction machine considerably increase when load is getting applied. Under load, higher

currents have to be provided, resulting in enlarged field harmonics generated by slotting effects and the winding structure. As observed in [109], in particular the eddy current losses exhibit a significant increase, since they rise approximately quadratically with the frequency.

Further challenges arise when induction machines with skewed rotor bars come into the focus of interest. Skewing is a common practice to reduce torque ripples, harmonic currents, and acoustic noise. On the one hand, the skew reduces high frequency losses in the rotor windings. On the other hand, it has been noted early in [111], that skewing leads to non-uniform flux density distribution along the machine length, which can result in elevated iron losses.

To avoid computationally expensive 3-D analyses, the skew effects are usually taken into account by multi-slice finite element models [112, 113]. Thereby, the electromagnetic quantities are evaluated in several cross-sectional slices at given positions along the machine axis. The currents in the rotor bars of the individual slices are coupled through an external electrical circuit. In [114], a time-harmonic multi-slice method has been employed, combined with a two-term expression for the iron loss estimation. It has been reported that the flux distribution, and thus the losses, may vary considerably depending on the loading condition. The investigations in [115–117] have been performed in the time domain by postprocessing the field solution to fit statistical core loss models. In [116] and [117], a comprehensive study on how the skew alters the balance between decreasing rotor bar losses and increased iron losses has been carried out concluding that in larger machines, where the iron losses become more dominant, the skew results in an overall loss increment.

In addition to the non-uniform field distribution along the machine length, skewing entails the emergence of axial field components. These components lead to planar eddy currents in the laminations and to parasitic inter-bar currents which flow from the rotor bars into the core. The effects of planar eddy currents have been studied in [118] by coupling a homogenized 3-D model to a model of individual laminates. In conclusion it was found that they contribute to negligibly small losses when compared to the eddy currents flowing within the sheet thickness. The effects of inter-bar currents are generally examined by resistance networks [119] or 3-D models [115, 120].

2.4.2 Effects of inverter supply

Owing to the latest progress in power electronics and control systems, variable speed drives are increasingly realized by means of frequency converters. In comparison to conventional sinusoidal supply, the switching operations of the inverter lead to distorted output voltages whose high frequency components induce additional losses in the machine windings and cores. In the past decades, the effects of inverter supply have been studied intensively in several publications, of which the most relevant ones are summarized below.

In [121], the impact of inverter supply on two samples of soft magnetic materials has been investigated experimentally. Under pulse width modulated (PWM) voltage supply, a major increase of the iron losses has been reported, whereby the eddy current losses have been identified to be most sensitive to the inverter output voltage. The measurement results have been compared to numerical studies employing a 1-D lamination model [122]. In [123], the 1-D approach has been coupled with a dynamic Preisach model, but no significant increase of the hysteresis losses has been noticed.

The additional losses in an inverter supplied induction machine have been examined in [124] using a slotless rotor test bench. During PWM feeding, the iron losses rose by 85 % in comparison to sinusoidal supply. The influences of the inverter characteristics on the iron losses have been measured in [125], including PWM supply voltages with different switching frequencies and modulation indices.

The loss computation of inverter fed electrical machines is commonly based on post-processing the transient 2-D field solution to generalized formulations of the statistical theory. The generalizations made are established as empirical relations between the losses under sinusoidal and inverter feeding [17, 126, 127]. For instance, in [128] and [129], these generalized models have been applied to the core loss estimation of an induction motor fed by PWM voltage. While in [128] no validations with measurements have been performed, the computational results of [129] have shown good accuracy for a large number of supply types.

Recently, the effects of inverter supply have been studied by means of more enhanced models allowing for an accurate assessment of the associated eddy current and hysteresis losses. In [130], a 1-D eddy current model combined with a Preisach-type vector model has been used to study an induction machine supplied by a six-step voltage source. This supply type was observed to cause comparatively low additional losses due the few switching operations involved. Moreover, it has been found that the inclusion of eddy current and hysteresis effects into the field solution has a rather small influence on the field patterns and the consequent losses. The works of [131] and [132] have contemporaneously investigated the eddy currents under PWM excitation by using a 1-D model. The model of [131] takes also hysteresis into account by using the notion of complex reluctivity. Other interesting studies on the iron losses of induction machines under PWM supply can be found in [133] and [134]: in [133], a magnetodynamic vector hysteresis model based on the Preisach theory has been utilized, whereas in [134] the hysteresis effects have been studied by a Jiles-Atherton model.

2.4.3 Effects of interlaminar short circuits

Evaluating the influence of manufacturing processes on the magnetic and electric properties of steel laminations is one of the most difficult aspects to assess. In particular, the cutting process substantially degrades the electromagnetic characteristics near the steel edges. Depending on the cutting technique, the degradation process can result in an iron

loss increase by up to 30 % [135, 136]. In the core loss prediction, the effects of cutting are usually addressed by correction factors derived from experiments [25].

The works of [137] and [135] emphasize that commonly utilized punching methods lead to a serious decrease of the magnetic permeability due to the mechanical stress applied. Laser-cutting may even induce a more severe permeability drop owing to thermal strains [138]. The effects of stress on the permeability have been considered in [139] and [140] by introducing a thin finite element layer of low permeability on the cutting edges. Other works take also the effects of the mechanical stress caused by shrink fitting and stamping into account [141, 142]. Lately, measurement and simulation of stress-dependent magnetic material properties have become a topic of considerable interest manifested in various publications documenting ongoing research [143, 144]. In this thesis, no further attention is given to the change of material characteristics during manufacturing. The discussions below are rather focusing on the effects of interlaminar short circuits, which will be analyzed according to their origin of occurrence.

In addition to the degradation of electromagnetic properties, the mechanical deformations during the cutting process result in creation of microscopic shearing burrs on the lamination edges. These edge burrs can break down the insulation leading to conductive connections between the stacked sheets. If the burr-induced short circuits cover several laminations, high currents begin to circulate, resulting in a significant loss increment and hence to local overheating [145]. Mostly, the effects of interlaminar short circuits have been considered by statistical evaluation of measured data [146, 147]. The used measurement setups are for instance based on capacitive methods [147] or employ external flux density sensors [148]. To precisely quantify the additional losses arising, measurement systems allowing for a selective application of artificial burrs have been set up. In [149], edge burrs have been introduced in a controlled manner to a model of a transformer core. Compared to a configuration without burrs, the burr effects have led to an increase of the total losses by about 100 %. In the burr region, the local losses became almost 50 times higher. Similar experiments have been performed in [150] and [151] by using a three-phase transformer core and a clamping device for the application of burrs. The measurement results have also been compared to an analytical eddy current model, but only poor correlation was found due to the simplifications made. In the works of [152] and [153] the interlaminar contacts have been modeled using a resistance network analogy. The investigations in [152] are based on an elementary short circuit comprising two sheet pairs. In [153], the network parameters have been derived from a simple small-scale 3-D finite element model.

Further interlaminar short circuits are caused by conductive joints, such as bolts, welds or clamping bars. In most cases, these fixations as well as the shaft and parts of the frame are mounted uninsulated on the core, short-circuiting a large number of laminations. Although the consequent loss increase is commonly acknowledged in industrial praxis, only a few scientific publications address the effects of conductive joints. The influence of welding joints on a toroidal core has been studied experimentally in [154] and [155]. It has been stated that the iron losses can rise by up to 44% depending on the number of welding passes and the core material.

A third possible cause for interlaminar short circuits are small insulation faults on the lamination surfaces inside the core middle. Such inner short circuits are most likely caused by aging effects combined with high temperature loads. The quality of the surface insulation is normally assessed by measurement of the surface resistance [156]. Because of the stochastic nature of coating faults, they are almost exclusively quantified by statistical means [146, 156].

2.5 Conclusion

This chapter has summarized relevant literature discussing eddy current and hysteresis models as well as additional iron losses emerging under practical working conditions. Despite the recent availability of powerful numerical tools, the estimation of iron losses is still mostly based on simple analytical approaches, for instance the statistical loss theory [6]. Additional losses are commonly considered by correcting factors without having detailed insight into their origin.

The eddy current problem in the steel sheets of electrical machines is usually treated by approximation of Maxwell's equations employing homogenization techniques or 1-D lamination models. However, in small machine parts such as teeth, bridges or closed slots, the effects of the 3-D eddy-current distribution are not negligible, and the methods stated may be no longer valid [57]. These edge effects become particularly important at the tooth tips exposed to high harmonic flux variations [56]. To overcome the restrictions of the homogenization methods and 1-D approaches, a method based on a 3-D finite element analysis is developed in this thesis. Unlike other 3-D models [132,157], the method proposed avoids cumbersome modeling of the rotor movement.

The Preisach model is the most popular hysteresis model in computational electromagnetics. Compared to other models, it offers high accuracy and stability founded on a robust mathematical background. In light of these advantages, a Preisach-type vector hysteresis model is used in this work, too. The used model has originally been proposed by others [64, 74], and is extended by the author to account for weak bi- and uniaxial anisotropies. The new anisotropy model is based on a generalized input projection and omits complicated expansions of the distribution functions, such as implemented in [101] or [102].

It is known from literature that the iron losses of an induction machine increase when load is getting applied. These effects will also be investigated in this thesis. Moreover, the developed eddy current and hysteresis models will be applied to the study of skewing effects having been investigated before by extensions of the statistical loss theory only [115–117].

Recently, the iron loss characteristics under inverter supply have attracted the attention of many researchers and are addressed here, too. Besides the commonly investigated inverter supply on the stator side, a doubly fed operation mode will also be examined. Slip-ring induction machines operated in doubly fed mode are supplied by a frequency

converter on the rotor side. The presented studies on the iron loss properties under rotor-sided inverter supply are new to the knowledge of the author.

The quantification of additional losses due to interlaminar short circuits is mostly performed in the literature using analytical methods derived from simple geometries. In order to enable studies on more complicated structures like an electrical machine, the 3-D eddy current model will be extended in this work by introducing suitable boundary conditions on the interlaminar contact surface. The method is capable of computing the true paths and values of the eddy currents and avoids full models comprising several interconnected sheets.

The developed models are applied in postprocessing manner to the 2-D cross-sectional field solution of the machine. The effects of the inclusion of the iron losses in the field analysis have been mentioned in section 2.4.2 and also studied in [48,158], concluding that for rotating electrical machines, their effects can be neglected without any significant loss of accuracy. Owing to the air-gap present in this machine type, a considerable amount of reactive power is required for the field generation, which in turn significantly attenuates the effects of iron losses. Furthermore, the incorporation of hysteresis and eddy current effects into the field solution implies high computational costs potentially suffering from numerical instability [93, 159]. Bearing these considerations in mind, the effects of iron losses are omitted during the 2-D analysis in favor of an efficient implementation well suited for industrial design purposes.

3 Fundamentals

After introducing some details of the loss generation in ferromagnetic materials, fundamentals of the numerical methods used will be presented in this chapter. The analysis of the electromagnetic field quantities is based on finite element methods, which are reviewed with particular emphasis on eddy current formulations and applications to rotating electrical machines. Moreover, the implementation of the employed Preisach hysteresis model will be detailed, involving a discussion on its identification and extension to rotating fields as well as dynamic conditions.

3.1 Losses in ferromagnetic materials

At a microscopic scale, ferromagnetic materials are frequently characterized using the domain theory [160]. Magnetic domains are regions with uniform magnetization separated by domain walls. When a magnetic field is getting applied, the domains align themselves with the external field. The magnetization process is accompanied by movement of the domain walls and alignment of the magnetic dipole moments. These phenomena are partly irreversible and reflected in the overall hysteretic behavior at macroscopic scale.

Depending on their chemical composition, grain size and the manufacturing process, ferromagnetic materials feature different magnetic properties adapted to specific applications. The magnetically soft ferro-silicon alloys used in electrical machines are easy to magnetize (high permeability) and show low magnetic losses. They can be classified in non-oriented and grain-oriented types. In grain-oriented steel, the domains are selectively aligned in a specific direction using a sequence of annealing and rolling treatments. Consequently, this steel type is characterized by strong anisotropy and rather large grain size. Grain-oriented steel is preferably used in transformers and large-sized rotating machines in which the core is assembled of sectorally segmented sheets. Non-oriented steel shows similar magnetic properties in all directions. Small anisotropies are potentially caused by the domain orientation during the rolling process. Owing to simpler manufacturing and thus lower costs, this steel type is used in a large variety of applications and will also be in the focus of this work.

During the magnetization of a ferromagnetic material, a part of the supplied energy is converted to heat. The associated energy loss during a magnetization cycle is proportional to the area of the hysteresis loop. According to their physical origin and their frequency

dependence, the total iron losses can be subdivided in two main groups, namely the hysteresis and the eddy current losses.

3.1.1 Hysteresis losses

The partially irreversible alignment of the magnetic domains leads to hysteretic behavior, and, thus, to the formation of losses. The hysteresis losses are static, since the energy needed to surpass the irreversible processes is independent of the frequency of the field applied.

Under unidirectionally alternating fields, the hysteresis losses increase steadily with the magnetic flux density until they show saturation tendencies at high values of B (see Fig. 3.1). This is due to the fact that the magnetization process at saturation is chiefly characterised by reversible alignments of the magnetic dipoles. These reversible effects take place hysteresis-free, requiring no energy when changing the magnetic state.

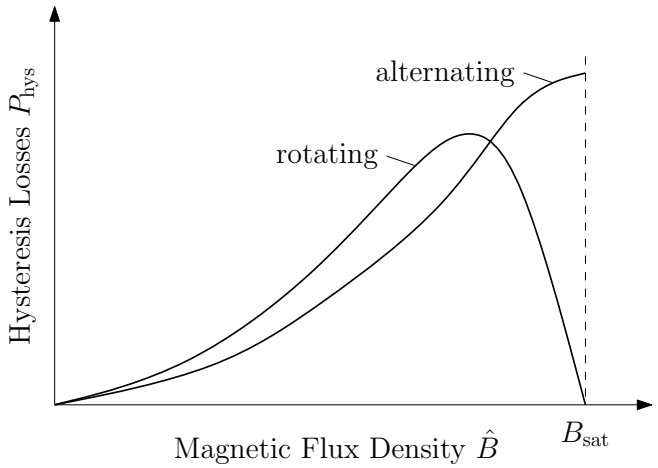

Fig. 3.1: Qualitative progression of the hysteresis losses under unidirectionally alternating and purely rotational field excitation [161].

In tooth roots and tips of rotating electrical machines as well as in T-joints of transformer cores, the magnetic field is locally rotating. In [161], it has been proven theoretically that the hysteresis losses under circular field with low amplitudes are about 2.3 times higher than in the alternating case. Experiments have shown that the losses drop to zero at saturation, as presented in Fig. 3.1. The loss drop is substantiated by the definitive alignment of the magnetic domains at saturation and the hysteresis-free rotation of the field against the domain anisotropy [161].

3.1.2 Eddy current losses

Eddy currents are induced whenever an electrically conductive body is exposed to time varying magnetic fields. The related energy losses are of dynamic nature, since they increase with the frequency of the supply field. Besides the classical eddy current losses present in homogenous materials, excess losses arise owing to the domain structure of the material.

3.1.2.1 Classical eddy current losses

During a magnetization cycle, the ferromagnetic material is exposed to a flux density varying in time. According to Faraday's law this changing flux density induces an electric field within the medium. In a homogenous conductive body, this electric field drives eddy currents as shown in Fig. 3.2(a).

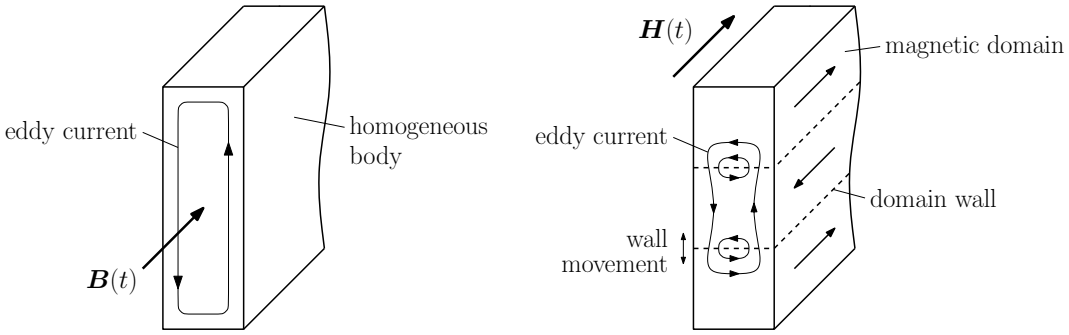

(a) classical (b) excess

Fig. 3.2: Schematic representation of eddy currents emerging from classical and excess effects [162].

The eddy currents themself generate a magnetic field which dampens the original one in the middle of the sheet. This skin effect increases with the frequency and results in an inhomogenous field distribution. Hence, the simplified methods reviewed in section 2.1, which assume a homogenous field within the lamination, are no longer valid for higher frequencies. In Bertotti's statistical loss theory [6], the skin effect is attributed to the excess losses, but such an approach still does not consider the local field distribution inside the sheet. The limits for the applicability of the simplified techniques depend on the geometrical and electromagnetic properties of the steel sheets and lie in a range of several hundred hertz [19].

3.1.2.2 Excess losses

The classical eddy currents account solely for the macroscopic currents induced in a homogeneous body. However, the domain structure of the material leads to the generation of eddy currents at a microscopic level. As indicated in Fig. 3.2(b), the domain walls begin to move when an alternating field is getting applied, provoking eddy currents to flow between the domains. The ensuing microscopic losses are often called excess or anomalous losses. Their extent depends mainly on the grain size of the material under investigation [14]. In materials with large domains, such as grain-oriented steel, the long domain walls move rather fast, leading to high losses. In comparison, non-oriented steel with fine grains is characterized by relatively low excess losses. Owing to their small amount in non-oriented materials, limited attention is paid to excess loss phenomena within this work.

3.2 Finite element method in electromagnetism

Nowadays, finite element methods have become recognized as a general analysis tool used in various engineering disciplines. In the design process of electromagnetic devices, finite element methods readily enable handling complex geometries and realistic materials. Regarding rotating electrical machines, the 2-D non-linear finite element analysis coupled with circuit equations is the state-of-the-art, made available in several commercial software packages. Pending challenges, being topics of ongoing research, are, for example, the inclusion of magnetic hysteresis into the field solution, the modeling of rotor motion in a 3-D environment, or coupling procedures in a multiphysical context.

Hereinafter, the finite element method will be discussed in the context of eddy current problems. Starting from Maxwell's equations, the resulting boundary value problem will be expressed in weighted residual form. Different potential formulations are derived and appropriate methods for space and time discretization will be presented. Some typical issues in modeling of rotating electrical machines are highlighted, too.

3.2.1 Problem definition

Maxwell's equations allow a complete description of electromagnetically coupled phenomena by gathering Ampère's law, Faraday's law of induction and Gauss' law. In this thesis, the focus will be kept on quasistatic eddy current problems, in which the displacement current density is assumed to be negligible. When treating eddy current problems, it is convenient to classify the problem domains according to their electrical conductivities, as presented in Fig. 3.3. In the non-conductive region Ω_n, the magnetic field quantities are static but time-dependent, whereas in the conductive domain eddy currents are additionally present.

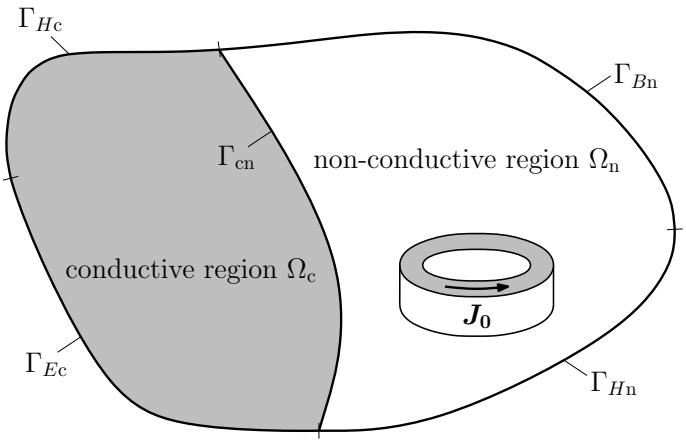

Fig. 3.3: General domain for eddy current problems with boundary conditions. Note that a coil excitation with given current density $\boldsymbol{J_0}$ has been chosen for illustration purposes. Other excitation types are discussed in the text.

To start with, the problem is excited by a given current density $\boldsymbol{J_0}$ situated in Ω_n. Excitations with prescribed total current or voltage of a conductor lead to a skin effect problem with current or voltage excitation, respectively. Skin effect problems will be treated in section 3.2.5.1, and typical excitations for machine models are detailed in section 3.2.6.1.

In the non-conductive region Ω_n, the set of differential equations to be solved is

$$\left.\begin{aligned} \nabla \times \boldsymbol{H} &= \boldsymbol{J_0} \\ \nabla \cdot \boldsymbol{B} &= 0 \end{aligned}\right\} \text{ in } \Omega_n. \tag{3.1}$$

Using time domain notation, the governing equations in the conductive eddy current domain Ω_c become

$$\left.\begin{aligned} \nabla \times \boldsymbol{H} &= \boldsymbol{J} \\ \nabla \times \boldsymbol{E} &= -\frac{\partial \boldsymbol{B}}{\partial t} \\ \nabla \cdot \boldsymbol{B} &= 0 \end{aligned}\right\} \text{ in } \Omega_c, \tag{3.2}$$

where $\boldsymbol{E}$ is the electric field intensity and $\boldsymbol{J}$ is the current density. The field quantities are coupled through constitutive material relations

$$\boldsymbol{B} = \mu \boldsymbol{H}, \quad \boldsymbol{H} = \nu \boldsymbol{B} \quad \text{in } \Omega_n \cup \Omega_c, \tag{3.3}$$

$$\boldsymbol{J} = \sigma \boldsymbol{E}, \quad \boldsymbol{E} = \rho \boldsymbol{J} \quad \text{in } \Omega_c, \tag{3.4}$$

in which μ is the permeability, ν the reluctivity and ρ the resistivity of the material. In the numerical field computations in this work, the magnetic properties are modeled as isotropic and hysteresis-free. Hysteretic behavior will be considered by postprocessing the non-hysteretic (single-valued) field solution to the Preisach model, whose basics are summarized in section 3.3.

On the outer boundaries of the problem domain, either the tangential or the normal component of relevant field quantities is prescribed (see Table 3.1, $\boldsymbol{n}$ stands for the outer normal vector). Along $\Gamma_{H\mathrm{c}}$ and $\Gamma_{H\mathrm{n}}$, the tangential component of the magnetic field intensity is specified. The tangential component of the electrical field intensity is prescribed on $\Gamma_{E\mathrm{c}}$, while the normal component of the magnetic flux density is given along $\Gamma_{B\mathrm{n}}$. On the interface between the conducting and non-conducting region, denoted by Γ_{cn}, the tangential component of the magnetic field intensity and the normal component of the flux density are continuous, providing coupling between the formulations in Ω_{c} and Ω_{n}. Applying these boundary conditions to the differential equations system of (3.1) and (3.2) leads to a unique solution [163].

Table 3.1: Boundary conditions for the problem domain of Fig. 3.3

boundary	condition
$\Gamma_{H\mathrm{c}}$	$\boldsymbol{H} \times \boldsymbol{n} = \boldsymbol{0}$
$\Gamma_{E\mathrm{c}}$	$\boldsymbol{E} \times \boldsymbol{n} = \boldsymbol{0}$
$\Gamma_{H\mathrm{n}}$	$\boldsymbol{H} \times \boldsymbol{n} = \boldsymbol{K}$
$\Gamma_{B\mathrm{n}}$	$\boldsymbol{B} \cdot \boldsymbol{n} = -b$
Γ_{cn}	$\boldsymbol{H} \times \boldsymbol{n}$ and $\boldsymbol{B} \cdot \boldsymbol{n}$ continuous

The symbol $\boldsymbol{K}$ denotes any existing surface current densities and b stands for surface charge densities.

In the following, the numerical solution of the presented quasistatic eddy current problem will be discussed, by first introducing some basic concepts of finite element modeling. Afterwards, the finite element equations will be formulated by means of suitable potential functions.

3.2.2 Method of weighted residuals

The method of weighted residuals provides a sound basis for the formulation of finite element methods. Thereby, an approximate solution of a boundary value problem is sought by expressing the problem in weak form using an integral approach.

First, a time-independent electromagnetic field problem will be considered, defined by a differential equation of the form

$$Au - f = 0 \tag{3.5}$$

where A is a differential operator, f the known excitation function, and u the unknown function. The boundary value problem becomes completely specified through Dirichlet and Neumann boundary conditions. Dirichlet boundary conditions define the function values along a boundary, whereas Neumann conditions prescribe the normal derivatives

of the solution. Neumann boundary conditions are satisfied implicitly within the weak formulation and are therefore often called natural boundary conditions.

For the numerical solution, the unknown function is approximated as a linear combination of basis functions n_j using the following ansatz:

$$u \approx \tilde{u} = u_D + \sum_{j=1}^{N} u_j n_j. \tag{3.6}$$

The function u_D satisfies the inhomogeneous Dirichlet boundary conditions. The N linearly independent basis functions fulfill the homogeneous Dirichlet conditions, and u_j are constant coefficients. Evaluating (3.5) with the approximated function $\widetilde{u}$ leads inherently to an error, called residual r

$$A\tilde{u} - f = r \neq 0. \tag{3.7}$$

The principle of weighted residuals states that the product of the residual and an arbitrary weighting function w_i vanishes when integrated over the whole problem domain Ω

$$\int_\Omega w_i r \,\mathrm{d}\Omega = \int_\Omega w_i (A\tilde{u} - f) \,\mathrm{d}\Omega = 0, \qquad i = 1, 2, \ldots, N. \tag{3.8}$$

If the weighting functions are selected to be the same as those for the approximation of the solution, Galerkin's method is arrived at. Substituting (3.6) to (3.8) with $w_i = n_i$ results in the following equations system

$$\sum_{j=1}^{N} u_j \int_\Omega n_i A n_j \,\mathrm{d}\Omega = \int_\Omega n_i f \,\mathrm{d}\Omega - \int_\Omega n_i A u_D \,\mathrm{d}\Omega \tag{3.9}$$

which can be rewritten in matrix form as

$$[A]\{u\} = \{b\}. \tag{3.10}$$

The coefficients of the stiffness matrix $[A]$ are obtained as

$$A_{ij} = \int_\Omega n_i A n_j \,\mathrm{d}\Omega. \tag{3.11}$$

If the differential operator A is symmetric, the matrix $[A]$ is symmetric as well. The vector $\{u\}$ comprises the unknown variables u_j, and the elements of the right hand side vector $\{b\}$ are given as

$$b_i = \int_\Omega n_i f \,\mathrm{d}\Omega - \int_\Omega n_i A u_D \,\mathrm{d}\Omega. \tag{3.12}$$

In transient eddy current problems, the time derivatives of the field quantities need also to be considered, leading to an operator equation of the form

$$Au + B\frac{\partial u}{\partial t} - f = 0. \tag{3.13}$$

The unknown function is now space- and time-dependent and will be approximated as

$$u \approx \tilde{u}(\boldsymbol{r}, t) = u_D(\boldsymbol{r}, t) + \sum_{j=1}^{N} u_j(t) n_j(\boldsymbol{r}). \tag{3.14}$$

In contrast to static problems, the coefficients u_j are time-dependent. The dependence of $\tilde{u}$ on the spatial coordinate $\boldsymbol{r}$ is taken into account by the basis functions n_j.

Applying Galerkin's method to the differential equation of (3.13) leads to

$$\sum_{j=1}^{N} \left(u_j \int_\Omega n_i A n_j \,\mathrm{d}\Omega + \dot{u}_j \int_\Omega n_i B \mathrm{n}_j \,\mathrm{d}\Omega \right) = \int_\Omega n_i f \,\mathrm{d}\Omega - \int_\Omega n_i A u_D \,\mathrm{d}\Omega - \int_\Omega n_i B \dot{u}_D \,\mathrm{d}\Omega, \tag{3.15}$$

wherein the dotted quantities denote the first-order time derivatives. Again, the Galerkin equations can be presented in matrix form as

$$[A]\{u\} + [B]\{\dot{u}\} = \{b\}, \tag{3.16}$$

with

$$A_{ij} = \int_\Omega n_i A n_j \,\mathrm{d}\Omega, \qquad B_{ij} = \int_\Omega n_i B \mathrm{n}_j \,\mathrm{d}\Omega, \tag{3.17}$$

and

$$b_i = \int_\Omega n_i f \,\mathrm{d}\Omega - \int_\Omega n_i A u_D \,\mathrm{d}\Omega - \int_\Omega n_i B \dot{u}_D \,\mathrm{d}\Omega. \tag{3.18}$$

The numerical solution of problems formulated by Galerkin's method requires discretization in terms of space and time. The next two sections discuss suitable discretization methods for electromagnetic field problems.

3.2.3 Space discretization using finite elements

In the classical Galerkin method, the unknown function is represented by a set of basis functions which are defined over the whole problem domain. However, in practical problems it is rather difficult to approximate the true solution over the entire domain. Therefore, it appears expedient to divide the entire continuous domain in small subdomains, called finite elements, over which simple basis functions are defined.

Depending on the dimensionality of the problem under investigation, the domain can be subdivided into line segments (1-D), triangles or rectangles (2-D), or tetrahedra, triangular prisms and hexahedral elements (3-D). The discretized structure thus obtained is called mesh or grid. Within the elements, the unknown functions can be represented on a nodal or edge basis.

Using node based elements, the unknown scalar and vector functions are approximated in the nodes associated with the element. The solution is usually interpolated by continuous and piecewise polynomial basis functions which satisfy

$$n_j = \begin{cases} 1 & \text{at node } j \\ 0 & \text{at all other nodes.} \end{cases} \tag{3.19}$$

For a given element geometry, the basis functions can be expressed in local coordinates. If the transformation between these local and the global coordinates (x_j, y_j, z_j) is expressed with the same basis functions, one speaks of isoparametric elements. The isoparametric representation transforms an arbitrarily shaped element in the global xyz-space into a regularly shaped element in the local $\xi\eta\zeta$-space:

$$x = \sum_{j=1}^{N_\mathrm{n}} x_j n_j(\xi,\eta,\zeta), \qquad y = \sum_{j=1}^{N_\mathrm{n}} y_j n_j(\xi,\eta,\zeta), \qquad z = \sum_{j=1}^{N_\mathrm{n}} z_j n_j(\xi,\eta,\zeta). \tag{3.20}$$

The shape functions n_j are dependent on the number of nodes N_n present in the element. The use of isoparametric elements with higher-order shape functions allows to form more general shapes and minimizes discretization errors on curved boundaries.

When expressing vector quantities with nodal elements, they impose full continuity of the vector field in normal and tangential direction. Under certain conditions, this can lead to erroneous and non-physical solutions [164, 165]. The problems arising are avoided, if the unknown vector functions are approximated by edge based elements. They assign the degrees of freedom to the edges of the elements and, thus, ensure the physically required continuity of the tangential component, while allowing normal discontinuity. The basis functions of an edge element are of vectorial nature and fulfill

$$\int_{\mathrm{edge}_i} \boldsymbol{n}_j \cdot \mathrm{d}\boldsymbol{r} = \begin{cases} 1 & \text{if } i = j \\ 0 & \text{otherwise.} \end{cases} \tag{3.21}$$

The finite element formulation via basis functions described by (3.19) and (3.21) leads to sparse system matrices with small bandwidth, provided that the nodes are numbered properly. The resulting linear equations systems can be solved by direct or iterative methods. Direct methods are based on Gaussian elimination and are best suited for small problems requiring a low amount of arithmetics. Larger problems involving a high number of degrees of freedom are preferably treated by iterative Krylov subspace methods, such as conjugate gradient techniques. The convergence of the iterative algorithms can be accelerated by using appropriate regularization and preconditioning methods. If non-linear material characteristics come into consideration, the governing equations system becomes non-linear, too. Non-linear matrix solvers are commonly based on the Newton-Raphson method, the Picard-Banach method or the fixed-point iteration.

3.2.4 Time discretization

According to their nature of time dependence, electromagnetic field problems can be classified in static, time-harmonic and transient problems. While static problems are time-independent, harmonic and transient problems require consideration of the time variation of the field quantities. In time-harmonic problems given in the frequency domain, the time dependence is specified by sinusoidal functions having a single frequency. Transient methods formulated in time domain enable modeling of fields varying arbitrarily in time.

Transient formulations call for schemes to discretize the finite element equations in the time domain. In most cases, so-called one-step integration approaches are applied, which can be summarised as θ-methods. The time axis is thereby divided into discrete time intervals Δt_k where the subscript k denotes the k-th step and $t_k = t_{k-1} + \Delta t_k$. Expressing the time t between two consecutive time steps as

$$t = (1-\theta)t_{k-1} + \theta t_k, \tag{3.22}$$

with $\theta \in [0,1]$, and considering the matrix-type problem of (3.16), the time derivative of the solution vector $\{\dot{u}\}$ can be approximated as

$$\{\dot{u}(t)\} \approx \frac{\{u_k\} - \{u_{k-1}\}}{\Delta t_k}, \tag{3.23}$$

wherein the notation $\{u(t_k)\} = \{u_k\}$ is used. Approximating further

$$\{u(t)\} \approx (1-\theta)\{u_{k-1}\} + \theta\{u_k\}, \qquad \{b(t)\} \approx (1-\theta)\{b_{k-1}\} + \theta\{b_k\}, \tag{3.24}$$

and substituting these relations to (3.16) yields

$$[A]((1-\theta)\{u_{k-1}\} + \theta\{u_k\}) + [B]\left(\frac{\{u_k\} - \{u_{k-1}\}}{\Delta t_k}\right) = (1-\theta)\{b_{k-1}\} + \theta\{b_k\}. \tag{3.25}$$

After bringing the known quantities of the previous $(k-1)$-th time step to the right hand side, this algebraic equations system is solved in each time step k using established methods.

If $\theta = 0$, the forward Euler method is obtained, $\theta = 1$ gives the backward Euler scheme. Other popular choices are $\theta = 1/2$ (Crank-Nicolson's method) or $\theta = 2/3$ (Galerkin's method). Choosing $1/2 < \theta \leq 1$ results in an unconditionally stable scheme which is stable regardless of the selected time step size.

3.2.5 Formulations for eddy current problems

Electromagnetic field problems are efficiently dealt with by means of potential functions describing magnetic or electric field quantities. Using scalar and vector potentials as primary variables significantly reduces the number of degrees of freedom to be solved, allowing for an economic treatment of various problem types.

Regarding quasistatic eddy current problems, the magnetic field must be described in both conductive and non-conductive regions, whereas the electric field needs to be considered in the conductive domains only. These fields can be represented by potentials in different ways. For instance, the solenoidality of the magnetic flux density enables to introduce the magnetic vector potential $\boldsymbol{A}$ as

$$\boldsymbol{B} = \nabla \times \boldsymbol{A} \quad \text{in } \Omega_\mathrm{n} \cup \Omega_\mathrm{c}. \tag{3.26}$$

In conductive regions, an electric scalar potential V can be defined, which satisfies

$$\boldsymbol{E} = -\frac{\partial \boldsymbol{A}}{\partial t} - \nabla \frac{\partial V}{\partial t} \quad \text{in } \Omega_\mathrm{c}. \tag{3.27}$$

The time derivative in the second term ensures the symmetry of the resulting Galerkin equations [166]. Alternatively, the electric field quantities can be expressed with the aid of the electric vector potential $\boldsymbol{T}$, since the current density becomes divergence-free under quasistatic conditions:

$$\boldsymbol{J} = \nabla \times \boldsymbol{T} \quad \text{in } \Omega_\mathrm{c}. \tag{3.28}$$

Introducing the reduced magnetic scalar potential Φ, the magnetic field intensity can be written as

$$\boldsymbol{H} = \boldsymbol{T_0} + \boldsymbol{T} - \nabla\Phi \quad \text{in } \Omega_\mathrm{c}, \tag{3.29}$$

$$\boldsymbol{H} = \boldsymbol{T_0} - \nabla\Phi \quad \text{in } \Omega_\mathrm{n}. \tag{3.30}$$

The use of an impressed vector potential $\boldsymbol{T_0}$ avoids modeling of complex coil geometries in the finite element mesh. It describes the current sources as

$$\boldsymbol{J_0} = \nabla \times \boldsymbol{T_0} \quad \text{in } \Omega_\mathrm{n}. \tag{3.31}$$

One possible choice is $\boldsymbol{T_0} = \boldsymbol{H_0}$, where $\boldsymbol{H_0}$ is the field of the coils in free space which can be obtained from Biot Savart's law

$$\boldsymbol{H_0}(\boldsymbol{r}) = \frac{1}{4\pi} \int\limits_{\Omega} \frac{\boldsymbol{J_0} \times (\boldsymbol{r} - \boldsymbol{r'})}{|\boldsymbol{r} - \boldsymbol{r'}|^3} \, \mathrm{d}\Omega'. \tag{3.32}$$

The introduced potentials provide the basis for different eddy current formulations [164], of which the most relevant ones will be presented in the following. Besides the $\boldsymbol{A}$,V-$\boldsymbol{A}$ and $\boldsymbol{T}$,Φ-Φ formulations commonly available in various commercial software packages, also the $\boldsymbol{A}$,$\boldsymbol{T}$-$\boldsymbol{A}$ formulation will be discussed, since it has proven to be advantageous in some specific cases investigated.

3.2.5.1 $\boldsymbol{A}$,V-$\boldsymbol{A}$ formulation

Formulating Ampère's law and the continuity equation for the current density by means of the potentials $\boldsymbol{A}$ and V leads to

$$\left.\begin{aligned} \nabla \times (\nu \, \nabla \times \boldsymbol{A}) + \sigma \frac{\partial \boldsymbol{A}}{\partial t} + \sigma \nabla \frac{\partial V}{\partial t} &= \boldsymbol{0}, \\ -\nabla \cdot \left(\sigma \frac{\partial \boldsymbol{A}}{\partial t} + \sigma \nabla \frac{\partial V}{\partial t} \right) &= 0 \end{aligned}\right\} \text{ in } \Omega_\mathrm{c}. \tag{3.33}$$

In the non-conductive domain one obtains

$$\nabla \times (\nu \, \nabla \times \boldsymbol{A}) = \boldsymbol{J_0} \quad \text{in } \Omega_\mathrm{n}. \tag{3.34}$$

Representing the boundary conditions of Table 3.1 in terms of potentials results in Dirichlet and Neumann conditions summarized in Table 3.2. On the boundary $\Gamma_{E\mathrm{c}}$, a constant scalar potential V_0 is specified, enabling treatment of skin effect problems with voltage excitation. Current excitation can be taken into account by introducing V_0 as an unknown constant satisfying the following integral relation [167]:

$$\int\limits_{\Gamma_{E\mathrm{c}}} \sigma \left(\frac{\partial \boldsymbol{A}}{\partial t} + \nabla \frac{\partial V}{\partial t} \right) \cdot \boldsymbol{n} \, \mathrm{d}\Gamma = I, \tag{3.35}$$

where I is the given current.

Table 3.2: Boundary conditions for the $\boldsymbol{A}$,V-$\boldsymbol{A}$ formulation

boundary	condition
$\Gamma_{H\mathrm{c}}$	$(\nu\,\nabla\times\boldsymbol{A})\times\boldsymbol{n}=\boldsymbol{0}$ and $\left(-\sigma\frac{\partial\boldsymbol{A}}{\partial t}-\sigma\nabla\frac{\partial V}{\partial t}\right)\cdot\boldsymbol{n}=0$
$\Gamma_{E\mathrm{c}}$	$\boldsymbol{A}\times\boldsymbol{n}=\boldsymbol{0}$ and $V=\text{constant}=V_0$
$\Gamma_{H\mathrm{n}}$	$(\nu\,\nabla\times\boldsymbol{A})\times\boldsymbol{n}=\boldsymbol{K}$
$\Gamma_{B\mathrm{n}}$	$(\nabla\times\boldsymbol{A})\cdot\boldsymbol{n}=-b$
Γ_{cn}	$(\nu_{\mathrm{c}}\,\nabla\times\boldsymbol{A}_{\mathrm{c}})\times\boldsymbol{n}_{\mathrm{c}}+(\nu_{\mathrm{n}}\,\nabla\times\boldsymbol{A}_{\mathrm{n}})\times\boldsymbol{n}_{\mathrm{n}}=\boldsymbol{0}$ and $(\nabla\times\boldsymbol{A}_{\mathrm{c}})\cdot\boldsymbol{n}_{\mathrm{c}}+(\nabla\times\boldsymbol{A}_{\mathrm{n}})\cdot\boldsymbol{n}_{\mathrm{n}}=0$

The subscript c denotes quantities defined in the conductive domain, n those ones existing in the non-conductive region. For the outer normal vectors holds $\boldsymbol{n}_{\mathrm{c}}=-\boldsymbol{n}_{\mathrm{n}}$.

When applying Galerkin's method, the magnetic vector potential is advantageously expanded by edge basis functions and the electric scalar potential by nodal functions [168]. The resulting equations system is symmetric but singular, since the gradient of any nodal based function lies in the function space of the edge based ones [164]. The singularity of the system matrix poses no hindrance when conjugate gradient techniques are applied, provided that the right hand side is consistent. Direct methods require gauging of the vector potential, for instance being realized by tree-gauge approaches [169]. The $\boldsymbol{A}$,V-$\boldsymbol{A}$ formulation necessitates accurate discretization of the exciting coils within the finite element mesh. This disadvantage can be bypassed by a reduced magnetic vector potential formulation, in which the excitation field is treated separately.

3.2.5.2 $\boldsymbol{T}$,Φ-Φ formulation

Substituting the potentials defined in (3.28)-(3.31) into Maxwell's equations, the governing differential equations become

$$\left.\begin{aligned}\nabla\times(\rho\,\nabla\times\boldsymbol{T})+\mu\frac{\partial\boldsymbol{T}}{\partial t}-\mu\nabla\frac{\partial\Phi}{\partial t}&=-\mu\frac{\partial\boldsymbol{T_0}}{\partial t},\\ \nabla\cdot(\mu\boldsymbol{T}-\mu\nabla\Phi)&=-\nabla\cdot(\mu\boldsymbol{T_0})\end{aligned}\right\}\ \text{in }\Omega_{\mathrm{c}},\tag{3.36}$$

and

$$-\nabla\cdot(\mu\nabla\Phi)=-\nabla\cdot(\mu\boldsymbol{T_0})\ \text{ in }\Omega_{\mathrm{n}}.\tag{3.37}$$

Expanding $\boldsymbol{T}$ in terms of edge basis functions, and Φ by nodal basis functions leads again to a symmetric and singular Galerkin equations system.

Table 3.3: Boundary conditions for the $\boldsymbol{T}$,Φ-Φ formulation

boundary	condition
$\Gamma_{H\mathrm{c}}$	$\boldsymbol{T} \times \boldsymbol{n} = \boldsymbol{T_0} \times \boldsymbol{n} = \boldsymbol{0}$ and $\Phi = \text{constant} = \Phi_0$
$\Gamma_{E\mathrm{c}}$	$(\rho \nabla \times \boldsymbol{T}) \times \boldsymbol{n} = -(\rho \nabla \times \boldsymbol{T_0}) \times \boldsymbol{n} = \boldsymbol{0}$ and $\mu(\boldsymbol{T} - \nabla\Phi) \cdot \boldsymbol{n} = -\mu \boldsymbol{T_0} \cdot \boldsymbol{n} = 0$
$\Gamma_{H\mathrm{n}}$	$\Phi = \text{constant} = \Phi_0$
$\Gamma_{B\mathrm{n}}$	$\mu \frac{\partial \Phi}{\partial \boldsymbol{n}} = b + \mu \boldsymbol{T_0} \cdot \boldsymbol{n}$
Γ_{cn}	$\boldsymbol{T} \times \boldsymbol{n} = \boldsymbol{0}$ and $(\mu_\mathrm{c} \boldsymbol{T_0} + \mu_\mathrm{c} \boldsymbol{T} - \mu_\mathrm{c} \nabla\Phi) \cdot \boldsymbol{n}_\mathrm{c} + (\mu_\mathrm{n} \boldsymbol{T_0} - \mu_\mathrm{n} \nabla\Phi) \cdot \boldsymbol{n}_\mathrm{n} = 0$

On the boundaries, the potentials have to fulfill the conditions listed in Table 3.3. If the conducting domain includes holes, the non-conducting region becomes multiply connected leading to a multivalued scalar potential. This restriction can be circumvented by defining fake conductors in the holes or by introducing cutting domains featuring a potential jump [170]. Most efficiently, tree-co-tree techniques can be applied to make multiply connected topologies simply connected [171].

3.2.5.3 *A*,*T*-*A* formulation

In this formulation, the current vector potential $\boldsymbol{T}$ is used exclusively to describe the current density in the conductive domain. The magnetic field in the whole domain is represented by the magnetic vector potential $\boldsymbol{A}$. Reformulating Ampère's law and Faraday's law yields

$$\left.\begin{aligned} \nabla \times (\nu \nabla \times \boldsymbol{A}) - \nabla \times \boldsymbol{T} &= \boldsymbol{0}, \\ \nabla \times (\rho \nabla \times \boldsymbol{T}) + \nabla \times \frac{\partial \boldsymbol{A}}{\partial t} &= \boldsymbol{0} \end{aligned}\right\} \text{ in } \Omega_\mathrm{c}, \tag{3.38}$$

whereas (3.34) holds in the non-conductive domain. Expressing $\boldsymbol{T}$ as the time derivative of a modified current vector potential, $\boldsymbol{t}$, and approximating $\boldsymbol{A}$ and $\boldsymbol{t}$ by edge basis functions, results again in symmetric Galerkin equations.

At a first glance, the use of two vector potentials appears to be inefficient when compared to vector-scalar potential formulations. However, this formulation explicitly satisfies the solenoidality of $\boldsymbol{B}$ and $\boldsymbol{J}$ on the boundaries by specifying the tangential components of $\boldsymbol{A}$ and $\boldsymbol{T}$ as Dirichlet conditions (see Table 3.4). Compared to vector-scalar potential formulations with implicit Neumann conditions, the $\boldsymbol{A}$,$\boldsymbol{T}$-$\boldsymbol{A}$ formulation entails, in some cases, faster convergence of iterative solvers.

Table 3.4: Boundary conditions for the $\boldsymbol{A}$,$\boldsymbol{T}$-$\boldsymbol{A}$ formulation

boundary	condition
$\Gamma_{H\mathrm{c}}$	$(\nu \nabla \times \boldsymbol{A}) \times \boldsymbol{n} = \boldsymbol{0}$ and $\boldsymbol{T} \times \boldsymbol{n} = \boldsymbol{0}$
$\Gamma_{E\mathrm{c}}$	$(\rho \nabla \times \boldsymbol{T}) \times \boldsymbol{n} = \boldsymbol{0}$ and $\boldsymbol{A} \times \boldsymbol{n} = \boldsymbol{0}$
$\Gamma_{H\mathrm{n}}$	$(\nu \nabla \times \boldsymbol{A}) \times \boldsymbol{n} = \boldsymbol{K}$
$\Gamma_{B\mathrm{n}}$	$(\nabla \times \boldsymbol{A}) \cdot \boldsymbol{n} = -b$
Γ_{cn}	$(\nu_{\mathrm{c}} \nabla \times \boldsymbol{A}_{\mathrm{c}}) \times \boldsymbol{n}_{\mathrm{c}} + (\nu_{\mathrm{n}} \nabla \times \boldsymbol{A}_{\mathrm{n}}) \times \boldsymbol{n}_{\mathrm{n}} = \boldsymbol{0}$ and $(\nabla \times \boldsymbol{A}_{\mathrm{c}}) \cdot \boldsymbol{n}_{\mathrm{c}} + (\nabla \times \boldsymbol{A}_{\mathrm{n}}) \cdot \boldsymbol{n}_{\mathrm{n}} = 0$
Γ_{cn1}	$\boldsymbol{T} \times \boldsymbol{n} = \boldsymbol{0}$
Γ_{cn2}	$(\nabla \times (\rho \nabla \times \boldsymbol{T})) \times \boldsymbol{n}_{\mathrm{c}} = \left(\nabla \times \frac{\partial \boldsymbol{A}}{\partial t}\right) \times \boldsymbol{n}_{\mathrm{n}}$

On the interface between the conductive and non-conductive domain Γ_{cn}, boundary conditions for $\boldsymbol{T}$ need to be specified in addition to those for $\boldsymbol{A}$. From a numerical point of view it would be desirable to set $\boldsymbol{T} \times \boldsymbol{n} = \boldsymbol{0}$ as a homogeneous Dirichlet condition. But such an approach would again complicate the treatment of multiply connected regions. Therefore it is most effective to subdivide $\Gamma_{\mathrm{cn}} = \Gamma_{\mathrm{cn1}} \cup \Gamma_{\mathrm{cn2}}$, and to derive the interface condition on Γ_{cn2} from Fraday's law.

3.2.6 2-D field analysis of rotating electrical machines

The electromagnetic field inside the machine cores can often be assumed to be constant along the axial direction, enabling its representation by cross-sectional 2-D models. Based on the 2-D field distribution, various machine properties can be readily evaluated, such as speed-torque characteristics or equivalent circuit parameters. Commonly, the 2-D analysis is based on the $\boldsymbol{A}$,V-$\boldsymbol{A}$ formulation employing a single component vector potential. This approach is also implemented in the commercial 2-D software packages used in this thesis [172]. Hereinafter, some special challenges faced in this respect will be discussed. The 3-D simulations are based on an in-house code and will be detailed further in the next chapters.

3.2.6.1 Coupling field and circuit model

The windings of the machine are supplied by an external electrical circuit requiring coupling of the field and circuit equations. In windings with massive conductors, skin effects may occur, whereas thin stranded coils are usually modeled as regions without skin effect. The machine windings can either be voltage or current driven. In current driven problems, the feeding current is known a priori and specified by (3.35) in the case of massive

conductors, or by a uniform current density in the case of stranded coils. In voltage driven windings with skin effect, the supply current I is introduced as an unknown variable and fulfills

$$U = (R + R_{\mathrm{dc}})I + L_\sigma \frac{\mathrm{d}I}{\mathrm{d}t} + R_{\mathrm{dc}} \int\limits_{\Gamma_{Ec}} \sigma \frac{\partial \boldsymbol{A}}{\partial t} \cdot \boldsymbol{n} \, \mathrm{d}\Gamma. \tag{3.39}$$

The circuit parameters R and L_σ denote any existing resistances or leakage inductances not considered by the field model, R_{dc} is the dc-resistance of the winding, and U stands for the given voltage. For windings with no skin effect, the induced voltages are obtained from the time derivative of the averaged flux linkage associated with the coil. The coils need to be connected according to the machine's winding configuration, leading to an additional equations system for the unknown currents which is solved together with the field equations [173].

3.2.6.2 Transient analysis with rotor motion

A major part of the iron losses in rotating electrical machines originates from high-order field harmonics caused, for example, by slotting effects or the discrete winding distribution. An accurate assessment of all high-order frequency components necessitates transient analyses being realized by time-stepping schemes. If the transient analysis is started with zero initial values, several periods have to be stepped through before reaching the steady state. The ensuing large computational burden can be alleviated by utilizing approximate frequency domain techniques to determine non-zero initial values [174, 175]. The initial field values are thereby obtained by a time-harmonic pre-simulation. Non-linearity of the magnetic materials is usually taken into account by effective reluctivity approaches [176], out of which the average energy method of [177] will be applied within this work.

If the field analysis is performed in the time domain, the motion of the rotor needs to be considered, requiring coupling of two domains sliding relative to each other. A common method to treat motional problems is the moving band technique [178], in which a thin air-gap layer is re-meshed in every time step. Other approaches are based on mortar elements [179] or simple interpolation techniques [172, 180]. In the mortar method, an integration mesh with additional basis functions is introduced on the interface by means of which a set of constraint equations is defined. The second technique, which is also used in this thesis, interpolates the variables from the master mesh to the slave mesh with the aid of linear approximation functions.

In [58], [180] and [181], the mentioned methods have also been extended to 3-D machine models, which have become feasible due to the recent advances in computational power. 3-D models allow to take into account axial fields arising from air-gap fringing and the end winding leakage as well as skewing effects. If the axial fields are neglected, skewed induction machines can be analyzed by multi-slice models [112, 113]. They represent the

axial field distribution by a set of 2-D models given at different positions along the machine length. The 2-D slices are coupled trough an external electrical circuit which enforces the same current in all 2-D field models.

3.3 Preisach hysteresis model

The Preisach model features accurate characterization of hysteretic materials by means of established mathematical formalisms. As already outlined in the literature review, the model enables correct modeling of major and minor loops by taking into account essential hysteretic properties. Despite its profound physical and theoretical background, the numerical implementation of the model is still lacking a general approach, hindering its integration into finite element software packages. Such problems involve, for instance, the necessity of extensive experimental data, the inversion of the classical Preisach model, or its extension to rotational and dynamic fields. Below, efficient algorithms for tackling the implementation problems encountered will be presented, after giving some fundamental considerations on classical Preisach modeling. The used algorithms are based on the work of [64] and [74], whereby the latter has been expanded further in [84] and [182].

3.3.1 Model representation by Everett functions

The Preisach model described by (2.8), is advantageously implemented by means of Everett functions. The values of the Everett function can be calculated from the input extrema (first-order reversal curves) of the flux density as

$$E(h_\alpha, h_\beta) = \frac{1}{2}(B(h_\alpha, h_\beta) - B(h_\alpha)) = \iint\limits_{\Omega(h_\alpha, h_\beta)} \mu(h_\alpha, h_\beta)\,\mathrm{d}h_\alpha\,\mathrm{d}h_\beta, \tag{3.40}$$

in which $B(h_\alpha)$ refers to the values of B at the reversal points and $B(h_\alpha, h_\beta)$ to values along the first-order reversal curves. In contrast to analytical approaches based on Gaussian or Lorentzian distribution functions, the use of precalculated Everett functions eliminates the numerically cumbersome double integration in the Preisach plane Ω.

If the model is identified from $k = 1, 2, \ldots, N_{\mathrm{rev}}$ reversal curves, the output flux density is obtained by summing up the Everett functions at the ascending and descending reversal points $h_{\alpha k}$ and $h_{\beta k}$, respectively

$$B(t) = B[H(t)] = -E(h_{\alpha 0}, h_{\beta 0}) + 2\sum_{k=1}^{N_{\mathrm{rev}}} (E(h_{\alpha k}, h_{\beta k-1}) - E(h_{\alpha k}, h_{\beta k})). \tag{3.41}$$

The Everett weight $E(h_{\alpha 0}, h_{\beta 0})$ is evaluated at the turning points of the major loop given by $h_{\alpha 0}$ and $h_{\beta 0}$.

Implementing the Preisach model by Everett functions guarantees high accuracy and efficiency, but requires measurement of a family of first-order reversal curves, which entails some difficulties [183]. From a practical point of view, it is therefore desirable to construct the first-order reversals from the measured major loop, or even to approximate the major loop analytically using a few parameters provided by the manufacturers of electrical steel.

3.3.1.1 Approximation of the major loop

In chapter 4, the major hysteresis loop will be approximated with the aid of the hyperbolic functions given in [184]:

$$g(H) = \begin{cases} \frac{H+H_\mathrm{c}}{h_1+k_1|H+H_\mathrm{c}|} & \text{for } -H_\mathrm{c} < H < \hat{H}_\mathrm{m} \\ \frac{H+H_\mathrm{c}}{h_1+k_2|H+H_\mathrm{c}|} & \text{for } -\hat{H}_\mathrm{m} < H < -H_\mathrm{c}, \end{cases} \tag{3.42}$$

where H_c denotes the coercivity field and ($\hat{H}_\mathrm{m}$,$\hat{B}_\mathrm{m}$) is the point upto which the material exhibits hysteresis. The parameters h_1, k_1 and k_2 can be identified from the major loop measured under quasistatic conditions or from basic parameters given in the data sheet of the material [182]. The descending branch of the major loop can now be built as

$$B_\mathrm{m}(H) = \hat{B}_\mathrm{m} \frac{2g(H) - g(\hat{H}_\mathrm{m}) - g(-\hat{H}_\mathrm{m})}{g(\hat{H}_\mathrm{m}) - g(-\hat{H}_\mathrm{m})}, \tag{3.43}$$

and the ascending branch results from symmetry since $B_\mathrm{m}(H) = -B_\mathrm{m}(-H)$.

3.3.1.2 Construction of first-order reversal curves

The first-order reversal curves can be created from the major loop in various ways. One possibility is to approximate them analytically, as for example shown in [185]. Here, the first-order reversal curves will be constructed by means of a Preisach distribution function obtained pointwise from the major loop. According to [186], a symmetrical distribution function can be represented as

$$\mu(h_\alpha, h_\beta) = \lambda(-h_\alpha)\lambda(h_\beta) \tag{3.44}$$

where λ is 1-D function defined pointwise, which can be used to express the gradient of the descending branch of the major loop as

$$\frac{\mathrm{d}B_\mathrm{m}}{\mathrm{d}H} = 2\lambda(H) \int_{\hat{H}_\mathrm{m}}^{H} \lambda(h_\beta)\,\mathrm{d}h_\beta. \tag{3.45}$$

Dividing $H = \{H_1, H_2, \ldots, H_N\}$ into N equal subintervals Δh, in which $\mathrm{d}B_\mathrm{m}/\mathrm{d}H$ and λ are considered as constant, (3.45) can be discretized as

$$\left.\frac{\mathrm{d}B_\mathrm{m}}{\mathrm{d}H}\right|_i = \frac{B_{\mathrm{m}i+1} - B_{\mathrm{m}i}}{H_{i+1} - H_i} = 2\lambda(H_i) \sum_{l=1}^{i} \lambda(H_l)\Delta h. \tag{3.46}$$

Evaluating this equation for all subintervals $i = 1, 2, \ldots, N$ leads to a bilinear equations system to be solved algebraically [187]. The distribution function thus obtained defines the classical Preisach model completely by the knowledge of the major loop. In this work, the classical model is solely used for calculating first-order reversal curves required in the inversion procedure described below.

3.3.2 Inversion of the classical Preisach model

The classical Preisach model takes the field intensity H as input, and gives the flux density B as output. However, 2-D electromagnetic field problems are conventionally treated by magnetic vector potential formulations requiring B as input quantity for the Preisach model. In order to incorporate the Preisach model into such formulations, the classical model needs to be inverted. Furthermore, the inverted B-based model enables a straightforward dynamization of the static models using the approach of section 3.3.4.

Mostly, the classical Preisach model is inverted by iterative methods [95], or by inverting the distribution function itself [188]. Iterative methods have been found to be computationally demanding, while the inversion of the distribution function is not generally possible. To overcome these restrictions, an inverted Everett function F will be used here which allows to rewrite (3.41) as

$$H(t) = H[B(t)] = -F(b_{\alpha 0}, b_{\beta 0}) + 2\sum_{k=1}^{N_\mathrm{rev}} (F(b_{\alpha k}, b_{\beta k-1}) - F(b_{\alpha k}, b_{\beta k})), \tag{3.47}$$

by exchanging the roles of B and H. The up- and down-switching values b_α and b_β are now controlled by B.

The Everett function is inverted numerically using an algorithm proposed in [182]. The algorithm discretizes the Preisach plane in $M \times M$ points and generates first-order reversal curves depending on B. First, the non-linearity is transformed from B to H, by applying a linear interpolation operator Φ to the descending branch of the major loop described by the discrete values $B_\mathrm{m} = \{B_\mathrm{m1}, B_\mathrm{m2}, \ldots, B_{\mathrm{m}N}\}$:

$$H_{\mathrm{m}j} = \Phi(b_{\alpha j}, H_1, \ldots, H_N; B_\mathrm{m1}, \ldots, B_{\mathrm{m}N}), \qquad j = 1, \ldots, M. \tag{3.48}$$

Then, descending first-order reversal curves are constructed by supplying

$$H_{\mathrm{r}ij} = \frac{i-1}{M-1}(\hat{H}_\mathrm{m} - H_{\mathrm{m}j}) + H_{\mathrm{m}j}, \qquad i = 1, \ldots, N, \quad j = 1, \ldots, M \tag{3.49}$$

to the forward Preisach model identified in section 3.3.1.2, yielding $B_{\mathrm{r}ij}$. Now, the reversal points are controlled by b_α, but the non-linearity of the curves still remains in B. To transform the non-linearity to H, the linear operator Φ is applied once again to each first-order reversal curve

$$H_{\mathrm{rev}ij} = \Phi(b_{\alpha i}, H_{\mathrm{r}1j}, \ldots, H_{\mathrm{r}Nj}; B_{\mathrm{r}1j}, \ldots, B_{\mathrm{r}Nj}), \qquad i = 1, \ldots, j, \quad j = 1, \ldots, M. \tag{3.50}$$

Finally, the inverted Everett function is obtained from $H_{\mathrm{rev}ij}$ in analogy to (3.40). The algorithm used ensures the creation of a uniform and smooth inverted Everett function, provided that $N > M$. For numerical implementations, the $M \times M$ Everett table is mapped to a coarser grid using bicubic spline interpolation.

3.3.3 Vector model

The rotational flux present in electrical machines requires a vectorization of the scalar model presented above. If the vector extension is realized by the Mayergoyz approach, (2.9) can be rewritten in inverted form as

$$\boldsymbol{H}(t) = \sum_{i=1}^{N_\varphi} H_{\varphi_i}(t)\boldsymbol{e}_{\varphi_i} = \sum_{i=1}^{N_\varphi} H[B_{\varphi_i}(t)]\boldsymbol{e}_{\varphi_i}. \tag{3.51}$$

Assuming isotropic material, the input projection of the flux density is given by

$$B_{\varphi_i}(t) = |\boldsymbol{B}(t)| \cos(\varphi - \varphi_i), \tag{3.52}$$

in which φ is the polar angle specifying the direction of the magnetic flux density vector. Anisotropic behavior will be treated in chapter 5 by introducing a generalization of (3.52), which simultaneously improves the rotational loss properties.

The Everett function of the vector model F_φ needs to be re-identified by comparison to the scalar Everett function. The resulting identification problem reads

$$F(b_\alpha, b_\beta) = \sum_{i=1}^{N_\varphi} F_\varphi(b_\alpha \cos\varphi_i, b_\beta \cos\varphi_i) \cos\varphi_i \tag{3.53}$$

and is solved numerically using the procedure developed in [189]. This guarantees that the vector model gives the same output as the scalar one when supplied by a unidirectionally alternating flux density.

3.3.4 Dynamic hybrid model

The vector Preisach model presented is by definition static and excludes any eddy current and excess effects. Coupling suitable eddy current models to a dynamic Preisach model

has proven to be highly accurate [190], but suffers from high computational costs, and, in some cases, from numerical instabilities [93]. In order to avoid such numerical complications, a simplified magnetodynamic vector hysteresis model has been introduced in [90] by adopting concepts of the statistical loss separation theory. Thereby, the magnetic field strength is decomposed into a static hysteresis part H_{hys}, a classical eddy current part H_{cl} and an excess part H_{ex}

$$\begin{aligned} H_{\varphi_i}(t) &= H_{\mathrm{hys}}(t) + H_{\mathrm{cl}}(t) + H_{\mathrm{ex}}(t) \\ &= H[B_{\varphi_i}(t)] + \overline{c}_{\mathrm{cl}}\delta_{\mathrm{e}} \left| \frac{\mathrm{d}B_{\varphi_i}(t)}{\mathrm{d}t} \right|^{\gamma} + \overline{c}_{\mathrm{ex}}\delta_{\mathrm{e}} \left| \frac{\mathrm{d}B_{\varphi_i}(t)}{\mathrm{d}t} \right|^{0.5}, \end{aligned} \tag{3.54}$$

with $\delta_{\mathrm{e}} = \mathrm{sign}(\mathrm{d}B_{\varphi_i}/\mathrm{d}t)$. Introducing the exponent γ as

$$\gamma(B_{\varphi_i}(t)) = a_0 + a_1\delta_{\mathrm{e}} \left(\frac{B_{\varphi_i}(t)}{B_{\mathrm{sat}}} \right) + a_2 \left(\frac{B_{\varphi_i}(t)}{B_{\mathrm{sat}}} \right)^2 \tag{3.55}$$

ensures that the classical eddy current term is non-linearly dependent on the applied magnetic field, which implies accurate modeling of high-order harmonic effects. The constant B_{sat} stands for a predefined saturation value and can be chosen as $B_{\mathrm{sat}} = \hat{B}_{\mathrm{m}}$. The prediction of minor hysteresis loops can be improved by defining a_0 as

$$a_0 = \alpha_0 + \alpha_1 |B_{\mathrm{rev}}|, \tag{3.56}$$

where B_{rev} are the reversal values of the flux density. The parameters $\overline{c}_{\mathrm{ex}}$, a_1, a_2, α_0 and α_1 are identified from dynamic BH-loops measured at different frequencies, $\overline{c}_{\mathrm{cl}}$ can be kept fixed to $\overline{c}_{\mathrm{cl}} = \sigma d^2/12$.

Using definitions of section 2.2.2, the power losses per unit volume are calculated by the Poynting theorem as

$$P = \frac{1}{T} \int_0^T \boldsymbol{H} \cdot \frac{\partial \boldsymbol{B}}{\partial t} \, \mathrm{d}t = \frac{1}{T} \int_0^T \left(H_x \frac{\mathrm{d}B_x}{\mathrm{d}t} + H_y \frac{\mathrm{d}B_y}{\mathrm{d}t} \right) \mathrm{d}t, \tag{3.57}$$

and averaged over a fundamental period. The losses can be separated further into alternating and rotating components following the theorem of [191]:

$$P_{\mathrm{alt}} = \frac{1}{T} \int_0^T |\boldsymbol{H}| \frac{\mathrm{d}|\boldsymbol{B}|}{\mathrm{d}t} \cos(\alpha) \, \mathrm{d}t, \qquad P_{\mathrm{rot}} = \frac{1}{T} \int_0^T \frac{\mathrm{d}\varphi}{\mathrm{d}t} (\boldsymbol{H} \times \boldsymbol{B})_z \, \mathrm{d}t, \tag{3.58}$$

in which α denotes the phase lag between the $\boldsymbol{B}$ and $\boldsymbol{H}$ vectors. The subscript z in $(\boldsymbol{H} \times \boldsymbol{B})_z$ represents the vector component in z-direction.

The model of (3.54) combines features of the statistical engineering approach with the accuracy of advanced approaches for solving the penetration equation, and is therefore referred to as the hybrid model. It can be used for the iron loss calculation either at the postprocessing stage, as in this work, or even for incorporating the iron losses into the field solution. In the next chapter, the hybrid model will by compared to the traditional model of (2.4) as well as to the 3-D eddy current model proposed.

4 3-D eddy current model for steel laminations of rotating electrical machines

Accurate methods for predicting iron losses in electrical machines need to cope with complex phenomena, like high harmonic content and rotating flux. In particular, the exact computation of the eddy current losses plays a key role within this context, since they become a major loss component at high frequencies. As discussed in chapter 2, the eddy current losses in the steel sheets are commonly evaluated using simplified postprocessing methods based on the statistical loss theory. More enhanced methods employ 3-D homogenization techniques or 1-D lamination models. Homogenized models solely account for the planar eddy currents caused by perpendicular fields. 1-D models consider the penetration of the flux density along the lamination thickness, but neglect the return path of the eddy currents on the sheet edges.

In this chapter, a novel method to compute the true 3-D eddy current distribution in the steel laminations will be presented. The 3-D model is excited by time-dependent boundary conditions derived from a 2-D cross-sectional field analysis. The proposed approach allows separate treatment of the stator and rotor sheets preventing computationally expensive transient 3-D simulations for the whole machine. Nevertheless, all loss relevant effects, such as high-order harmonics and the rotor motion are accounted for in the analysis. The resulting losses serve as a validation basis for various reduced models and enable the segregation of the different iron loss components.

The method developed is applied to the loss estimation of a three-phase, low-voltage, four pole slip-ring induction machine designed for wind power applications in the megawatt range. Details on the machine parameters and the used steel sheet type are given in appendix A. Some further, previously unpublished, results of another machine of similar type are given in appendix B.

The investigations in this chapter are restricted to no load operation only. Results for loaded operation will be presented in chapter 6, along with a method to reduce the computational burden of the original 3-D time-stepping approach. The 3-D eddy current model has been originally presented at [P1] and then published in [P2], including comparisons of the 3-D model to two simplified loss models, as well as validations against iron loss measurements.

4.1 Coupling the 2-D machine model to the 3-D sheet model

The proposed method can be subdivided into two steps: first, a transient 2-D field analysis is carried for the whole machine. In a second step, the 3-D eddy current problem is solved separately for a single stator and rotor sheet.

The 2-D field analysis is performed by means of a third-party software package using a nodal based $\boldsymbol{A}$,V-$\boldsymbol{A}$ formulation [172]. The problem domain is discretized by rectangular or triangular elements with shape functions of second order. In the 2-D model, the iron regions are assumed to be non-conductive; their magnetic non-linearity is considered by a single-valued magnetization curve and handled by the Newton-Raphson scheme. The massive rotor bars are modeled as eddy current domains, but not the stranded stator conductors. The resistance and leakage inductance of the end windings are taken into account by lumped circuit parameters coupled externally to the field model. The stator windings are driven by currents obtained from measurements or analytical approaches based on the equivalent circuit theory. The movement of the rotor in the time-stepping analysis is treated by nodal interpolation on an air-gap interface layer. Starting transients are attenuated by determining the initial steady state through a time-harmonic pre-simulation.

Only no load operation will be studied within this chapter. During the iron loss measurements under no load, the machine's rotor windings have been kept open in order to prevent undesired rotor currents and, hence, further losses. Neglecting any currents in the rotor windings, the intrinsically transient problem can be reduced to a magnetostatic one, solved for different rotor positions.

The 3-D model is weakly coupled to the 2-D model by impressing the 2-D magnetic vector potential on its boundaries. The specification of the boundary conditions for the 3-D model will be detailed in the next sections. Homogeneous and solely parallel flux is assumed within the iron stack. Therefore, only a single sheet needs to be considered. In [39] it was reported that additional parallel and axial flux due to air-gap fringing and the end winding leakage decays quickly towards the core middle. These stray fluxes will be even smaller for the investigated machine, since the clamping plates have a remarkable shielding effect.

Figs. 4.1 and 4.2 show the 3-D finite element models for the stator and rotor sheets. Because of symmetry, only one pole of the machine and a half of the lamination thickness is modeled. To model the edge effects correctly even for high frequencies, a relatively fine mesh is used near the edges and the tooth tips. Depending on the frequencies of the arising field harmonics, three to ten equally sized finite element layers are used along a half of the sheet thickness. One should note that the finite element mesh of the individual laminates is independent of the grid in the 2-D model. Therefore, a much coarser mesh can be used in the 2-D machine model than in the 3-D model of the sheets.

The 3-D eddy current problem is solved solely in the conductive laminates. Two different eddy current formulations, the $\boldsymbol{A}$,V and $\boldsymbol{A}$,$\boldsymbol{T}$ formulations, are investigated. The

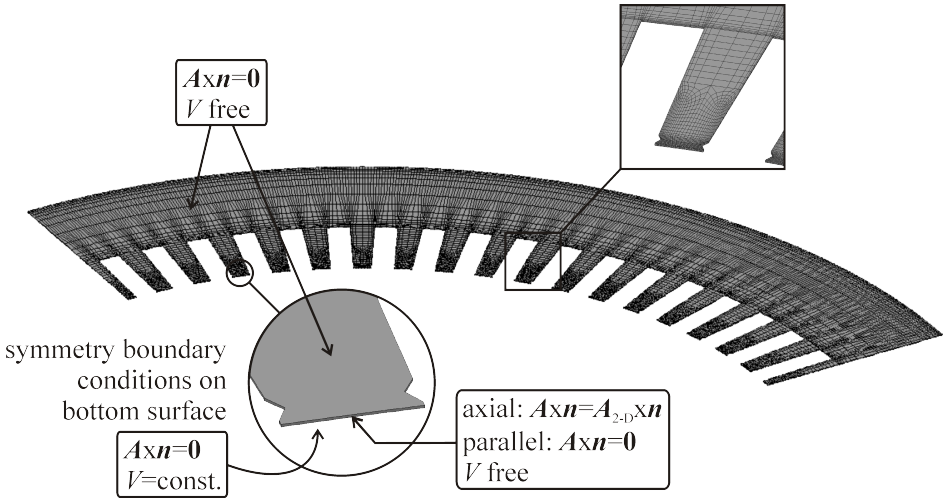

Fig. 4.1: 3-D finite element model of the investigated stator sheet as well as boundary conditions for the $\boldsymbol{A}$,V formulation.

analysis is performed using an in-house software package based on isoparamteric hexahedral edge elements with quadratic shape functions. The employed iterative solver utilizes conjugate gradient methods preconditioned by incomplete Cholesky factorization. Time discretization is managed by the backward Euler scheme, and magnetic non-linearity is handled by the Picard-Banach method.

4.1.1 Boundary conditions for the $\boldsymbol{A}$,V formulation

The electromagnetic field within the lamination is prescribed uniquely by specifying the normal component of $\boldsymbol{B}$ on its boundaries in addition to setting the normal component of $\boldsymbol{J}$ to zero [43]. The prescription of the normal component of $\boldsymbol{B}$ is equivalent to specifying the tangential component of $\boldsymbol{A}$. The $\boldsymbol{A}$,V formulation of (3.33) implicitly satisfies the condition of vanishing normal component of $\boldsymbol{J}$ on the sheet surface by setting the scalar potential V free. However, this natural boundary condition can be only satisfied approximately by the finite element solution.

The tangential component of $\boldsymbol{A}$ on the boundaries along the lamination thickness is extrapolated from the 2-D vector potential and assumed to be constant along the thickness. The boundaries along the lamination thickness are hereinafter called axial boundaries. Since flux in axial direction is neglected, $\boldsymbol{A} \times \boldsymbol{n}$ is set to zero on the boundaries parallel to the sheets. The boundary conditions are then

$$\boldsymbol{A} \times \boldsymbol{n} = \begin{cases} \boldsymbol{A}_{2-\mathrm{D}} \times \boldsymbol{n} & \text{on axial boundaries} \\ \boldsymbol{0} & \text{on parallel boundaries,} \end{cases} \tag{4.1}$$

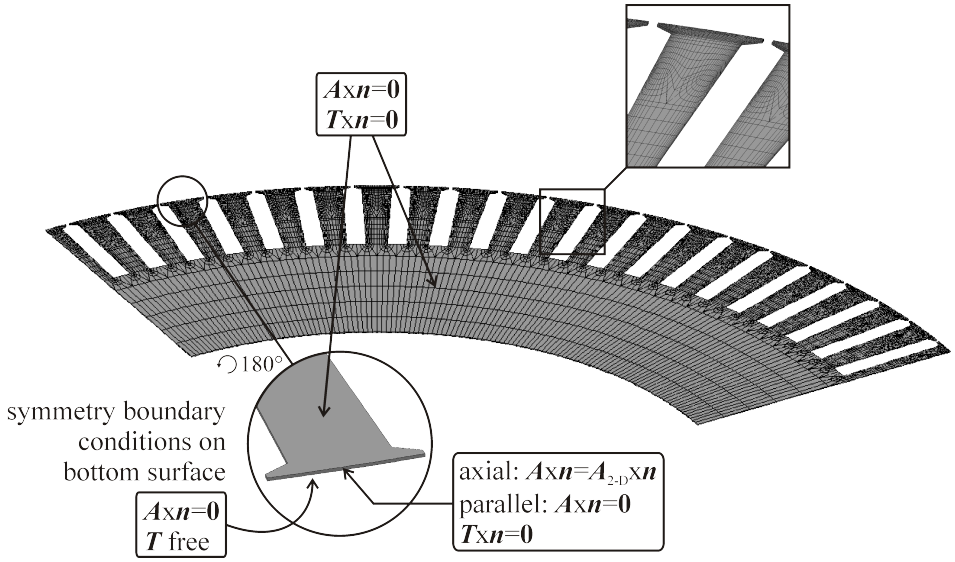

Fig. 4.2: 3-D finite element model of the investigated rotor sheet as well as boundary conditions for the $\boldsymbol{A}$,$\boldsymbol{T}$ formulation.

where $\boldsymbol{A}_{\text{2-D}}$ is the vector potential from the 2-D field solution. The boundary conditions are prescribed anew for every time step. Fig. 4.1 demonstrates the specifications of the boundary conditions for the $\boldsymbol{A}$-V formulation by means of a stator sheet.

4.1.2 Boundary conditions for the $\boldsymbol{A}$,$\boldsymbol{T}$ formulation

Using the $\boldsymbol{A}$-$\boldsymbol{T}$ formulation of (3.38), the normal component of $\boldsymbol{J}$ can be specified by the tangential component of the current vector potential $\boldsymbol{T}$. Unlike the $\boldsymbol{A}$,V formulation, the $\boldsymbol{A}$,$\boldsymbol{T}$ formulation satisfies the condition of vanishing normal component of the current density exactly by setting the $\boldsymbol{T} \times \boldsymbol{n} = \boldsymbol{0}$ on the lamination surface. The boundary conditions for $\boldsymbol{A}$ are the same as those in the $\boldsymbol{A}$,V formulation. Fig. 4.2 shows the boundary conditions for the $\boldsymbol{A}$,$\boldsymbol{T}$ formulation by using the example of a rotor sheet.

4.2 3-D eddy current distribution

After performing a 2-D field analysis for the whole machine, the 3-D models have been solved with the $\boldsymbol{A}$,V and $\boldsymbol{A}$,$\boldsymbol{T}$ formulations using time-dependent boundary conditions from the 2-D solution. In order to cover all relevant harmonic effects, an equidistant time step size of $\Delta t = T/100$ has been used for the stator, and $\Delta t = T/1000$ for the rotor sheet simulation. The absence of high-order field harmonics in the stator allows for using relatively large time step sizes. With increasing load, high-order harmonics become also

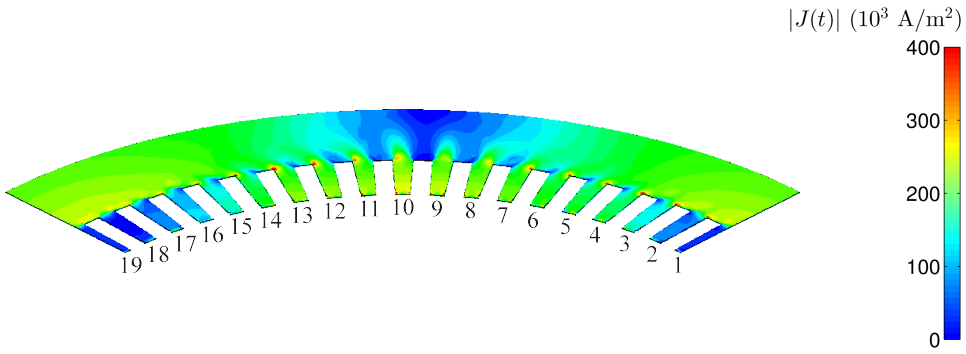

Fig. 4.3: Current density distribution in a stator sheet at a specific time instant and rated no load current.

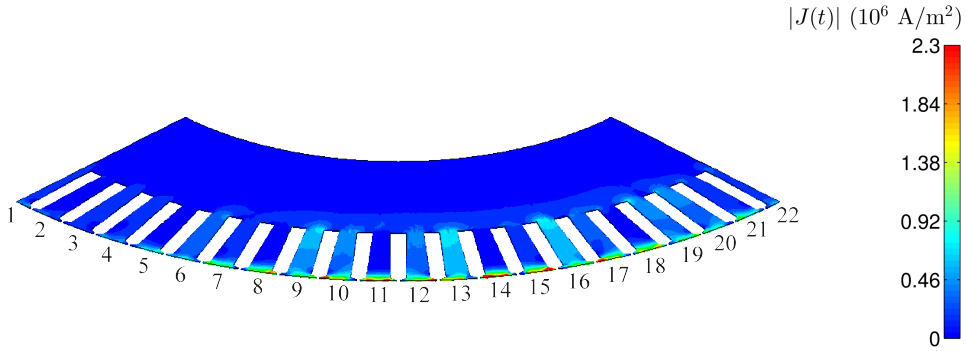

Fig. 4.4: Current density distribution in a rotor sheet at a specific time instant and rated no load current. The sheet is rotated counterclockwise for illustration purposes.

pronounced in the stator sheet, requiring identical time discretization as in the rotor (see also chapter 6).

The current density distribution in the steel sheets is presented in Figs. 4.3 and 4.4, respectively. The simulations shown have been carried out for rated no load current using the $\boldsymbol{A}$,V formulation. In the stator sheet, the current density is quite uniformly distributed and mainly caused by the 50 Hz fundamental frequency component. The eddy currents in the rotor are concentrated in the tooth tips and are almost exclusively evoked by the first stator slot harmonic at 1800 Hz (see also Fig. 6.1). The corresponding losses are obtained by integrating the product of $\boldsymbol{E}$ and $\boldsymbol{J}$ over the sheet volume and averaged over time.

Fig. 4.5 provides an enlarged view of the current density in a stator and rotor tooth. In addition to the computations with the $\boldsymbol{A}$,V formulation, also the results of the $\boldsymbol{A}$,$\boldsymbol{T}$ formulation are presented, indicating excellent agreement between both formulations. The corresponding 3-D behavior of $\boldsymbol{B}$ and $\boldsymbol{J}$ illustrated by vector plots is shown in Fig. 4.6. Only the tooth tip regions are plotted for better visualization. Details on the compu-

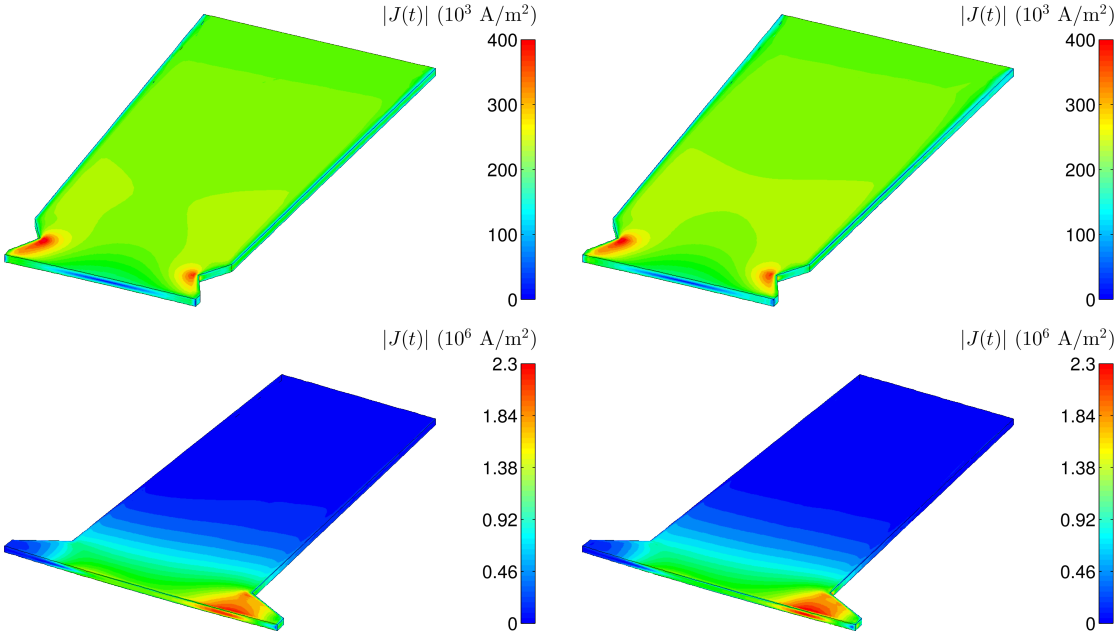

(a) $\boldsymbol{A}$,V formulation (b) $\boldsymbol{A}$,$\boldsymbol{T}$ formulation

Fig. 4.5: Current density distribution in stator tooth 8 (above) and rotor tooth 8 (below) for both formulations. Refer to Figs. 4.3 and 4.4 for numbering.

tational requirements of both the $\boldsymbol{A}$,V and $\boldsymbol{A}$,$\boldsymbol{T}$ formulation will be given in chapter 6, together with the numerical savings achieved by a harmonic decomposition method.

4.3 Total iron losses

The total iron losses, composed of classical eddy current, hysteresis and excess losses, will be compared first to two simplified loss models and then validated against no load iron loss measurements.

4.3.1 Simplified iron loss models

Two simplified iron loss models are discussed as a representative example of the numerous techniques known from the literature. The first one is the traditional model of (2.4) which is derived from the statistical loss theory. The second one is the hybrid model of (3.54) and is based on the evaluation of magnetization curves. Both models are employed as a postprocessing method.

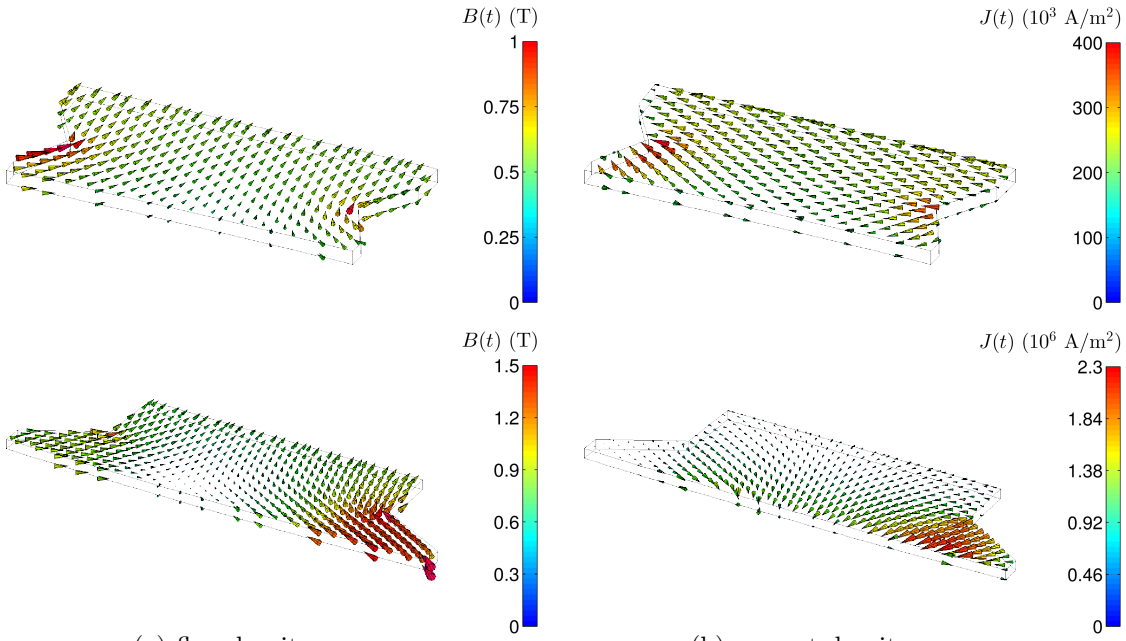

(a) flux density (b) current density

Fig. 4.6: Magnetic flux density and current density in stator tooth tip 8 (above) and rotor tooth tip 8 (below). The $\boldsymbol{A}$-V formulation has been used.

4.3.1.1 Traditional model

One of the most common techniques for the iron loss estimation in electrical machines is to apply the traditional model of (2.4) element-wise to the 2-D solution. The input flux density is thereby obtained as $B_i = \sqrt{B_{i,x}^2 + B_{i,y}^2}$, where $B_{i,x}$ and $B_{i,y}$ are the harmonic components of the flux density in x- and y-direction, respectively. The parameters in (2.4) are identified from measurements on an Epstein frame and listed in Table 4.1. The frame consists of 280×30 mm strips with a total sample mass of 1 kg. The measurements have been performed according to the IEC 60404-2 standard, which specifies the measurement procedure up to 400 Hz [192]. Measurements for higher frequencies take into consideration the IEC 60404-10 standard, too [193].

Table 4.1: Identified parameters for the traditional model

c_{hys}	c_{cl}	c_{ex}
162	$\sigma\pi^2 d^2/6 = 0.97$	3.59

The thickness and the conductivity of the sheet are given with $d = 0.5$ mm and $\sigma = 2.35\,{}^{\mathrm{MS}}/_{\mathrm{m}}$.

Fig. 4.7 compares the specific losses obtained from measurements with the results from a least square fitting procedure of (2.4). Only measurements up to 200 Hz are used for the model identification. For the sake of comparison, the calculated loss curves for 400, 500, 1000 and 2000 Hz are shown, too. The model can not be adjusted for the whole range of frequencies. Fitting for higher frequencies results in unrealistically low losses for lower frequencies and vice versa. The identified parameter set is found to be the best compromise for the current application, since it is expected that a major part of the losses is attributable to the low frequency regime.

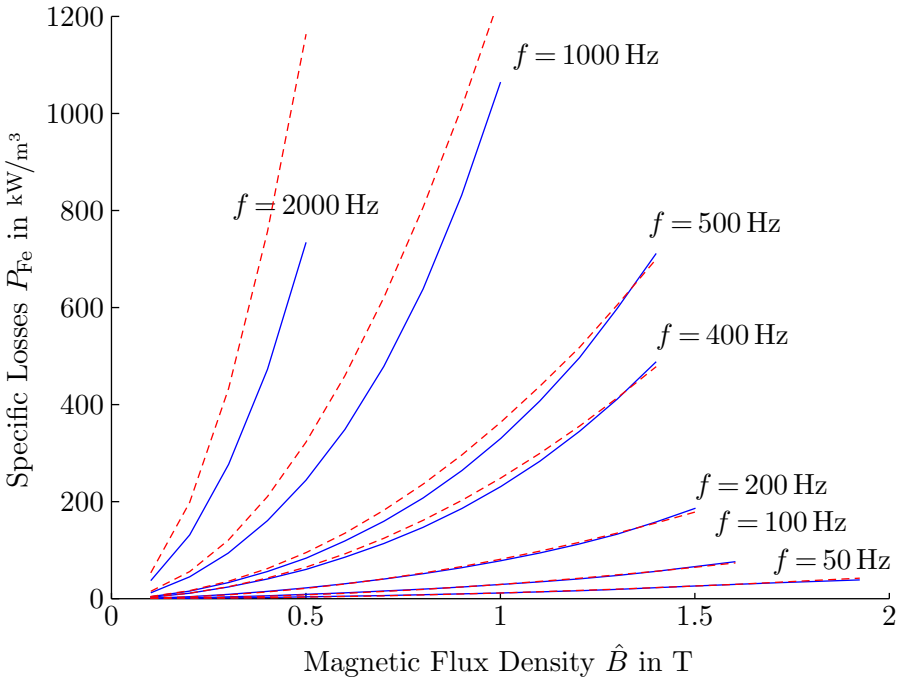

Fig. 4.7: Measured (—) and fitted (---) specific loss curves for the traditional model. The measurements have been carried out under sinusoidal flux excitation using an Epstein frame.

The main advantage of the traditional technique lies in its simplicity: only three parameters need to be identified from alternating flux measurements and the implementation is straightforward. But it is well known that the model fails when high harmonics or complex flux patterns occur. In the derivation of the classical eddy current term of (2.4) it is assumed that the lamination thickness is considerably smaller than the skin depth. However, the skin depth increases for higher frequencies particularly entailing an overestimation of the high frequency rotor losses. Inadequate modeling of the effects of minor loops leads to further deviations. Moreover, the rotational behavior of the hysteresis losses is not accounted for, because the model does not distinguish between alternating and rotational

fields. The traditional technique might be significantly improved by introducing enhanced approaches enabling proper modeling of the skin effect under high frequencies [17], minor hysteresis loops [13], or rotational losses [25]. In this work, solely the basic traditional model is examined, since it is featured to be one of the most popular iron loss models.

4.3.1.2 Hybrid model

The hybrid model of (3.54) overcomes some imperfections of the traditional method by evaluating the shape of dynamic magnetization curves. The hysteresis term in (3.54) is computed by the static vector Preisach model presented in section 3.3. The Preisach model is implemented by Everett functions constructed from first-order reversal curves which are derived from the major hysteresis loop. The major loop is approximated analytically by fitting the expression of (3.42) to BH-measurements on an Epstein frame. The measurements have been carried out under quasistatic conditions up to a flux density of 1.5 T. The number of the directions in the vector model has been set to $N_\varphi = 10$.

The dynamic parameters describing the eddy current and excess effects are identified from BH-loops measured at different frequencies. Fig. 4.8 shows the measured and fitted hysteresis characteristics; Table 4.2 summarizes the identified parameters. The hybrid model is able to accurately predict the loop shapes in a simple and efficient way, and considers further the effects of minor loops and rotational losses.

Table 4.2: Identified parameters for the hybrid model

$\overline{c}_{\mathrm{cl}}$	$\overline{c}_{\mathrm{ex}}$	a_1	a_2	α_0	α_1	B_{sat}
$\sigma d^2/12 = 0.049$	0.12	0.15	−0.018	0.91	0.055	1.5

4.3.2 Model comparison

The losses from the 3-D model serve as reference for those obtained from the simplified techniques. The results of the different models as a function of the supply current are compared in Fig. 4.9. The proportion of the eddy current losses in the rotor core is remarkable and nearly as high as in the stator. The results from the traditional technique and the 3-D model fit well for the low frequency stator losses. The hybrid model only slightly underestimates the losses. As expected, the traditional technique clearly overpredicts the high-order harmonic rotor losses, while the hybrid model gives fairly good results. The significant deviations for the traditional technique have already been noted during the identification procedure, which has demonstrated that the model can not be adjusted for a wide frequency range (see Fig. 4.7).

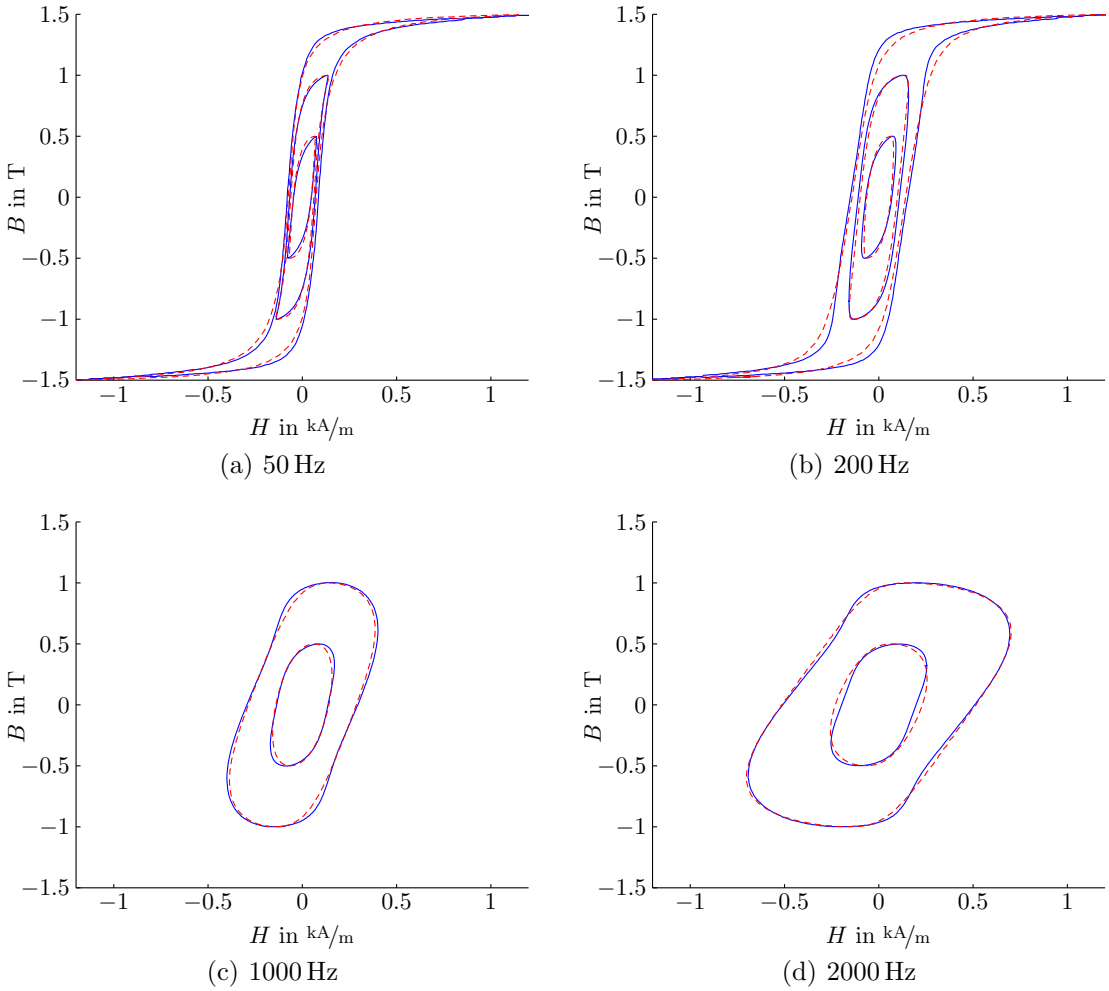

(a) 50 Hz (b) 200 Hz

(c) 1000 Hz (d) 2000 Hz

Fig. 4.8: Measured (—) and fitted (---) dynamic BH-loops obtained by applying flux densities of different fundamental frequency. The measurements have been performed with an Epstein frame. Note that the flux excitation does not necessarily need to be sinusoidal.

Fig. 4.10 segregates the different iron loss components of the simplified models. Compared to the hybrid model, the traditional one underestimates the hysteresis losses slightly, because it does not take the effects of minor loops and rotational losses properly into consideration. Similarly to the classical eddy current losses, the excess losses are clearly overestimated by the traditional technique. In the hybrid model, the excess losses account for the domains wall motion and the interdependence between hysteresis and eddy current effects [50]. It is observed that the excess losses become rather small in the non-oriented steel studied, provided that the high frequency effects are modeled correctly.

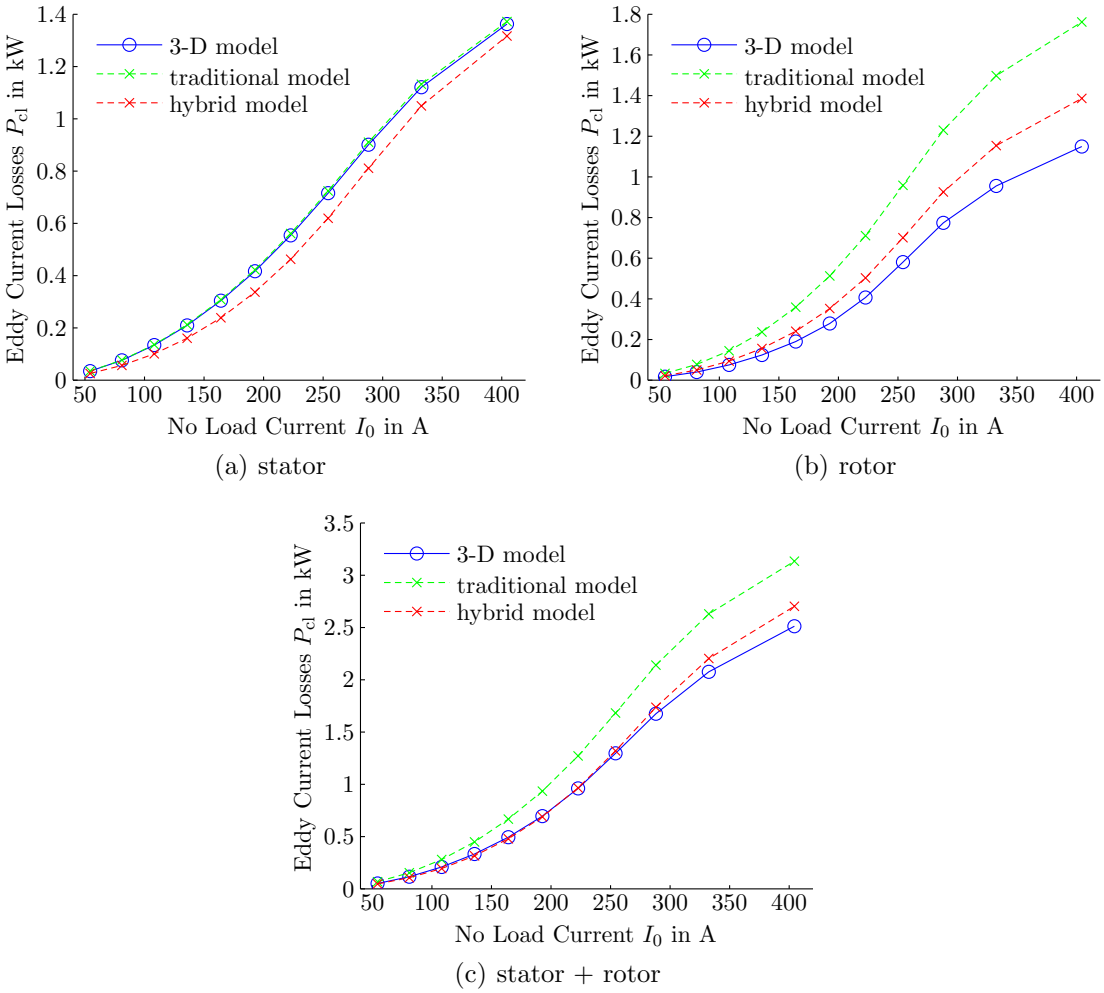

(a) stator

(b) rotor

(c) stator + rotor

Fig. 4.9: No load eddy current losses as a function of the supply current predicted by the 3-D model and the simplified models. The losses per single sheet have been multiplied by the lamination number to get the losses of the whole core stack.

4.3.3 Validation against measurements

For no load operation, the total iron losses are directly accessible by measurements based on the input-output method. The measurements have been performed with opened rotor slip-rings in order to avoid additional rotor currents. The machine under test was driven by a second machine running at synchronous speed. Thereby, the friction losses are covered by the driving machine. The iron losses are obtained by subtracting the stator winding losses from those measured on the stator terminals.

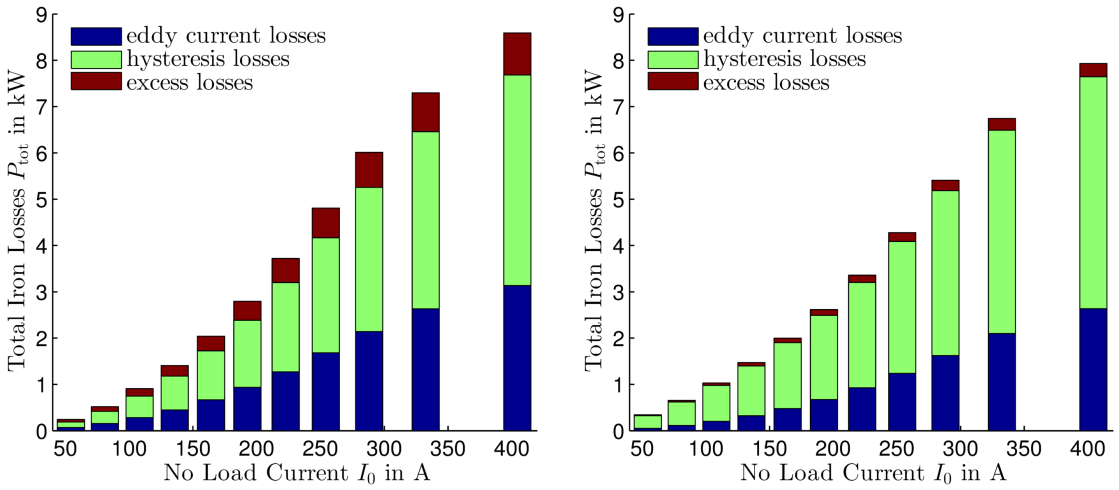

(a) traditional model (b) hybrid model

Fig. 4.10: Separated iron losses for no load operation obtained by the simplified models.

The measured and computed no load iron loss characteristics are presented in Fig. 4.11. Since the 3-D model considers the eddy current losses only, the hysteresis and excess losses are taken from the hybrid model including the vector Preisach model. The 3-D model and the hybrid technique give accurate results for a wide range of supply currents. The traditional model shows remarkable discrepancies, especially at higher currents, since it is unable to cope with the high harmonic eddy current losses in the rotor.

With increasing no load current, the flux paths tend increasingly to close into the housing and complementary construction parts. The ensuing leakage fluxes cause additional losses not accounted for in the iron loss computation. In order to assess these extra losses, a full 3-D model of the machine's end region has been set up. The end region model comprises the cores' end, the clamping system, the housing and the surrounding air. The end windings are modeled as filament currents whose excitation field is calculated by Biot Savart's law. Only the clamping plate and the frame are defined as electrically conductive. To reduce the number of unknowns in the non-conducting domains, the $\boldsymbol{T}$,Φ-Φ formulation is applied for the eddy current analysis. The analysis is performed in the frequency domain, again using hexahedral edge elements. The non-linearity of the iron cores and clamping plate is considered by an effective reluctivity approach.

Fig. 4.12 shows the eddy current loss distribution in the stator clamping plate when the 3-D model is fed by maximum current of 404 A. At higher currents, the iron cores become saturated and stray fluxes are increasingly penetrating the clamping plate. The resulting losses are also included in Fig. 4.12 explaining the differences between measured and computed iron loss values at high currents. The losses induced in the frame were found to be negligibly small when compared to those of the clamping plate, and are therefore not discussed any further.

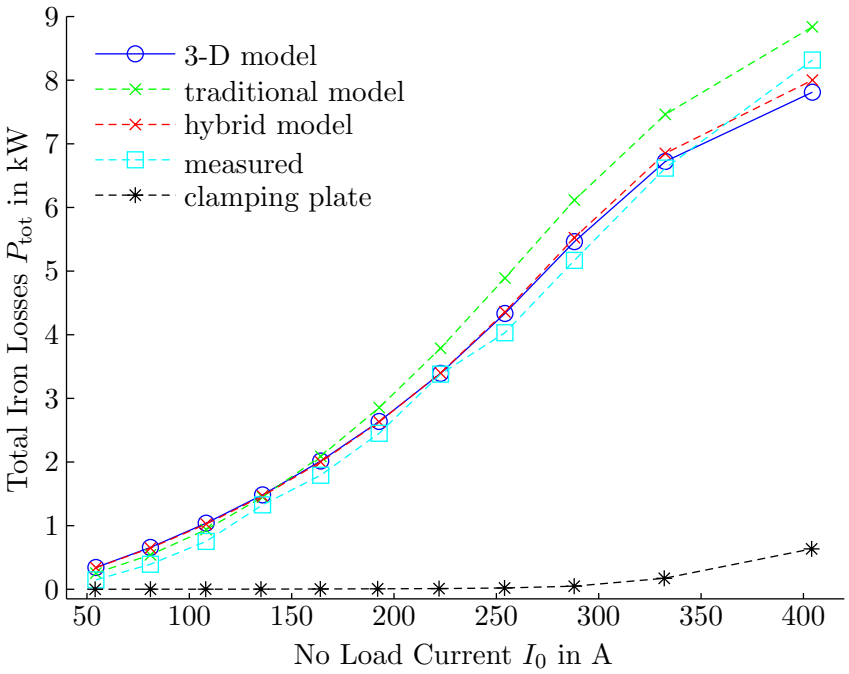

Fig. 4.11: Measured and simulated total iron losses for no load operation as a function of the supply current. The computed losses in the clamping plate are given, too.

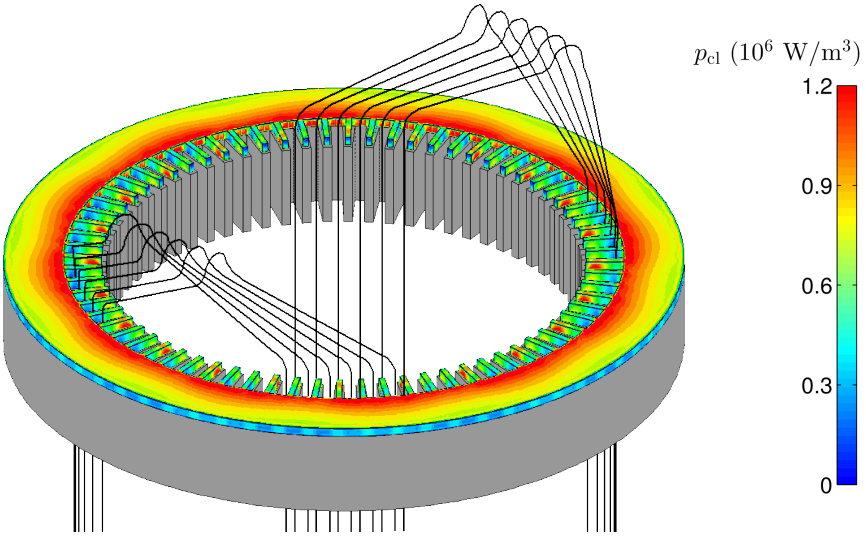

Fig. 4.12: Time-averaged eddy current loss distribution in the stator clamping plate for maximum no load current ($I_0 = 404$ A). The stator's core end and the windings of a positive phase are also shown.

5 Anisotropic generalization of vector Preisach hysteresis models

The Preisach hysteresis model employed in the previous chapter is isotropic in nature showing the same BH-characteristics in every direction. However, even the non-oriented steel used exhibits a certain amount of anisotropy which affects the field distribution and hence the iron losses. In non-oriented materials, these anisotropic effects are primarily caused by the crystal alignment during the rolling process and, to some extent, also by magnetocrystalline and shape anisotropies present in each singular particle.

The previous identification of the isotropic models has been performed by means of a standard Epstein frame whose sample strips have been cut in arbitrary directions to average the effects of anisotropy. In order to accurately assess the material's anisotropy, measurements on a rotational single sheet tester have been carried out to allow independent excitation in different directions as well as generation of spatially rotating fields.

Following the author's contributions [P3] and [P4], this chapter introduces a new generalization of the vector Preisach model in order to simulate weak bi- and uniaxial anisotropy present in non-oriented magnetic steel. The generalization is based on a modified input projection and improves the rotational loss behavior as well. Moreover, the model is combined with a simplified approach for the eddy current and excess effects, enabling studies of frequency-dependent anisotropic properties.

5.1 Anisotropy model

The vector Preisach model of section 3.3.3 applies the scalar model in each feasible direction and forms the output by superimposing the individual scalar contributions. In the inverted model, the scalar inputs are obtained by projecting the flux density vector onto the directions of interest. Here, a novel extension of the original Mayergoyz model will be introduced, by redefining the input projection of (3.52) as

$$B_{\varphi_i}(t) = |\boldsymbol{B}(t)| \cdot \delta \cdot |\cos(\varphi - \varphi_i + \psi(t))|^{1/w}, \tag{5.1}$$

where $\delta = \mathrm{sign}(\cos(\varphi - \varphi_i + \psi))$. The coefficient w has been originally proposed in [83] and implements biaxial anisotropy. Biaxial anisotropic material exhibits two equally pronounced magnetic easy axes perpendicular to each other. This type of anisotropy results

in flower-shaped H-loci when a circular flux density is applied. The angle ψ introduced here aims to incorporate uniaxial anisotropy (ψ_{aniso}) by simultaneously improving the rotational loss properties (ψ_{rot})

$$\psi(t) = \psi_{\text{aniso}}(t) + \psi_{\text{rot}}(t). \tag{5.2}$$

Both components will be detailed in the following, using the definitions below.

5.1.1 Uniaxial anisotropy

Uniaxial anisotropy is characterized by a sole magnetic easy axis, leading to elliptical field loci under rotational excitation. Introducing an additional projection angle in (5.2) leads to a new projection system which increases or decreases the input flux density of the individual scalar models. For materials exhibiting uniaxial anisotropy, ψ_{aniso} has to be π-periodic with respect to the magnetic easy axis specified by the angle θ:

$$\psi_{\text{aniso}}(t) = \Psi(\boldsymbol{B}) \sin(2(\varphi_i - \theta)). \tag{5.3}$$

Depending on the material under investigation, Ψ can be $\boldsymbol{B}$-dependent, as e. g. given in Table 5.1. One should note that besides an implicit uniaxial anisotropy in the rolling axis, further anisotropy axes may be present in the material. In such cases, their contributions are superimposed additively.

5.1.2 Improving rotational loss properties

Although the Mayergoyz model features essential vector hysteresis characteristics, it fails to represent the rotational loss properties close to saturation [84]. As discussed in chapter 2, the model produces an irreversible hysteretic behavior at high magnitudes, and therefore the losses dwell at a constant level instead of decreasing as experimentally observed. To improve the rotational loss properties, a small phase shift ψ_{rot} is introduced between the $\boldsymbol{B}$ and $\boldsymbol{H}$ vectors following the approach of [84]:

$$\psi_{\text{rot}}(t) = g(\boldsymbol{B})\text{sign}(\text{d}\varphi). \tag{5.4}$$

The real function g is introduced here as

$$g(\boldsymbol{B}(t)) = a_{\text{rot1}} \text{e}^{-a_{\text{rot2}}(|\boldsymbol{B}(t)| - B_{\text{rot}})^2} + \psi_0, \tag{5.5}$$

in which a_{rot1}, a_{rot2}, B_{rot} and ψ_0 are constant parameters identified from rotational loss measurements. The first term in (5.5) is based on a Gaussian distribution function enabling the representation of the rotational behavior near B_{rot}. The angle ψ_0 is independent of the flux density and ensures that the $\boldsymbol{B}$ and $\boldsymbol{H}$ vectors become parallel at saturation.

5.1.3 Dynamic extension

The dynamization of the static model is again based on the hybrid approach of section 3.3.4. Since a uniform distribution of the eddy currents in the cross section is assumed, an isotropic flux density projection $B_{\varphi_i}^{\mathrm{iso}}$ is supplied to the hybrid model of (3.54):

$$H_{\varphi_i}(t) = H[B_{\varphi_i}(t)] + \overline{c}_{\mathrm{cl}}\delta_{\mathrm{e}} \left| \frac{\mathrm{d}B_{\varphi_i}^{\mathrm{iso}}(t)}{\mathrm{d}t} \right|^{\gamma} + \overline{c}_{\mathrm{ex}}\delta_{\mathrm{e}} \left| \frac{\mathrm{d}B_{\varphi_i}^{\mathrm{iso}}(t)}{\mathrm{d}t} \right|^{0.5} . \tag{5.6}$$

The exponent γ reads:

$$\gamma(B_{\varphi_i}(t)) = a_0 + a_1\delta_{\mathrm{e}} \left(\frac{\mathrm{d}B_{\varphi_i}^{\mathrm{iso}}(t)}{B_{\mathrm{sat}}} \right) + a_2 \left(\frac{\mathrm{d}B_{\varphi_i}^{\mathrm{iso}}(t)}{B_{\mathrm{sat}}} \right)^2 , \tag{5.7}$$

and $\delta_{\mathrm{e}} = \mathrm{sign}(\mathrm{d}B_{\varphi_i}^{\mathrm{iso}}/\mathrm{d}t)$. The isotropic input projection is obtained by setting $w = 1$ and $\psi = 0$ in (5.1), which thus reduces to its basic form of (3.52). The parameters of the dynamic model are again identified from BH-loops measured in different directions.

5.2 Identification results

The magnetic characteristics of the non-oriented steel grade used have been measured under alternating and circular flux using a rotational single sheet tester. The studied specimens have been cut from three different positions on the steel strip, located in the center and near the opposing edges. Since almost no differences have been observed in the magnetic properties of the different specimens, only results for the middle sample will be presented in the following.

The used measurement setup (see [194] and Fig. 5.1 for details) consists of a personal computer equipped with a data acquisition card, instrumentation and power amplifiers, and the tester itself. The yoke of the tester is an ordinary stator core of an induction motor carrying a special two phase winding. The yoke construction minimizes leakage fluxes allowing high field homogeneity even at high induction levels and in any magnetization direction. Slot effects are pronounced in the layer close to the air-gap, but do not influence the field homogeneity in the inner measurement region [195].

The magnetic flux density is measured by two orthogonal B-coils wound trough 0.8 mm holes in the sample. The H-components are determined by cross coils ($20 \times 20\,\mathrm{mm}^2$ measuring area, 2 mm thick) placed on the sample surface. Since the magnetic field intensity decays with the distance from the sample, the H-coils have been mounted as close to the surface as structurally possible. The inevitable distance between the sensors and the sample surface results in too low measured H-values leading to a softer BH-behavior than observed in the Epstein frame measurements of chapter 4. However, the BH-loop area,

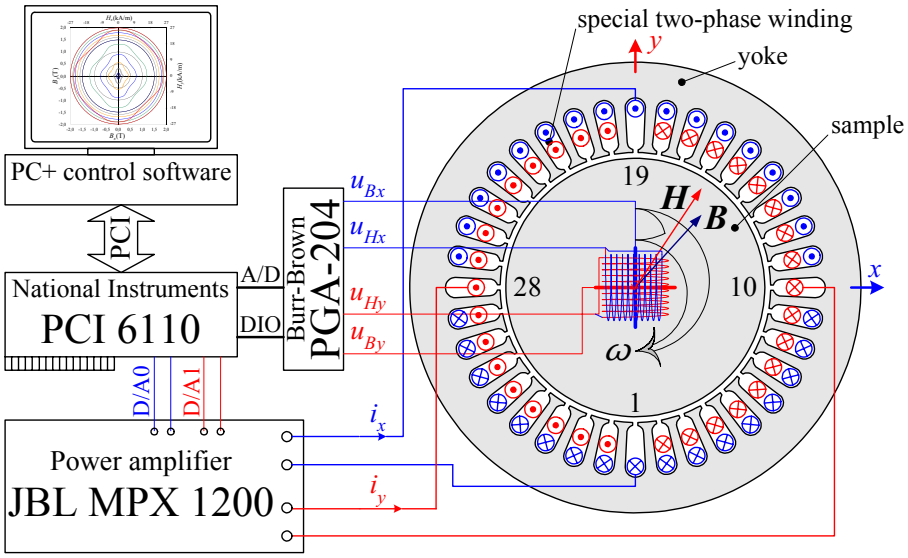

Fig. 5.1: Measurement system with personal computer, data acquisition card (PCI 6110) with two 12 bit D/A converters and four 16 bit A/D converters, stereo power amplifier (JBL MPX 1200), instrumentation amplifier (PGA-204) controlled by DIO port, and the rotational single sheet tester. The sample diameter is 78 mm, the stator inner diameter 81.5 mm [194].

and hence the losses, obtained by both systems show no notable difference (see Fig. 5.2), endorsing the general validity of the proposed setup. The evaluation of the field intensity can be improved by employing a biaxial array of hall sensors [196], or by sandwiching the H-coils between two sample sheets [197].

The induced voltages in the B-coils are amplified and fed to a iterative feedback control. The computerized control system allows to generate arbitrary flux density waveforms varying with frequencies up to 2 kHz. The attainable peak flux density is given with 2 T for frequencies up to 100 Hz, and decreases for higher frequencies owing to the limited output power of the stereo amplifier.

5.2.1 Static hysteresis

First, the anisotropy parameters in (5.1) and (5.3) are identified using alternating measurements in different directions spread by 15° increments. The measurements have been carried out at low frequencies, for which the effects of the eddy currents are negligible. The model identification is based on a least square method which fits the simulation results to the measured data by adjusting the parameters w and Ψ. The scalar Everett function initially needed in the vectorization procedure is obtained by supplying an angularly av-

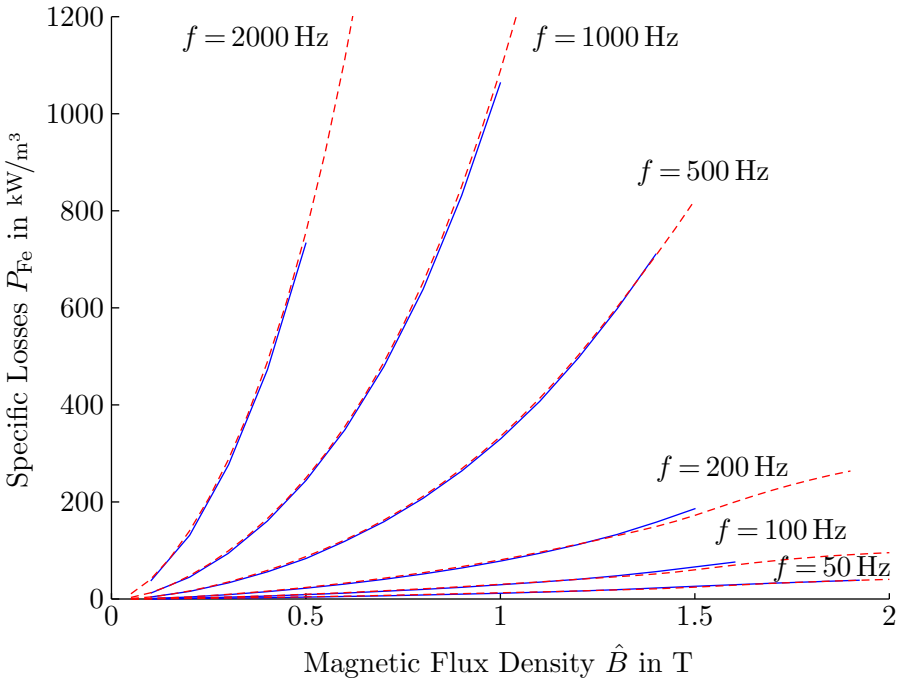

Fig. 5.2: Specific losses measured by the Epstein frame (—) and the rotational single sheet tester (---) . The losses from the rotational single sheet tester are obtained by averaging the alternating losses in different directions. The rotational single sheet tester achieves higher induction levels over the entire frequency range.

eraged major loop to the algorithms described in section 3.3. In the identification of the vector Everett function, (3.53) can also be modified according to the generalized input projection, leading to spatially dependent Everett data, such as used in [101] or [102]. In this work, (3.53) is kept in its original form, maintaining the Everett data isotropic. Considering the anisotropic effects subsequently during the field projection avoids lengthy identification algorithms and keeps the model implementation simple and efficient.

The vector hysteresis model has been identified for $N_\varphi = 16$ directions using measurements up to flux densities of 1.7 T. Beyond the major loop, a non-hysteretic single-valued magnetization curve has been employed. The single-valued extension is constructed by cubic spline interpolation between the end point of the BH-curve and the maximum measured flux density of 2 T [182].

The identified anisotropy parameters are summarized in Table 5.1. Besides a biaxial anisotropy ($w = 0.94$), two directions of uniaxial anisotropy are apparent in the material: a strong anisotropy in the rolling direction (x-axis), and a rather small one around $\theta = -45°$. The form of the Ψ-functions is obtained from basic observations on the the angular dependency of the H-loci. The associated constants are obtained by the least square identification procedure mentioned above.

Table 5.1: Identified uniaxial anisotropy parameters

axis	Ψ	θ
1	$0.30\left[1-\left(\frac{\lvert\boldsymbol{B}(t)\rvert}{B_{\mathrm{iso}}}\right)^2\right]$	0°
2	$0.013\lvert\boldsymbol{B}(t)\rvert^2$	-44.4°

At $B_{\mathrm{iso}}=2\,\mathrm{T}$ the anisotropy in rolling direction decreases to zero.

Fig. 5.3 compares the simulated and measured field intensity obtained under purely circular flux density rotating in clockwise direction. No significant difference has been noted between the measurements in clockwise and counterclockwise direction. The used steel exhibits remarkable uniaxial anisotropy in rolling direction, which is especially pronounced for low flux densities and decreases towards saturation. Biaxial anisotropy becomes notable at higher induction levels and results in flower-shaped field loci with four peaks.

Owing to anisotropy, the phase lag between the $\boldsymbol{B}$ and $\boldsymbol{H}$ vectors varies with the angular position. In particular, under rotational excitation, the changing phase lag modifies the hysteresis loop area, and thus the losses. Fig. 5.4 shows the measured and simulated BH-loops in x- and y-direction, when the material is exposed to circular field with a constant amplitude of 2 T. Due to symmetry, only a half of the hysteresis loops is presented in the plot. In y-direction, the ascending branch of the BH-loop intersects the descending branch leading to a negative loop area. No intersection is detected in x-direction causing an enlargement of the hysteresis area. Consequently, the losses in y-direction become negative while those in x-direction increase. In total, the losses balance each other and drop to zero at saturation, as seen in Fig. 5.7(b).

The prediction of the rotational losses has been further improved by adding the phase lag of (5.4) to the anisotropy angles. The corresponding parameters, listed in Table 5.2, are determined by fitting the computed static loss curve to the measured one. The correction angle reaches its maximum of 1.92° at $B_{\mathrm{rot}}=1.4\,\mathrm{T}$, and decreases to 0.15° for flux densities above 1.8 T.

Table 5.2: Identified parameters for rotational loss improvement

a_{rot1}	a_{rot2}	B_{rot}	ψ_0
0.031	30.8	1.4	0.0026

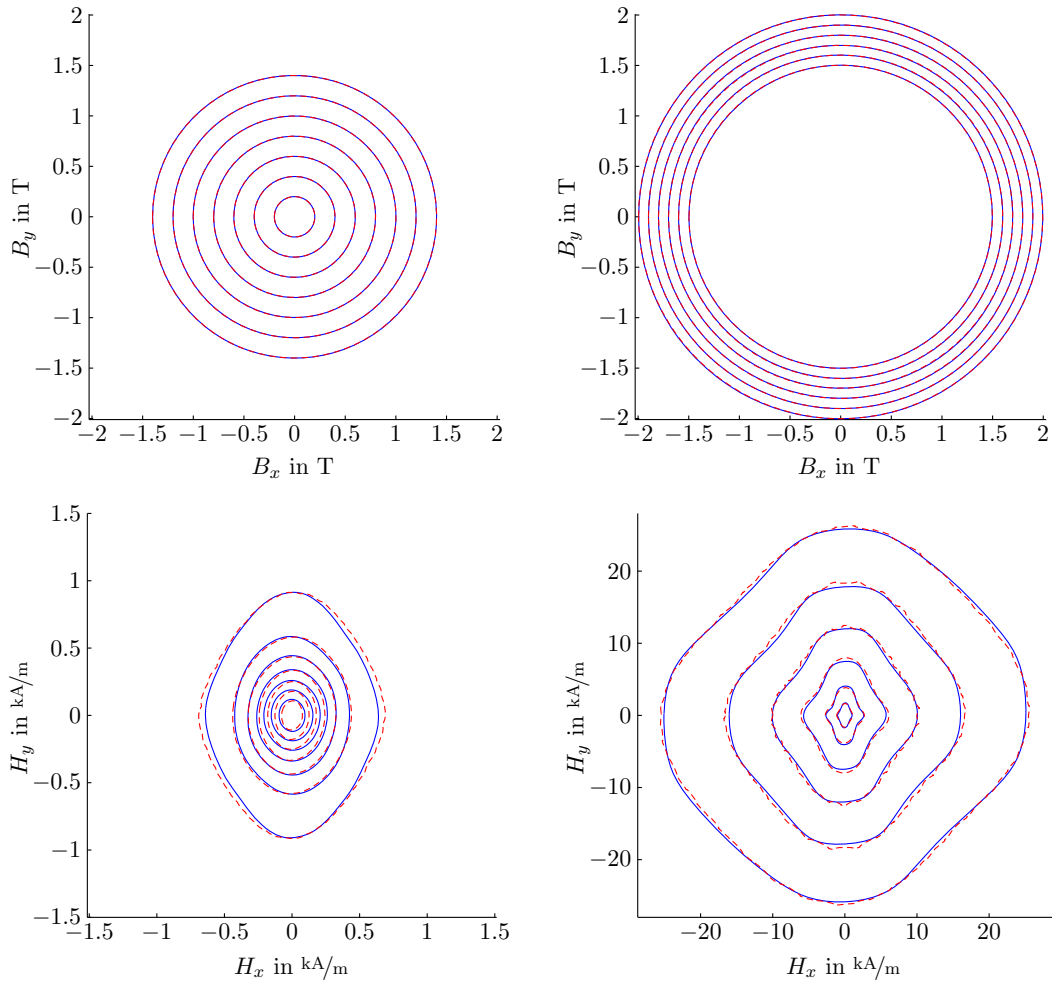

(a) 0.2 T - 1.4 T (b) 1.5 T - 2.0 T

Fig. 5.3: Measured (—) and simulated (---) loci of flux density (above) and field (below) under static and rotational excitation. The amplitude of the flux density has been increased in 0.2 T steps (a) and 0.1 T steps (b), respectively.

5.2.2 Dynamic hysteresis

After implementing the static model, the dynamic one is identified from BH-loops measured over a wide range of frequencies. The dynamic parameters obtained are given in Table 5.3 and differ slightly from those of the hybrid model in section 4.3.1.2. This is explained by the fact that hysteresis loops alternating in multiple directions directions have been used in the identification. Further differences are caused by the softened BH-behavior due to the inaccuracy in H-sensing, but also substantiated by the higher B_{sat} value specified.

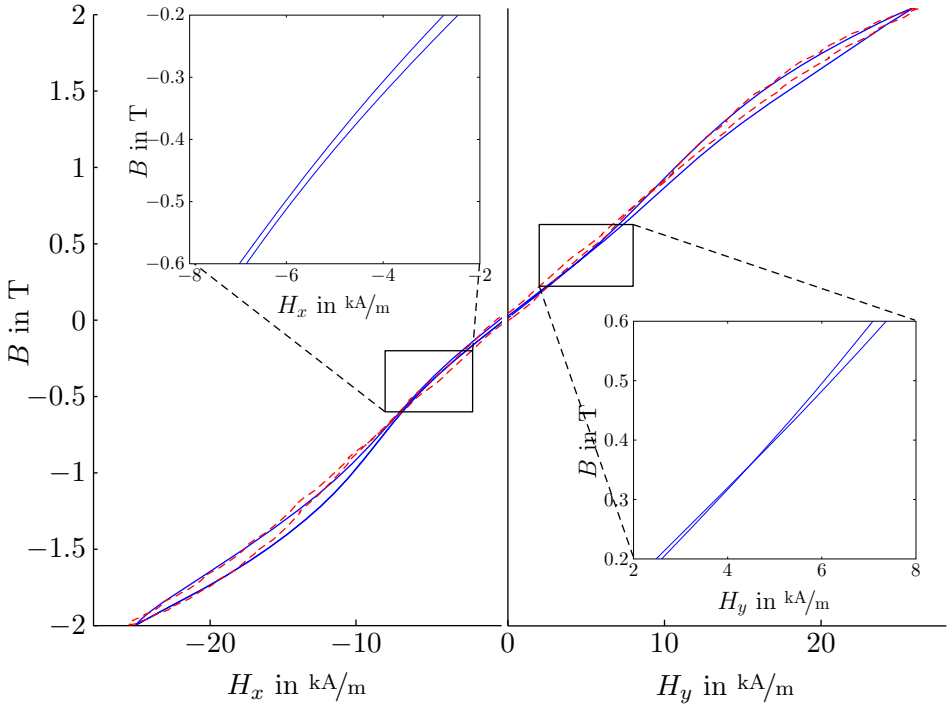

Fig. 5.4: Measured (—) and simulated (---) BH-loops for a static, clockwise rotational flux density of 2 T. Only the measurement results are shown in the zoomed section for sake of better visibility. The corresponding losses in x-direction are $+2.99\,\mathrm{kJ/m^3}$ (measured) and $+2.78\,\mathrm{kJ/m^3}$ (simulated), those in y-direction $-2.73\,\mathrm{kJ/m^3}$ (measured) and $-2.75\,\mathrm{kJ/m^3}$ (simulated).

The measured and fitted BH-characteristics under alternating flux excitation in x- and y-direction are shown in Fig. 5.5. The anisotropy decreases with increasing frequency, since the field components related to the eddy current and excess effects are distributed uniformly along the angular position. This effect can be examined especially well under rotational conditions, as presented in Fig. 5.6. The deflection of the H-loci in the y-direction is due to the fact that the field intensity induced by the eddy currents leads to an additional H_x-component. Its sign depends on whether the field intensity is increasing or decreasing, resulting in opposite inclination angles between clockwise and counterclockwise rotation.

Table 5.3: Identified parameters for the dynamic anisotropy model

$\overline{c}_{\mathrm{cl}}$	$\overline{c}_{\mathrm{ex}}$	a_1	a_2	α_0	α_1	B_{sat}
0.049	0.15	0.24	−0.015	0.95	0.042	1.7

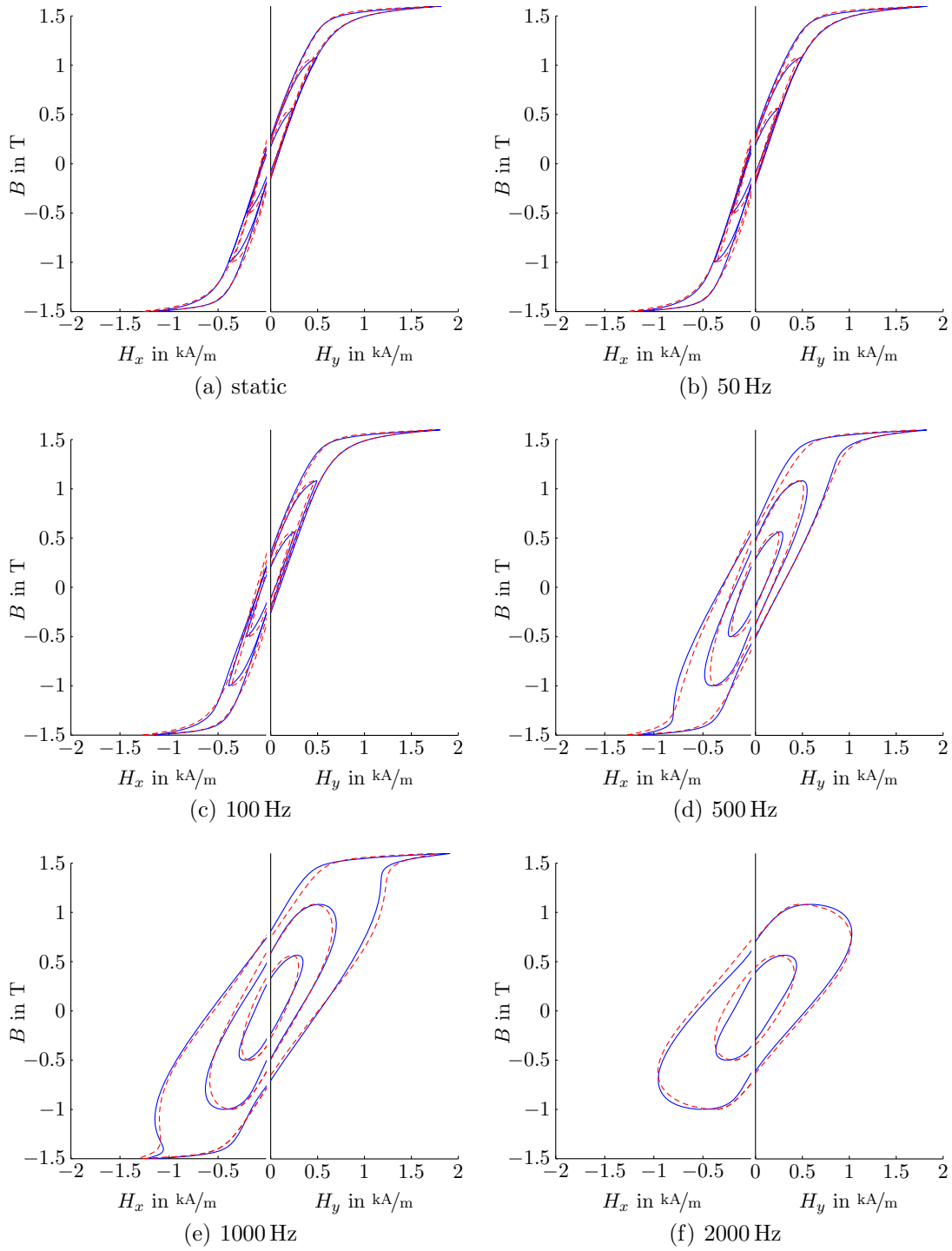

Fig. 5.5: Measured (—) and simulated (---) BH-loops for alternating excitation varying with different frequencies.

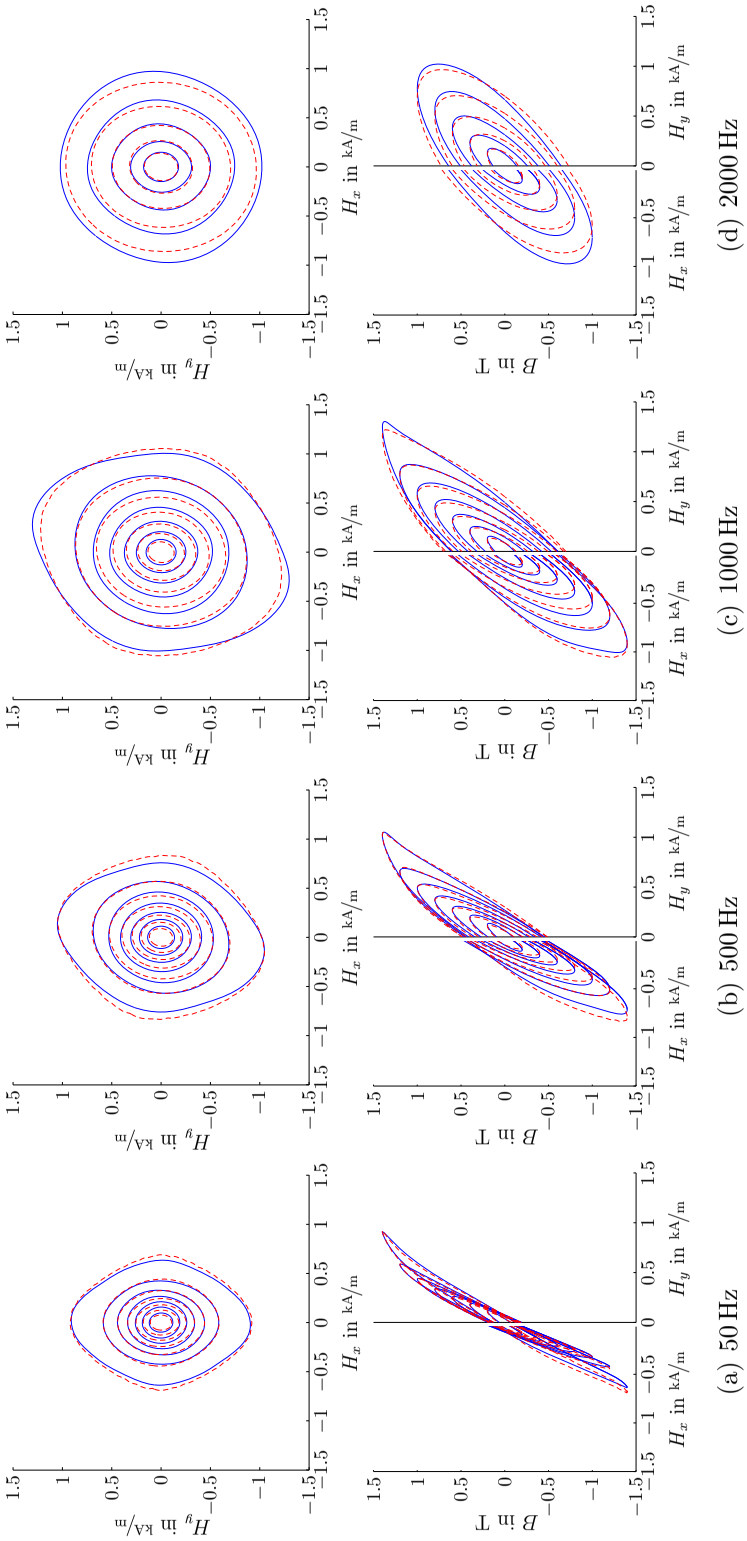

(a) 50 Hz (b) 500 Hz (c) 1000 Hz (d) 2000 Hz

Fig. 5.6: Measured (—) and simulated (- - -) field loci (above) and corresponding BH-loops (below) under clockwise rotational excitation for different frequencies. The amplitude of the flux density has been increased from 0.2 T to 1.4 T in 0.2 T steps.

5.2.3 Losses

Fig. 5.7 presents the energy losses obtained by evaluating the BH-loop area. Under static conditions, the loss curves are consistent with the theoretical considerations and experimental results of section 3.1.1. For low flux densities, the rotational losses are higher than the alternating ones until they drop to zero at saturation. With increasing frequency, in particular the rotational losses rise significantly, becoming nearly twice as high as in the alternating case.

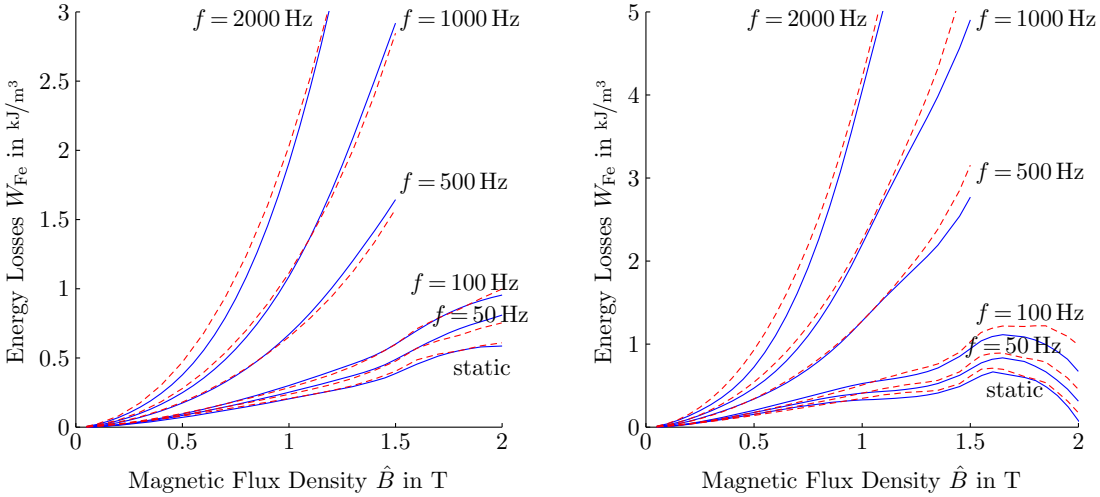

Fig. 5.7: Measured (—) and simulated (---) iron losses for different frequencies under alternating and rotational flux excitation.

5.3 Effects of anisotropy and rotational fields on the machine's iron losses

The methods proposed aim to investigate the impact of anisotropy and rotational effects on the iron loss behavior of rotating electrical machines. The evaluation of anisotropic effects requires their consideration in the 2-D field analysis, either as an anisotropic single-valued BH-curve, or even by coupling the field solution to the hysteresis model. The implementation of methods to account for magnetic anisotropy in the 2-D analysis would exceed the scope of this work. Therefore, the effects of anisotropy on the machine's iron losses are not discussed any further and will be addressed in future research. It is expected that anisotropy might impact the local iron loss distribution in the laminations, but its overall effect will be averaged along the core length since the individual sheets are usually rotated stepwise for one slot pitch.

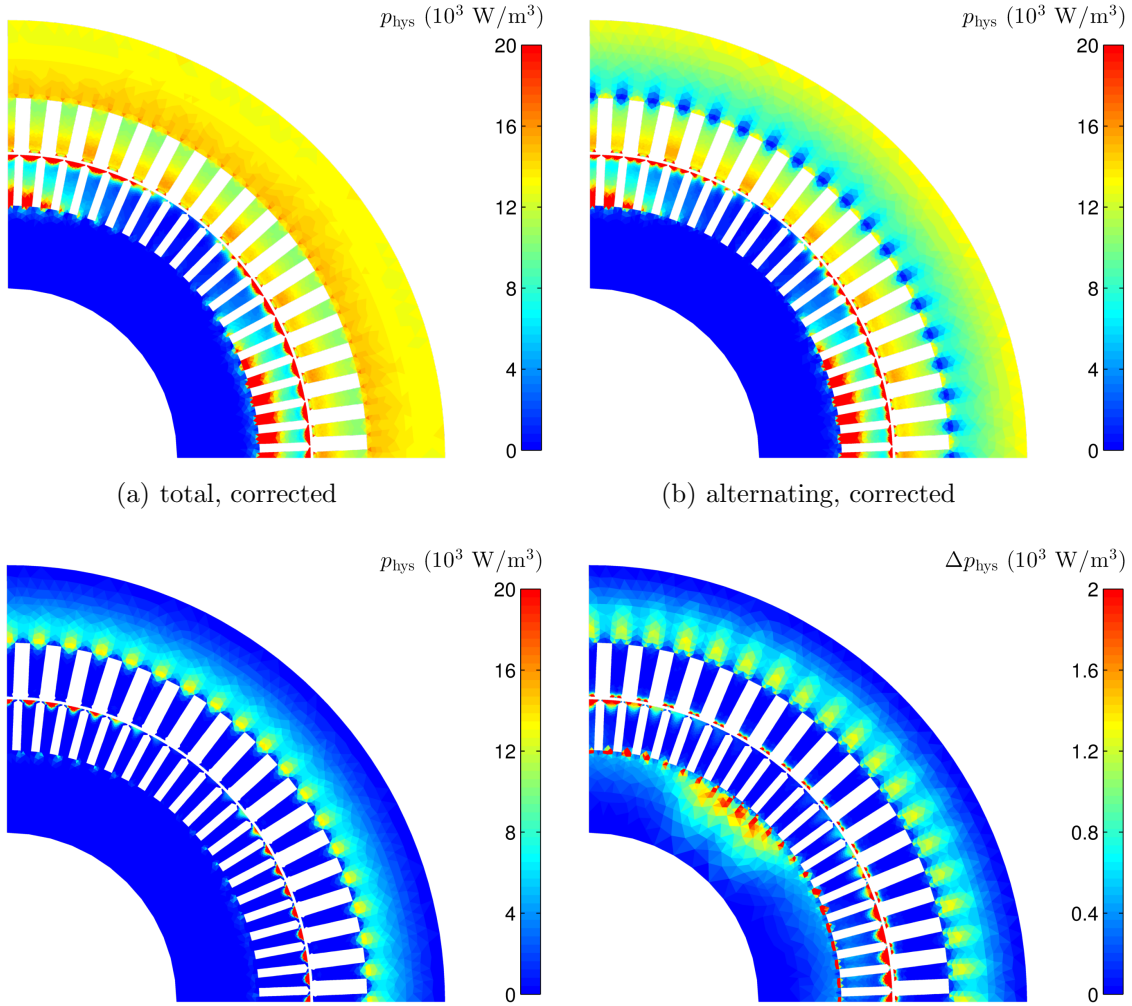

(a) total, corrected

(b) alternating, corrected

(c) rotating, corrected

(d) rot., increase without correction

Fig. 5.8: Breakdown of hysteresis losses in alternating and rotating contributions as well as increase of the rotating component when no phase lag correction is applied ($p_{\mathrm{no\,corr}} - p_{\mathrm{corr}}$). The total hysteresis losses of 3.24 kW separate into 2.55 kW for the alternating and 0.69 kW for the rotating components. Applying the original approach without correction, the rotational losses increase by about 20 %, while the alternating ones remain almost unaffected (+0.72 %).

In order to study the rotational loss improvement introduced in section 5.1.2, the computed hysteresis losses will be compared to the original Mayergoyz model. Fig. 5.8 shows the separated hysteresis loss components for the previously investigated induction machine, obtained by applying the vector Preisach model to the no load 2-D solution. In the vector model, the input projection has been kept isotropic and corrected by the phase

lag of (5.4). The rotational losses are mostly concentrated in the tooth roots and tips, and account for about 20 % of the total hysteresis losses. Using the original Mayergoyz approach, the rotational losses remain constant at saturation, leading to higher losses than with the proposed correction (see Fig. 5.8(d)). In total, the hysteresis losses rise only by 4.79 %, since the emerging fields in the machine are rarely purely circular, contributing thus to relatively low rotational losses.

6 Additional losses due to loading and skewing

The previous analyses were limited to no load operations only. When load is getting applied, the flux patterns in the machine become increasingly distorted leading to elevated iron losses. Although the fundamental flux density components generally decrease by increasing the load, the iron losses increase due to the emergence of high-order field harmonics. In machines with skewed rotor bars, the axial field distribution becomes non-uniform under load entailing a redistribution of the losses along the core length. Especially in larger machines, the effects of skewing can result in an overall increase of the total machine losses.

In this chapter, the dependence of the core losses on the effects of loading and skewing will be studied by gathering findings of the author's publications [P5–P8]. In [P5] and [P6], the 3-D eddy current distribution in the steel sheets has been evaluated for various loading conditions. In addition, a harmonic decomposition method has been introduced effectively reducing the computational burden of the original 3-D time-stepping method of chapter 4 by solving a few time-harmonic problems instead. The works of [P7] and [P8] have investigated the effects of skewing on the axial iron loss distribution and compared the obtained losses to the ones of a machine with straight rotor bars.

Different loading conditions examined during the standard machine tests will be analyzed. In these tests, the stator terminals of the machine are supplied with sinusoidal voltage and the slip-rings of the rotor windings are short-circuited. The load is specified by a second machine coupled to the shaft of the machine under test. In the transient 2-D simulations for the whole machine, the operating condition is specified via a constant rotor speed and the stator current. The iron loss models are again applied a posteriori to the 2-D solution.

6.1 Frequency domain decomposition of the transient 3-D eddy current problem

Solving the 3-D eddy current problem of a steel sheet in the time domain entails high computational costs, since the high field frequencies call for fine numerical discretization in terms of space and time. The ensuing numerical burden can be significantly reduced by

substituting the non-linear time-stepping procedure with linear time-harmonic evaluations of dominant frequency components.

6.1.1 Eddy current formulations in frequency domain

The harmonic analyses are carried out independently in parallel for different field frequencies ω_k. Rewriting the $\boldsymbol{A}$-V formulation of (3.33) for the time-harmonic case using complex notation yields

$$\begin{aligned} \nabla \times (\nu \nabla \times \boldsymbol{A}) + \mathrm{j}\omega_k \sigma \boldsymbol{A} + \mathrm{j}\omega_k \sigma \nabla V &= \boldsymbol{0}, \\ -\nabla \cdot (\mathrm{j}\omega_k \sigma \boldsymbol{A} + \mathrm{j}\omega_k \sigma \nabla V) &= 0. \end{aligned} \tag{6.1}$$

For the $\boldsymbol{A}$,$\boldsymbol{T}$ formulation, the governing equations of (3.38) become

$$\begin{aligned} \nabla \times (\nu \nabla \times \boldsymbol{A}) - \nabla \times \boldsymbol{T} &= \boldsymbol{0}, \\ \nabla \times \left(\frac{1}{\sigma} \nabla \times \boldsymbol{T} \right) + \mathrm{j}\omega_k \nabla \times \boldsymbol{A} &= \boldsymbol{0}. \end{aligned} \tag{6.2}$$

The actual saturation level of the machine is considered by defining the reluctivity ν using the field's peak values from the non-linear transient 2-D simulations performed in advance

$$\nu = \left. \frac{\max\{|H_{\text{2-D}}(t)|\}}{\max\{|B_{\text{2-D}}(t)|\}} \right|_T . \tag{6.3}$$

The magnetic field intensity and flux density in a 2-D element, $H_{\text{2-D}}$ and $B_{\text{2-D}}$, are evaluated over a period of the fundamental line frequency. The reluctivity is assumed as constant for consecutive 3-D elements extruded from the 2-D mesh. Therewith, the variation of the reluctivity in axial direction is neglected. The same reluctivity values are used for all time-harmonic analyses.

After solving the harmonic problems, an arbitrary field value at a specific time instant $X(t)$ is obtained by superposition of the individual frequency components $X(\mathrm{j}\omega_k)$ in proper phase relation

$$X(t) = \mathrm{Re}\left\{ \sum_{\omega_k} X(\mathrm{j}\omega_k) \cdot \mathrm{e}^{\mathrm{j}\omega_k t} \right\}. \tag{6.4}$$

6.1.2 Boundary conditions for the harmonic problems

The specification of boundary conditions discussed in chapter 4 can be adopted in a straightforward manner to time-harmonic problems. In order to excite the individual

harmonic models, the transient 2-D magnetic vector potential needs to be decomposed into its spectral components. Considering induction machines, all possible field frequencies can be determined a priori using analytical approaches, see e. g. [198] and [199]. The electromagnetic field in a slip-ring induction machine with integer slot windings can be expressed by a sum of rotating field components having the spatial azimuthal order r, the frequencies ω^{s} in a stator coordinate system, and ω^{r} in a moving rotor coordinate system

$$\begin{aligned} r &= p(1 + 6g_{\mathrm{s}} + 6g_{\mathrm{r}} + 2k_{\mathrm{sat}}), \\ \omega^{\mathrm{s}} &= \omega_0(1 + 6g_{\mathrm{r}}(1 - s) + 2k_{\mathrm{sat}}), \\ \omega^{\mathrm{r}} &= \omega^{\mathrm{s}} - (1 - s)\frac{r}{p}\omega_0. \end{aligned} \tag{6.5}$$

Here, p stands for the pole pair number of the machine and $\omega_0 = 2\pi f_0$ is the line frequency. The slip value s is defined by the mechanical speed of the rotor. The integer values g_{s} and g_{r} belong to the field components generated by slotting effects and the discrete winding distribution. The index s corresponds to the stator, and r to the rotor. The integer variable k_{sat} is related to saturation effects.

Since the field frequencies caused by the asynchronous rotor movement do, in general, not coincide with multiples of the fundamental frequency, the commonly applied discrete Fourier transform leads to erroneous results due to leakage effects. Therefore, the method of [199] is used, which replaces the Fourier transform straight to the frequency domain by a two-step approach: first, a Fourier transform is performed in azimuthal direction, yielding the spatial characteristic for different ordinal numbers r. Then, the frequency components are computed for each spatial order using a least square algorithm. As the individual field components are clearly separated by their spatial order, even closely spaced spectral lines can be determined correctly avoiding leakage and aliasing effects.

6.1.3 Field harmonics

Fig. 6.1 shows the frequency spectrum of the magnetic flux density in a tooth tip, obtained by applying the procedure of [199] to the 2-D solution. The simulations have been carried out for various loads, rising from 0 % up to 125 % of the rated torque. A whole period of the fundamental line frequency divided in 1000 time steps has been used for the frequency domain evaluation. One should note the close but distinct spectral lines, especially prominent in the rotor, which can not be resolved properly by a conventional Fourier transform. The dominant spectral lines near the 3rd, 5th and 7th multiples of the fundamental frequency are induced by saturation effects and the discrete winding distribution. Additionally, slotting effects cause notable high harmonics arising next to 2100 Hz in the stator, and 1800 Hz in the rotor tooth. Further slot harmonics appear near 4200 and 3600 Hz. As the machine draws more current under load, the frequency components due to winding and slotting enlarge.

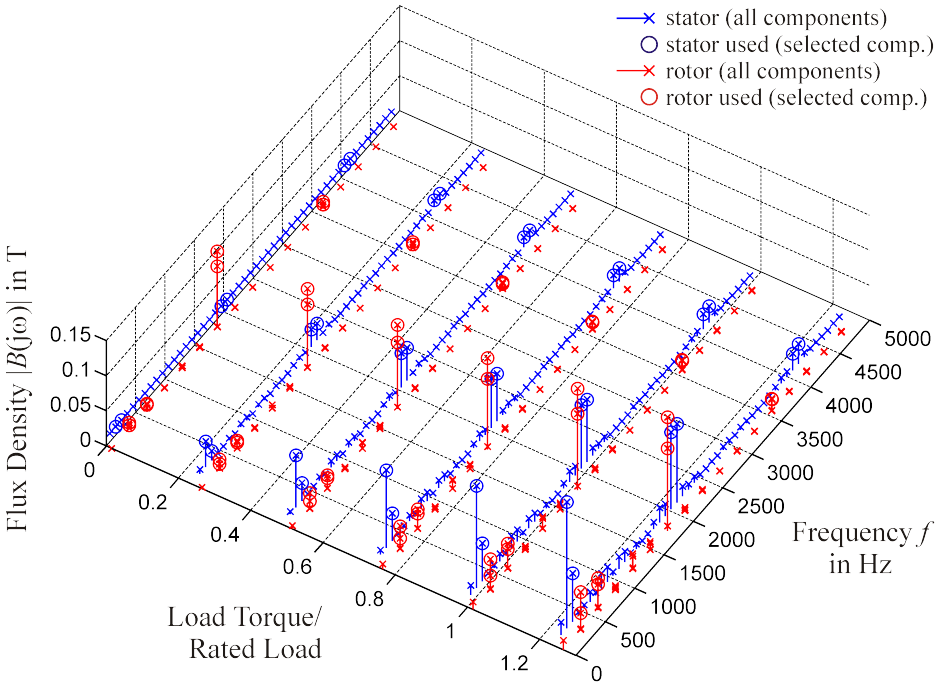

Fig. 6.1: Load-dependent frequency spectrum of the radial component of the flux density observed in a stator and rotor tooth tip of the 2-D model. The fundamental frequency components are not shown, the rotor frequencies are given in the rotor coordinate system. The crossed spectral lines indicate all occurring components, the circles mark the selected set used in the time-harmonic method.

The circled spectral lines in Fig. 6.1 indicate the frequency components accounted for in the time-harmonic computations. The associated frequencies are obtained by substituting the integer values

$$\begin{aligned} g_\mathrm{s} &= -2\frac{N_\mathrm{s}}{6p}, -\frac{N_\mathrm{s}}{6p}, -1, 0, +1, +\frac{N_\mathrm{s}}{6p}, +2\frac{N_\mathrm{s}}{6p}, \\ g_\mathrm{r} &= -2\frac{N_\mathrm{r}}{6p}, -\frac{N_\mathrm{r}}{6p}, -2, -1, +1, +2, +\frac{N_\mathrm{r}}{6p}, +2\frac{N_\mathrm{r}}{6p} \end{aligned} \tag{6.6}$$

into (6.5), and neglecting saturation effects ($k_\mathrm{sat} = 0$). The stator and rotor slot numbers are given by $N_\mathrm{s} = 72$ and $N_\mathrm{r} = 84$. Together with the fundamental frequency component at $f_0 = 50\,\mathrm{Hz}$, seven frequencies have been considered in the harmonic simulations for the stator sheet. For the rotor sheet, the fundamental component emerging at low frequencies sf_0 has not been accounted for, since it induces negligible losses. Thus, a set of eight frequencies has been used for the rotor lamination. Considering more frequencies led to no significant improvement in the loss evaluation.

6.1.4 Eddy current losses

Fig. 6.2 compares the 3-D eddy current loss distribution in the sheets obatined by the harmonic superposition method to the one obtained by a time-stepping analysis. Excellent agreement is achieved between the transient and harmonic approach. Under load, the stator losses are due to both the fundamental and high frequency fields. The fundamental frequency losses are again distributed uniformly within the lamination, while the high-order frequency losses are concentrated in the teeth and their tips. The rotor losses are primarily caused by high-order fields near the air-gap. Since not a complete period of the fundamental rotor field is captured in the simulations, the loss distribution alters in circumferential direction. However, the averaged loss values differ in the per mill range compared to the results for a complete period, which can be easily obtained by summing up the time-harmonic solutions over a whole rotor period.

The eddy current losses integrated over the sheet volume are given in Fig. 6.3. As observed in Fig. 6.1, the high-order field harmonics rise with the applied load, resulting in

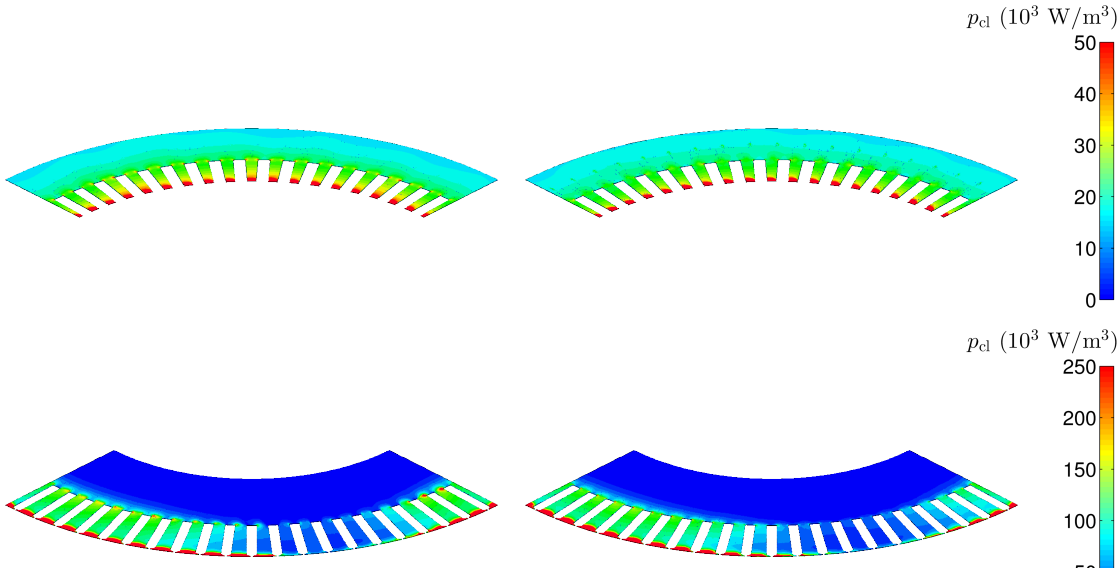

(a) time-stepping (b) harmonic superposition

Fig. 6.2: Time-averaged eddy current loss density computed by a time-stepping analysis and by the harmonic superposition principle for the stator (above) and rotor sheet (below). The simulations have been carried out for rated load, the losses have been averaged over a period of the fundamental line frequency. The $\boldsymbol{A}$,V formulation has been used in both time and frequency domain, the $\boldsymbol{A}$,$\boldsymbol{T}$ formulation in the frequency domain.

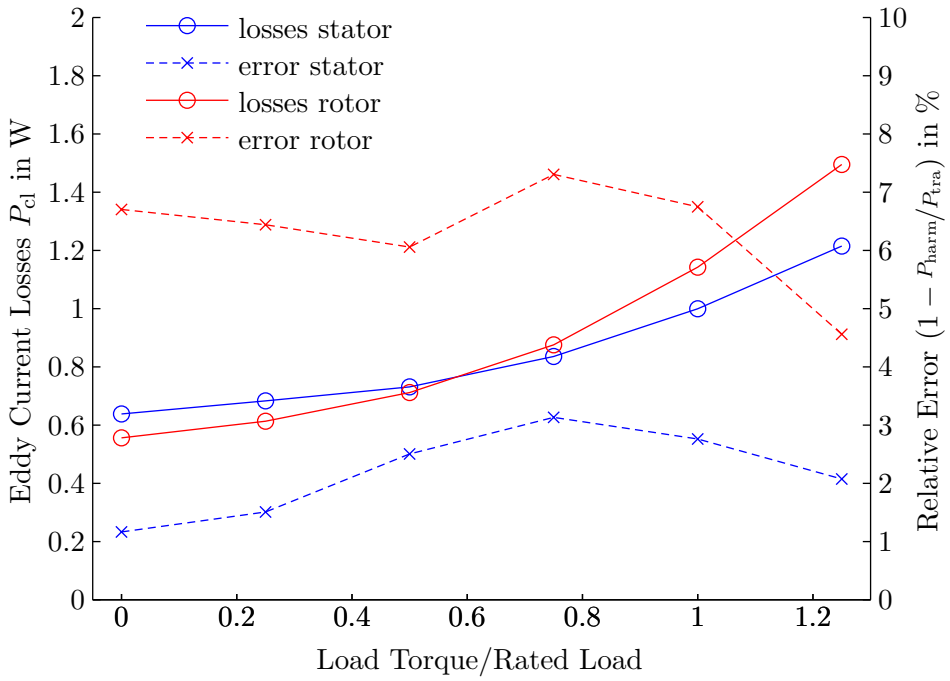

Fig. 6.3: Eddy current losses per sheet for different loads computed by a time-stepping analysis and relative error to the results of the harmonic superposition method.

elevated losses. In particular, the rotor losses do strongly increase, since they are mainly induced by high-order frequency fields. The relative difference in losses obtained by the transient and the time-harmonic analysis is plotted on the right axis of Fig. 6.3. Using the proposed limited set of frequencies, the error ranges between 1 % to 3 % for the stator and 4 % to 8 % for the rotor sheet. The harmonic superposition method gives slightly lower loss values, because not all frequency components are covered within the analysis.

6.1.5 Computational requirements

Table 6.1 lists the elapsed simulation times for the transient and harmonic 3-D problems, when conjugate gradient techniques are applied. The time-stepping methods require several days of computation. Once reaching the steady state after 20 to 30 time steps, a whole period of the fundamental line frequency comprising 1000 time steps has been simulated. Under low load, a good loss estimation can already be achieved by evaluating some tens of steps, since the steady state losses remain almost constant over time. Small variations are caused by high frequency effects. With increasing load, the loss variations due to the high frequency fields rise, requiring considerably more time steps to ensure a reliable loss determination. The $\boldsymbol{A}$,V formulation solves the transient problem significantly faster than the $\boldsymbol{A}$,$\boldsymbol{T}$ one, because it involves about 35 % less degrees of freedom (DOF).

Table 6.1: Computational data for the original transient 3-D analysis and the harmonic superposition method

	stator sheet				rotor sheet			
domain	transient		harmonic		transient		harmonic	
formulation	$\boldsymbol{A}$,V	$\boldsymbol{A}$,$\boldsymbol{T}$	$\boldsymbol{A}$,V	$\boldsymbol{A}$,$\boldsymbol{T}$	$\boldsymbol{A}$,V	$\boldsymbol{A}$,$\boldsymbol{T}$	$\boldsymbol{A}$,V	$\boldsymbol{A}$,$\boldsymbol{T}$
number of elements	47736	47736	47736	47736	60732	60732	60732	60732
DOF (mio.)	0.66	1.02	0.66	1.02	0.84	1.30	0.84	1.30
assembly time (h)	202	310	0.01	0.03	227	380	0.01	0.04
solution time (h)	245	329	0.94	0.32	222	412	1.11	0.77
total CPU time (h)	448	638	0.95	0.35	449	792	1.12	0.82
number of linear iterations	-	-	3523	567	-	-	3083	1003
losses (mW)	1000	1018	971.8	972.0	1142	1198	1064	1065

Simulations for rated load. The same convergence criteria have been set in the stator and rotor sheet simulations, respectively. An Intel Xeon computer running at 2.00 GHz has been utilized.

The harmonic superposition approach requires just a fraction of time compared to the original time-stepping method. Since the harmonic problems are treated in parallel, the times in Table 6.1 are given for the simulation with the longest time needed. For the $\boldsymbol{A}$,$\boldsymbol{T}$ formulation, the number of linear iterations, and hence the total CPU time, is about the same over the whole frequency range. The $\boldsymbol{A}$,V formulation needs considerably more iterations as the frequency increases, since the satisfaction of the natural boundary condition ensuring that the normal component of the current density is zero on the lamination boundaries becomes more cumbersome. Within the $\boldsymbol{A}$,$\boldsymbol{T}$ formulation, this condition is specified explicitly by the tangential component of $\boldsymbol{T}$. Consequently, this formulation converges in much less iterations when applied to higher frequencies. Compared to the $\boldsymbol{A}$,V formulation, the $\boldsymbol{A}$,$\boldsymbol{T}$ one solves the harmonic problems faster, although a larger number of degrees of freedom is required. Using the $\boldsymbol{A}$,$\boldsymbol{T}$ formulation, about 60 % of the total simulation time can be saved for the stator, and about 30 % for the rotor sheet.

6.2 Effects of skewing

The rotor bars of the machine investigated are skewed for one stator slot pitch. The effects of skewing are studied by coupling the iron loss models to a multi-slice model of the machine. The multi-slice model consists of five equidistantly placed slices whose rotor bars are externally coupled through an electrical circuit.

6.2.1 Axial loss variation

In a skewed machine, the phase of the rotor field with respect to the stator field changes along the machine axis. The superposition of the two fields yields a non-uniform flux density distribution [111]. For the investigated cases, the fundamental component of the flux density rises steadily along the core length. This effect increases with the load and leads to axially varying iron losses. Fig. 6.4 shows the computed eddy current losses in the

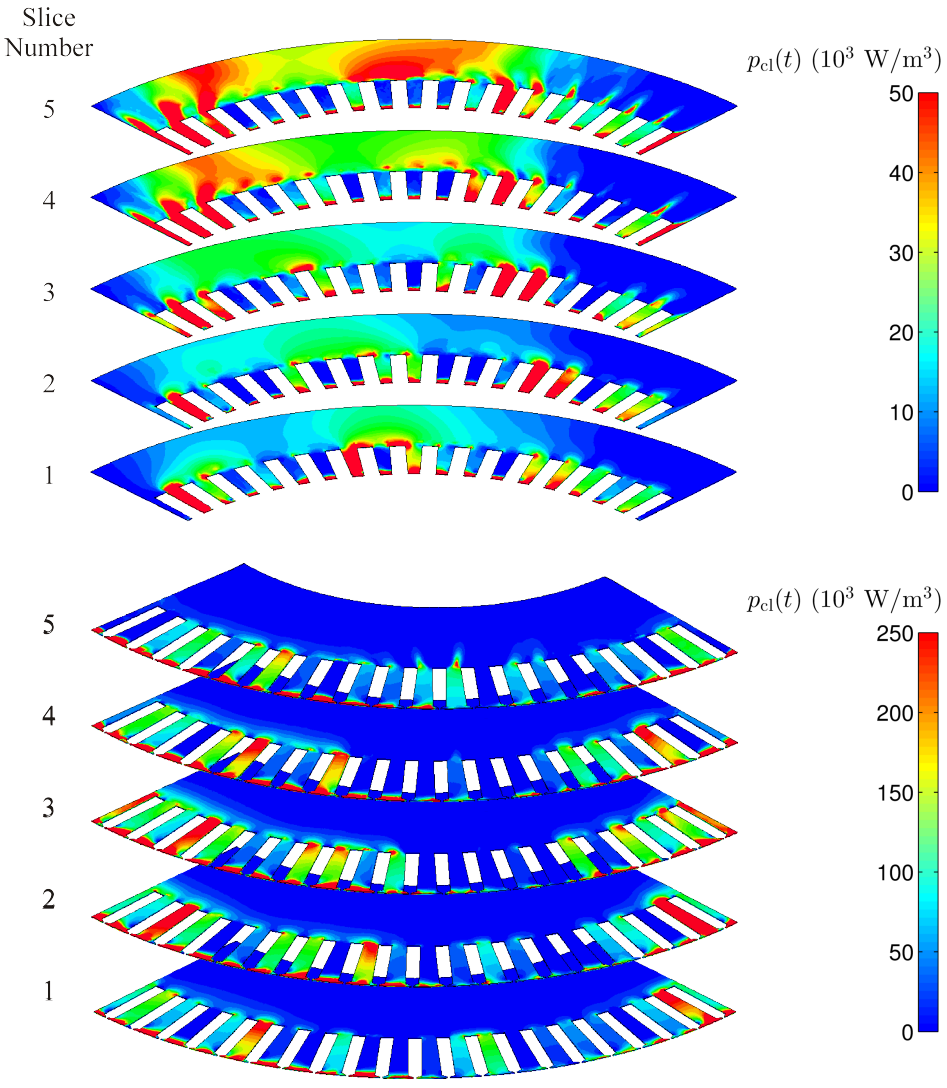

Fig. 6.4: Eddy current loss distribution in the stator (above) and rotor (below) sheets for a five-slice model at a specific time instant and rated load.

sheets obtained by performing the 3-D analysis for every slice. In the stator laminations, the fundamental frequency losses increase considerably with the slice number, while the high-order harmonic losses change to a less extent along the machine length. The axial variation of the loss distribution in the stator and rotor teeth is explained by a change in the reluctance of the flux paths for different teeth positions in the slices.

The axial iron loss behavior under varying load is detailed in Fig. 6.5. The hysteresis losses are again computed by a static vector Preisach model neglecting any anisotropic effects. Overall, the axial loss variation increases with the load. For rated load, the total iron losses in the fifth stator slice are about 100 % higher than in the first one. For the rotor core, this non-uniformity is less pronounced, but still amounts to about 50 % between the outermost slices.

Under no load, the skew has a negligible influence on the axial loss distribution, owing to the absence of the rotor field. Slight variations are caused by a change in the reluctivity of the magnetic circuit along the machine length. The iron losses in the individual stator slices differ up to 0.18 % compared to those obtained from a single-slice model representing a non-skewed machine. For the rotor slices this difference is up to 0.14 %. The small variations justify the utilization of a single-slice model for the no load case.

As observed previously, the general loss increment under load is due to the growing high-order field harmonics. Compared to the eddy current losses, the hysteresis losses in the stator core are less affected by the load. This is beacuse the fundamental field component under load is increasingly damped by the rotor field resulting in a diminished major hysteresis loop. The ensuing loss decrease is partly balanced by the effects of minor loops which are originating from higher harmonics. In contrast, the hysteresis losses in the rotor are almost exclusively caused by minor loops and increase thus with the applied load (see also Figs. 7.6 to 7.8).

6.2.2 Comparison to a straight machine

The sum of losses for the skewed machine, presented in Fig. 6.6(a), is compared in Fig. 6.6(b) to those of a machine with straight rotor bars. Although the differences between the iron loss results are rather small, a general increase in the stator losses and a decrease in the rotor losses can be observed for the skewed machine. The copper losses in the stator and rotor winding rise slightly, since the skewed machine has a lower power factor, which requires higher currents to provide the same output torque. The high frequency copper losses in the massive rotor bars are not significantly influenced by the skew. This is due to the fact that the rotor bars of the studied machine are lying remarkably deep in the slots, preventing the penetration of the stator slotting fields. Hence, no significant rotor joule loss decrease is apparent in the skewed machine. The sum of the iron and winding losses in the stator and rotor, designated as the total losses, increases by up to 1.22 % for the skewed variant.

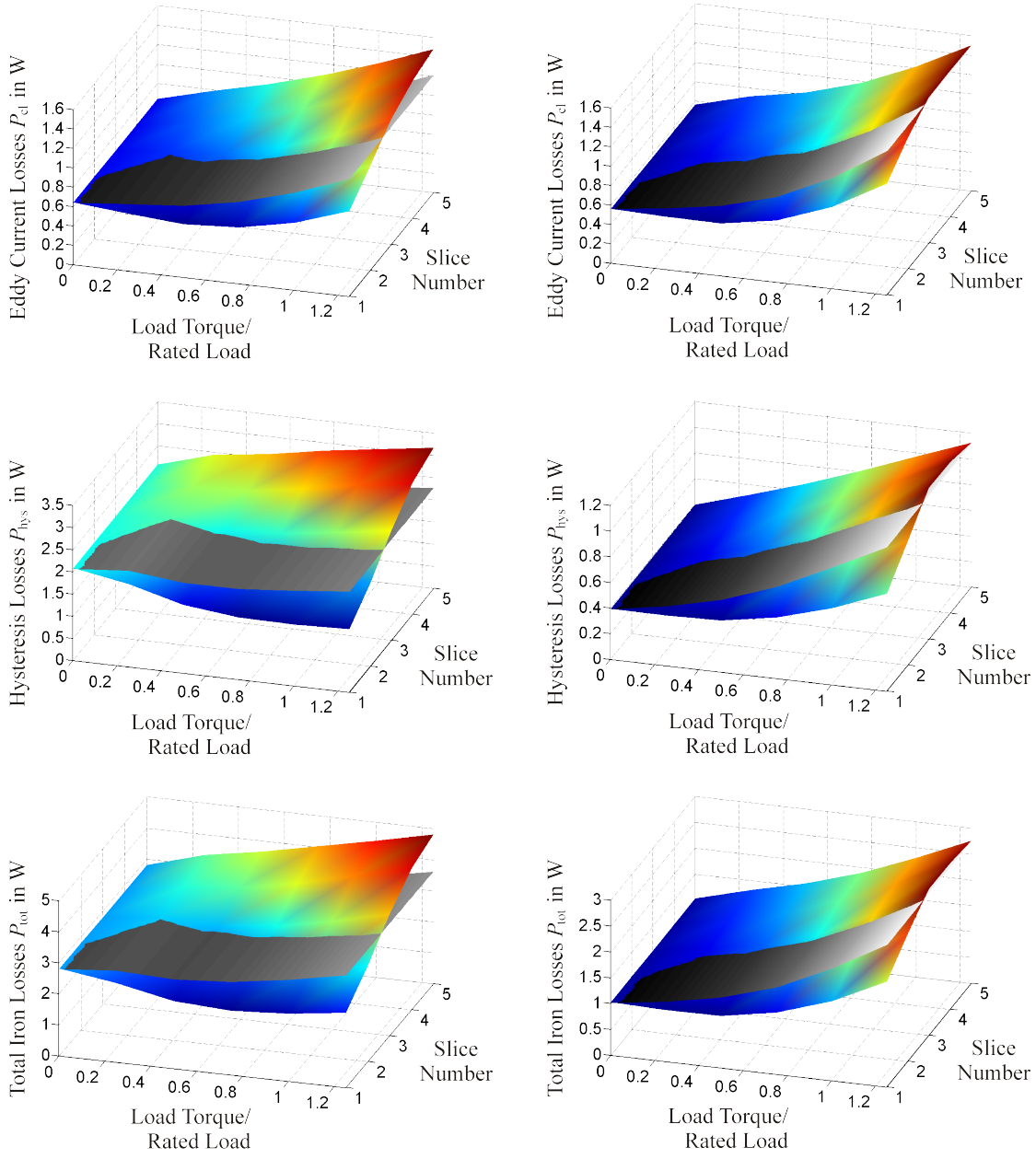

(a) stator (b) rotor

Fig. 6.5: Eddy current, hysteresis and total iron losses for different slice numbers and loading conditions. The colored surfaces represent the losses for the skewed machine, the gray ones those for the non-skewed variant. The given values refer to a single sheet; a cubic spline interpolation is used between the slice positions.

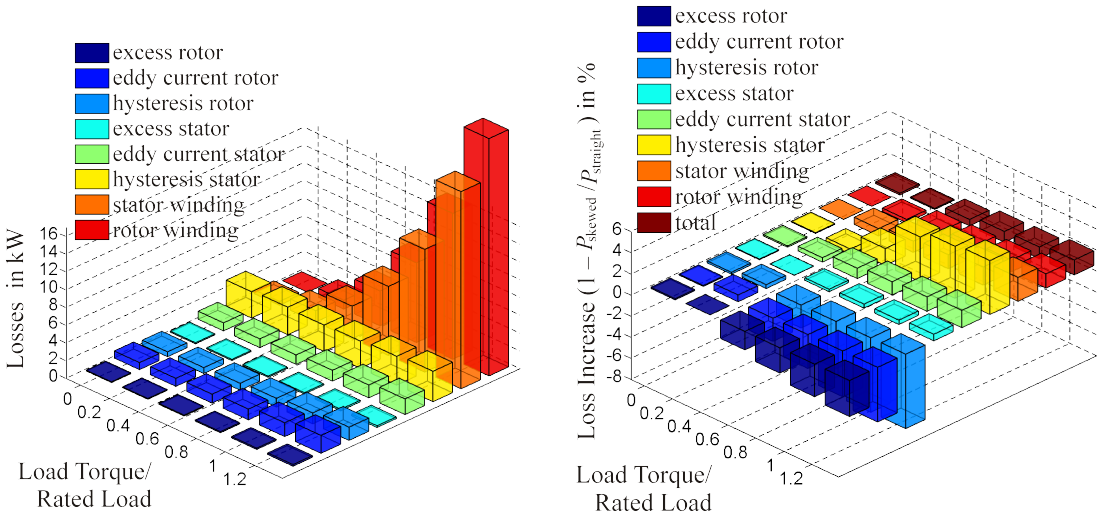

(a) skewed variant

(b) increase to straight variant

Fig. 6.6: Losses computed for the skewed machine and their increase compared to the straight variant. The loss sum is obtained by adding the losses of all slices.

The small differences in the total losses justify the omission of the skewing effects from previous computations. The overall iron losses can be estimated with high accuracy using a single-slice model of a non-skewed machine. Therefore, the investigations in the next chapters will also employ a single-slice model taking benefit of less computational expenses. However, the axial variation in the iron losses should be considered during the thermal design process.

7 Additional losses due to inverter supply

During the past decades, variable speed drives operated with frequency converters have become a de facto standard solution in many industrial applications. Such inverter fed systems enable, on the one hand, to efficiently optimize the machines' speed and torque characteristics over a wide range of operating regimes. On the other hand, the non-sinusoidal supply evoked by the frequency converter leads to additional machine losses and, thus, to thermal problems. In particular the iron losses in the steel sheets significantly increase due to additional eddy currents in the laminations and the presence of minor hysteresis loops under distorted flux.

This chapter extends the previous analyses to the effects of PWM voltage supply on the machine's iron loss characteristics by recapping the conference contribution [P9]. The examined slip-ring topology enables for studies of inverter supply on the stator terminals, as well as operations in doubly fed mode. Doubly fed concepts are largely used in wind power applications to adapt the mechanical speed provided by the wind turbine to the electrical frequency needed in the power grid. Thereby, electrical power is supplied to the machine's rotor terminals by means of a frequency converter. The additional losses under rotor-sided inverter supply behave differently compared to the stator fed ones, and are therefore evaluated on a comparative basis.

7.1 Inverter fed machine model

The effects of inverter supply are investigated by coupling the 2-D finite element model of the machine to a frequency converter model. Two different configurations running under various loading conditions will be analyzed. For clarity, their modeling will be treated separately in the following.

7.1.1 Stator fed operation

Again, no load and rated load operations performed during the standard machine tests will be studied. In order to assess the iron loss increase between sinusoidal and PWM supply, an inverter fed machine model, as sketched in Fig. 7.1(a), has been set up. In contrast to the previous analyses, the stator terminals of the machine are voltage fed via an external electrical circuit. The computational burden is alleviated by neglecting

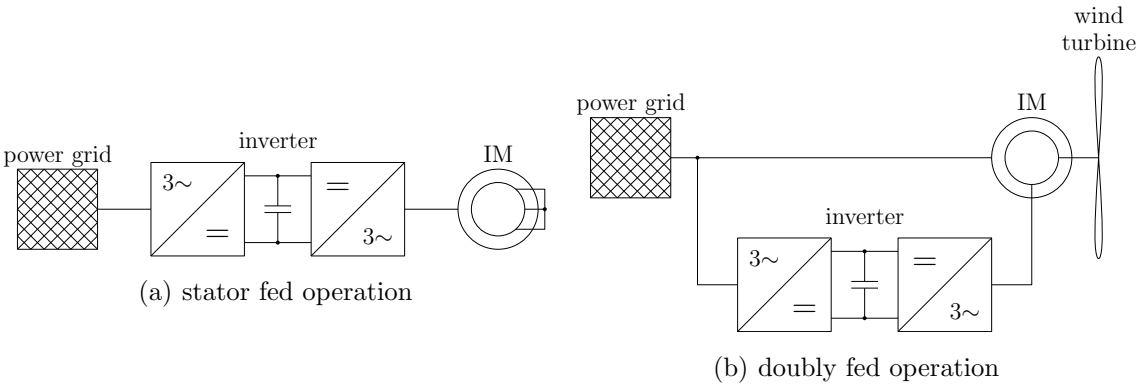

Fig. 7.1: Operation modes under investigation. Induction machines (IM) in topology (a) are commonly used in motor applications, whereas topology (b) is a typical wind power application becoming economically competitive in the megawatt range.

eddy current effects in the rotor windings and by using a single-slice model representing a non-skewed machine.

The finite element model is coupled to a MATLAB/Simulink [200] environment which provides the PWM voltage. The modeled inverter topology is a voltage sourced two-level converter consisting of three half-bridges. The switching elements are assumed to be ideal omitting any parasitic effects. The PWM signal generation is based on a space vector modulation using a software determined switching pattern [201]. Fig. 7.2 shows the simulated PWM voltage and the corresponding frequency spectrum. In all cases investigated, the dc-link voltage is given with 1100 V, and the switching frequency with $f_c = 2250\,\text{Hz}$. To accurately detect all switching operations, the time steps in the transient computation have been kept fixed to $\Delta t = 1/(30 f_c)$, which corresponds to 1350 equidistant steps during a 50 Hz fundamental period. The finite element machine model is invoked in each time step, starting transients are again avoided by a harmonic pre-simulation.

7.1.2 Doubly fed operation

In wind power applications with doubly fed machines (see Fig. 7.1(b) and [202]), electrical power is added or discharged to the machine's rotor terminals. Whenever the speed of the wind turbine becomes over-synchronous, power is carried over the rotor-sided inverter to the grid. In sub-synchronous operation, active power is supplied to the rotor and fed back to the grid along with the mechanical turbine power. Unlike topologies with stator-sided inverters, only a fractional amount of the total plant power is carried over the converter taking advantage of smaller inverter dimensioning.

The finite element model of the machine as well as the PWM algorithms are handled in the same way as discussed above. To ensure a correct field formation during doubly fed

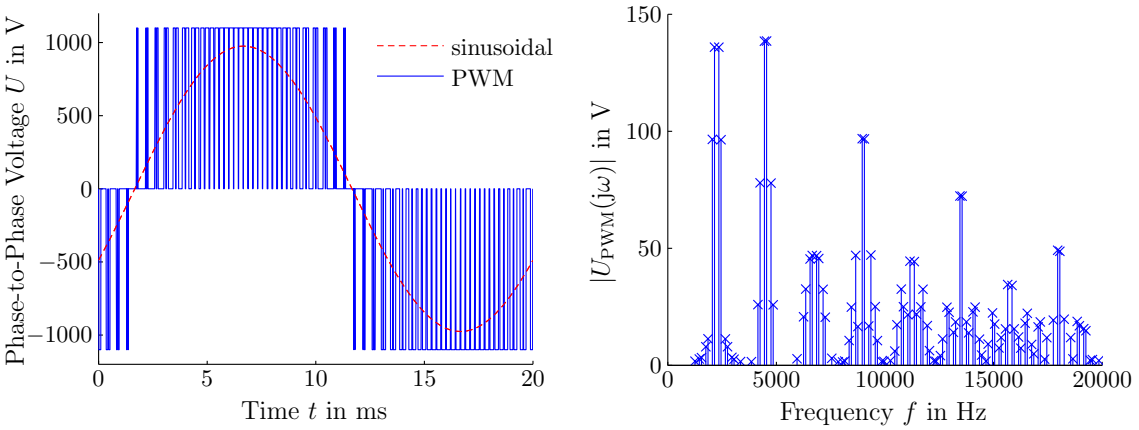

(a) time function (b) frequency spectrum

Fig. 7.2: Stator PWM voltage with sinusoidal reference in time and frequency domain. The fundamental frequency component of 690 V is not shown in the spectrum. The harmonic components induced by the inverter are chiefly pronounced in the sidebands near integer multiples of the switching frequency.

operation, the axes of the stator and rotor windings need to be aligned by specifying the initial rotor position. The stator voltage supplied to the finite element model is assumed to be sinusoidal, the PWM rotor voltage is controlled by a scheme given in Fig. 7.3. The PI control system modeled is a simplified version of practical implementations, in which the reference value for the rotor current $I_{r,\mathrm{ref}}$ is calculated using the measured output power. In the present studies, the rotor current reference is predicted analytically. The analytical program is based on the equivalent circuit theory of induction machines and considers saturation effects, too [203]. The parameters for PI controller are obtained by analyzing the step response of the analytical machine model. Owing to the control system involved, startup transients need to be passed through before reaching the steady state.

7.2 Effects of inverter supply

The iron loss increase under inverter supply is evaluated by feeding the 2-D field solution to the iron loss models developed in the previous chapters. The 3-D eddy current model is solved in time domain using the $\boldsymbol{A}$,V formulation. The Preisach hysteresis model is identified from measurements presented in chapter 5 and employs again an isotropic input projection during vectorization.

All simulations have been carried out for both sinusoidal and PWM supply types. The computations under stator fed operation have been performed for no load and rated load conditions, by specifying the slip with $s = 0\,\%$ and $s = +0.91\,\%$, respectively. In doubly

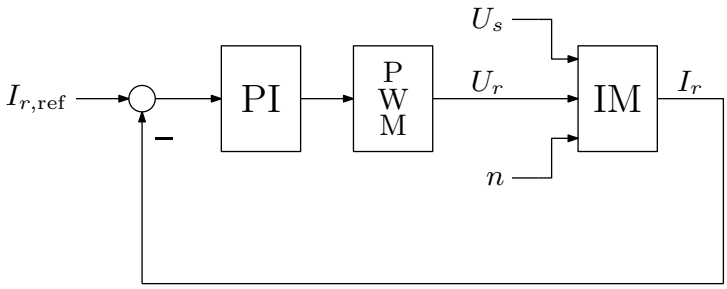

Fig. 7.3: Block diagram of the rotor current controller. The induction machine (IM) model takes the sinusoidal stator voltage U_s, the PWM rotor voltage U_r and the constant turbine speed n as inputs, and feeds back the rotor current I_r.

fed operation it is assumed that the turbine runs at 1700 rpm ($s = -13.3\,\%$) and that the plant delivers rated power with a power factor of $\cos\varphi = 1$ to the grid. About 10 % of the total output power as well as the overall reactive power required are carried over the frequency converter.

7.2.1 Eddy current losses

The loss distributions computed by the eddy current analysis are shown in Figs. 7.4 and 7.5. The results for sinusoidal stator fed operation have been thoroughly discussed in the previous chapters and are given here too, for the sake of completeness. The losses in doubly fed operation show a distribution similar to the loaded stator fed ones due to similar current loads in both cases.

Under stator fed inverter supply, the eddy current losses increase considerably for both loading conditions. The high harmonics present in the PWM supply voltage induce high frequency currents in the stator and rotor windings which lead to additional losses in the tooth area. The loss distribution increases almost equally for both loading types, since they are fed by the same PWM voltage. Slight differences can be observed on the rotor surface, because some tooth tip regions become highly saturated under load, presenting an unattractive path for the high-order inverter fields.

In doubly fed operation, the PWM-induced loss increase is significantly smaller than in the stator fed mode. This is due to the fact that the number of windings in the rotor is less than half of that in the stator. Harmonic voltage supplied to the rotor thus results in lower harmonic fields than if fed to the stator, even though the low rms value of the rotor voltage entails a smaller modulation index usually characterized by higher harmonic content [125].

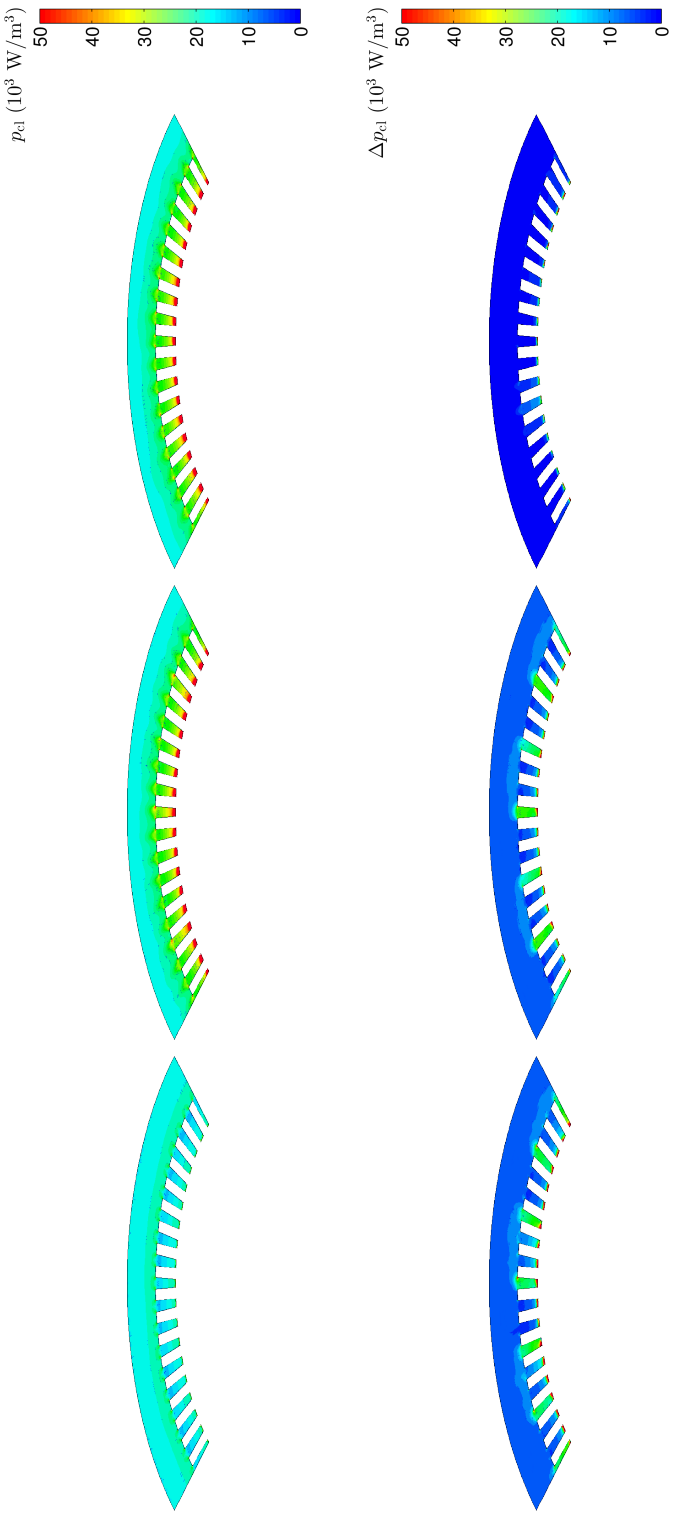

(a) stator fed, no load (b) stator fed, rated load (c) doubly fed

Fig. 7.4: Time-averaged eddy current loss distribution in the stator sheet under sinusoidal supply (above) and their increase under PWM supply ($p_{\mathrm{PWM}} - p_{\mathrm{sin}}$, below) for different operational conditions.

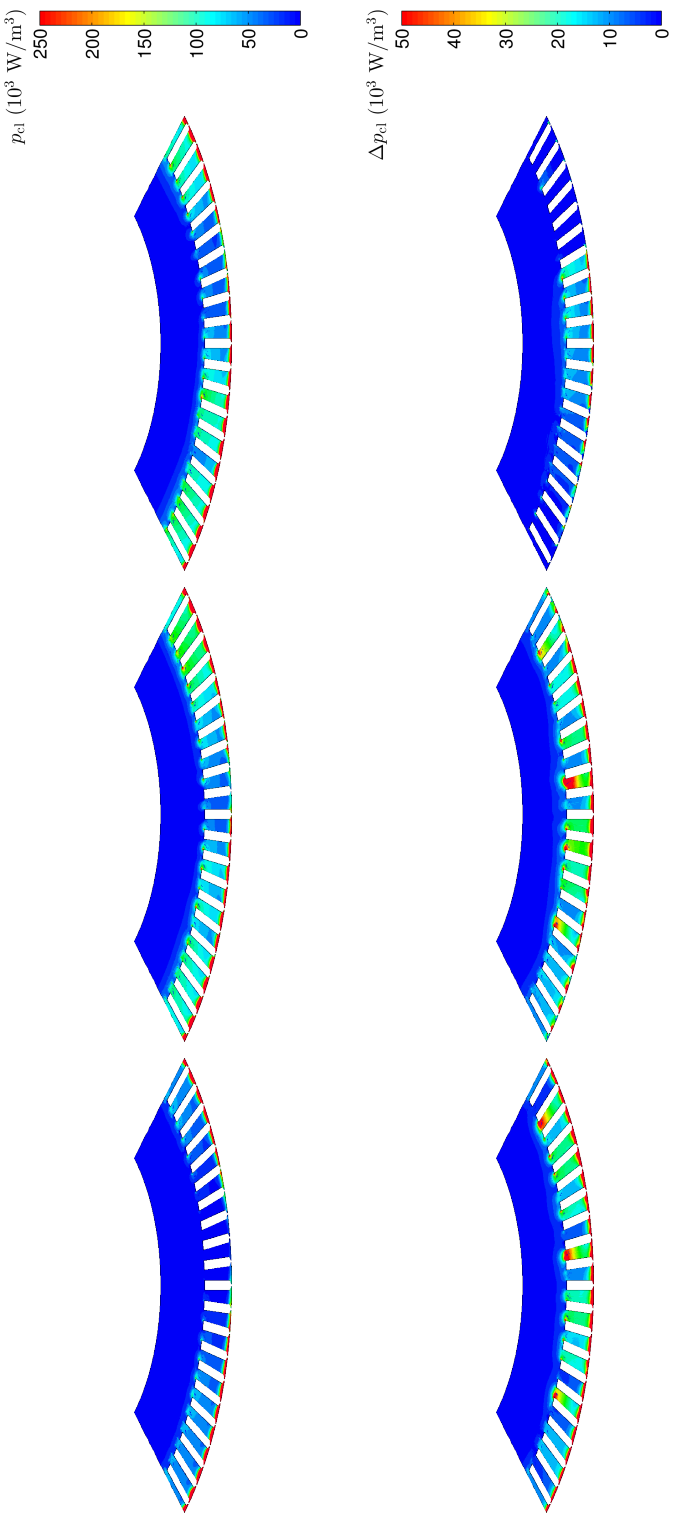

(a) stator fed, no load (b) stator fed, rated load (c) doubly fed

Fig. 7.5: Time-averaged eddy current loss distribution in the rotor sheet under sinusoidal supply (above) and their increase under PWM supply ($p_{\mathrm{PWM}} - p_{\mathrm{sin}}$, below) for different operational conditions.

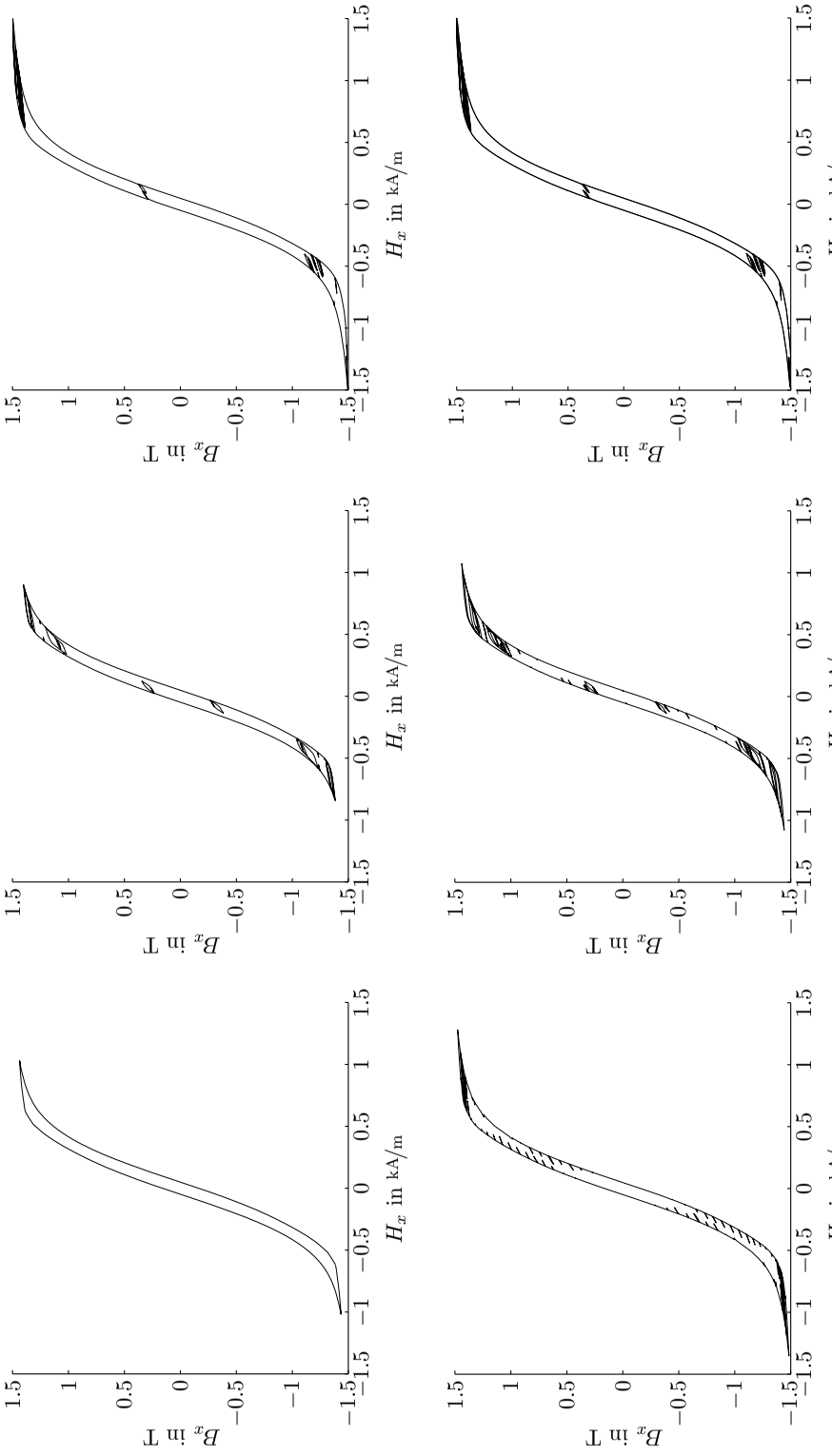

(a) stator fed, no load (b) stator fed, rated load (c) doubly fed

Fig. 7.6: Static hysteresis loops observed in the center of a stator tooth under sinusoidal supply (above) and under PWM supply (below) for different operating modes.

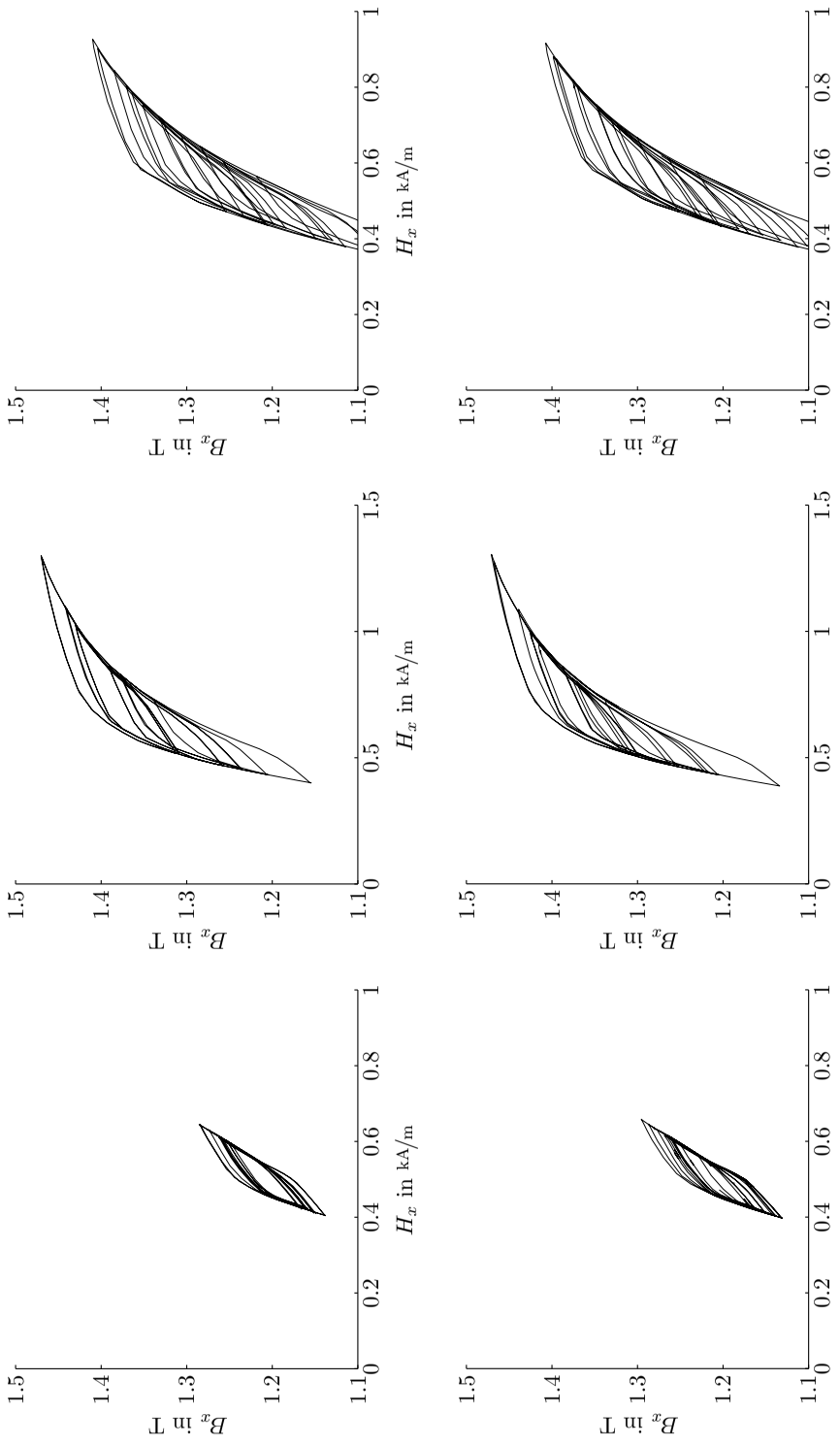

(a) stator fed, no load (b) stator fed, rated load (c) doubly fed

Fig. 7.7: Static hysteresis loops observed in the center of a rotor tooth under sinusoidal supply (above) and under PWM supply (below) for different operating modes.

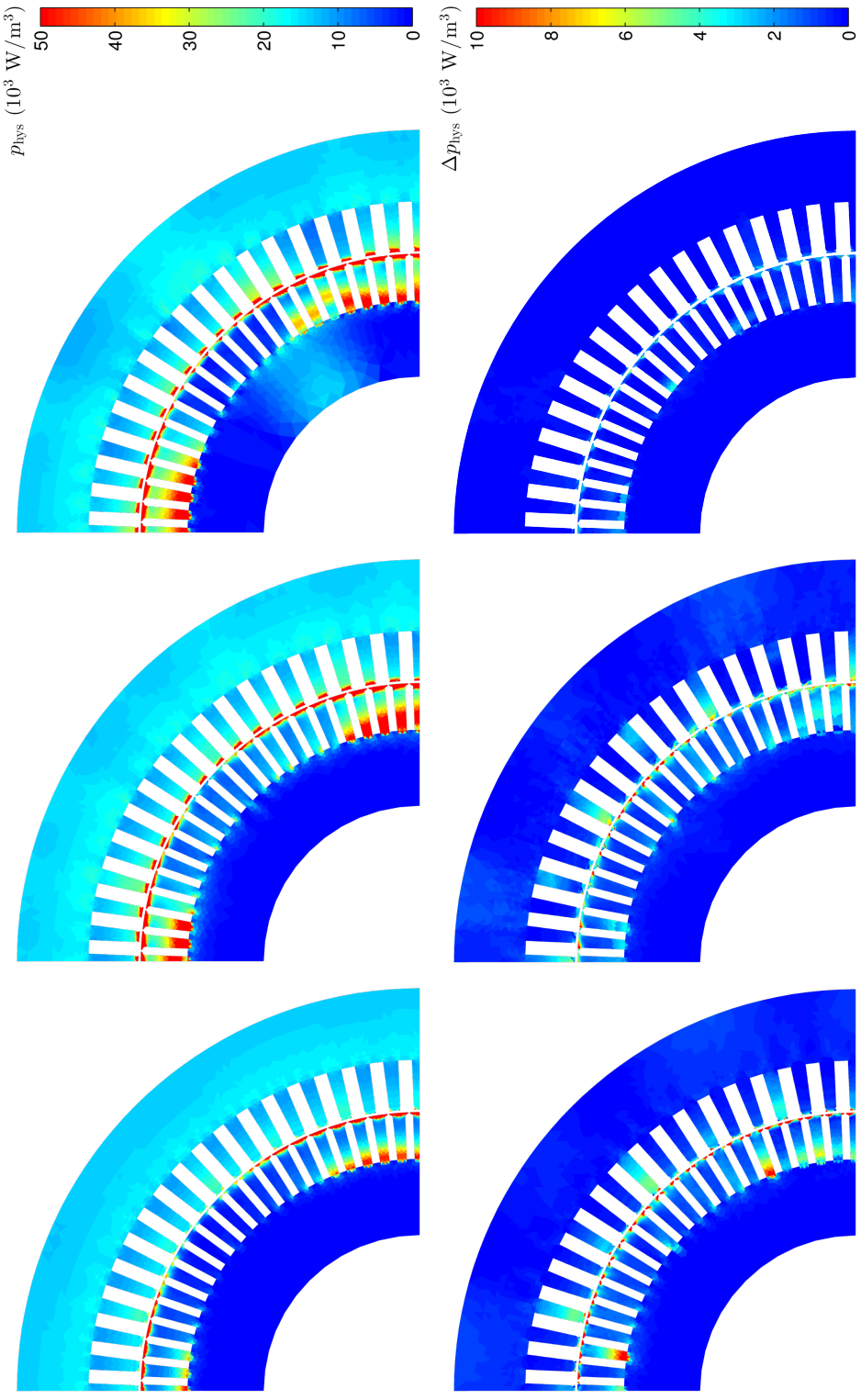

(a) stator fed, no load (b) stator fed, rated load (c) doubly fed

Fig. 7.8: Hysteresis losses under sinusoidal supply (above) and their increase under PWM supply ($p_{\mathrm{PWM}} - p_{\mathrm{sin}}$, below) for different operational conditions. The losses are calculated from the BH-loop area spanned over a complete period of the fundamental line frequency.

7.2.2 Hysteresis losses

Figs. 7.6 and 7.7 present the hysteresis loops in the middle of a tooth, obtained by postprocessing the 2-D field solution to the vector Preisach model. On the one hand, the PWM supply results in formation of new minor hysteresis loops as observed in the stator under no load condition. On the other hand, inverter feeding entails an enlargement of existing minor loops originating from slotting effects. The latter effect can be examined especially well in the rotor core, due to the exclusive presence of minor loops.

Under sinusoidal conditions, the hysteresis losses in Fig. 7.8 exhibit a similar distribution as the eddy current losses. A major part of the losses is evoked by the fundamental frequency component and most prominent in the stator sheet. The high frequency losses are again concentrated in the teeth and their tips and increase with the load applied. The additional hysteresis losses under PWM supply are considerably smaller than the eddy current ones. The loss increment is most pronounced in low saturated rotor tooth tips, whereas the stator losses do only marginally increase since the newly created minor loops span a relatively small BH-loop area.

7.2.3 Total iron losses

Table 7.1 quantifies the different iron loss components for each operating mode investigated. The given excess losses are again obtained from the hybrid model described in section 3.3.4. Under stator fed operation, the additional losses induced by the frequency converter are significant in both no load and rated load conditions. In percentage terms, the loss increase is more apparent under no load because of the inherently lower sinusoidal losses. The eddy current losses are observed to be most affected by the harmonics of the PWM supply, whereas the additional minor hysteresis loops result in a comparatively small loss increment. Moreover, it should be noted that particularly the rotor core is exposed to a severe loss increase, an important information for cooling design optimizations.

The studied doubly fed operation mode shows similar sinusoidal losses as the stator fed mode running under motor load, owing to similar loss distributions in both cases. The extra losses due to inverter supply exhibit the same tendencies as discussed above, but are in general much lower than the stator fed ones. This behavior is explained by the different winding topologies of stator and rotor resulting in different conversion of the voltage harmonics. Speaking in terms of equivalent circuit parameters, this implies that the machine represents a higher filter inductance for harmonics supplied to the rotor. Regarding wind power applications, the reduced additional losses in doubly fed configurations can be considered as a further advantage when competing against other topologies available.

Table 7.1: Iron losses under sinusoidal supply and their increase under PWM supply

(a) stator losses

operation mode	stator fed				doubly fed	
	no load		rated load			
supply type	sinus	PWM	sinus	PWM	sinus	PWM
P_{cl} (kW)	0.93	+26.1 %	1.46	+19.3 %	1.47	+4.51 %
P_{hys} (kW)	2.81	+4.32 %	3.26	+3.75 %	3.18	+0.48 %
P_{ex} (kW)	0.18	+26.4 %	0.24	+18.1 %	0.24	+1.04 %
P_{tot} (kW)	3.92	+10.5 %	4.96	+9.03 %	4.89	+1.71 %

(b) rotor losses

operation mode	stator fed				doubly fed	
	no load		rated load			
supply type	sinus	PWM	sinus	PWM	sinus	PWM
P_{cl} (kW)	0.83	+25.6 %	1.38	+16.7 %	1.48	+7.49 %
P_{hys} (kW)	0.58	+20.8 %	1.27	+8.39 %	1.67	+1.97 %
P_{ex} (kW)	0.13	+25.9 %	0.20	+13.9 %	0.21	+4.66 %
P_{tot} (kW)	1.54	+23.8 %	2.85	+12.9 %	3.36	+4.57 %

(c) stator + rotor losses

operation mode	stator fed				doubly fed	
	no load		rated load			
supply type	sinus	PWM	sinus	PWM	sinus	PWM
P_{tot} (kW)	5.45	+14.2 %	7.81	+10.4 %	8.25	+2.88 %

8 Additional losses due to interlaminar short circuits

Besides additional losses arising under practical working conditions, such as loaded operation or inverter supply, the manufacturing process itself can lead to a deteriorated loss behavior of the electrical steel sheets used. The ensuing loss increase is in general rather difficult to assess, since different manufacturing steps like rolling, cutting or assembling affect the electromagnetic steel properties in a stochastic way. An acknowledged issue during all stages of production is the formation of interlaminar short circuits between the stacked sheets possibly resulting in a significant loss increase and triggering local overheating. As outlined in the literature review of chapter 2, interlaminar short circuits are most likely caused by shearing burrs on the cutting edges as well as conductive joints mounted uninsulated on the iron stack. Further galvanic contacts can emerge from age-related insulation faults inside the core, but these are not treated here in detail.

Within the context of manufacturing influences, this chapter aims to contribute towards a better understanding of the effects of interlaminar short circuits. For this purpose, a novel interlaminar contact model will be set up by introducing appropriate boundary conditions on the 3-D eddy current model of a single sheet. Such an approach avoids full 3-D models with multiple short circuited laminations which become quickly cumbersome when more complicated geometries are dealt with. The interlaminar model has been presented in the conference publications [P10] and [P11], in which the method proposed has been first validated against full models with several joined sheets, and then applied to quantify the additional losses due to shearing burrs and conductive joints.

The following investigations employ time-harmonic analyses and are limited to the stator core operated under no load conditions. Previous results showed that, for no load, the losses in the stator sheets are almost exclusively caused by the fundamental field component. Therefore, they can be even evaluated correctly using harmonic simulations considering the fundamental component only. For rated no load current, the eddy current losses obtained from the transient analysis are 901 W, while the time-harmonic simulation yields 904 W. Despite the simplifications made, all relevant factors influencing the behavior underlying an interlaminar short circuit are still incorporated in the computations. The use of harmonic analyses constitutes no restriction on the introduced method, it remains easily expandable to transient simulations.

8.1 Interlaminar eddy current model

The developed 3-D eddy current model is extended to take account of the effects of interlaminar short circuits by specifying additional boundary conditions on the galvanic contact surfaces. Again, only a single sheet is considered in the 3-D model. This reduced approach is valid as far as, for multiple interconnected laminates, the electromagnetic quantities in the sheets within the core become periodic.

Fig. 8.1 illustrates the specifications of the boundary conditions for the 3-D model when the $\boldsymbol{A}, V$ formulation is used for the eddy current analysis. On the insulated surfaces, the boundary conditions of chapter 4 apply, ensuring that the normal component of the current density is zero here. On the interlaminar contact surface Γ_c, the current flow is

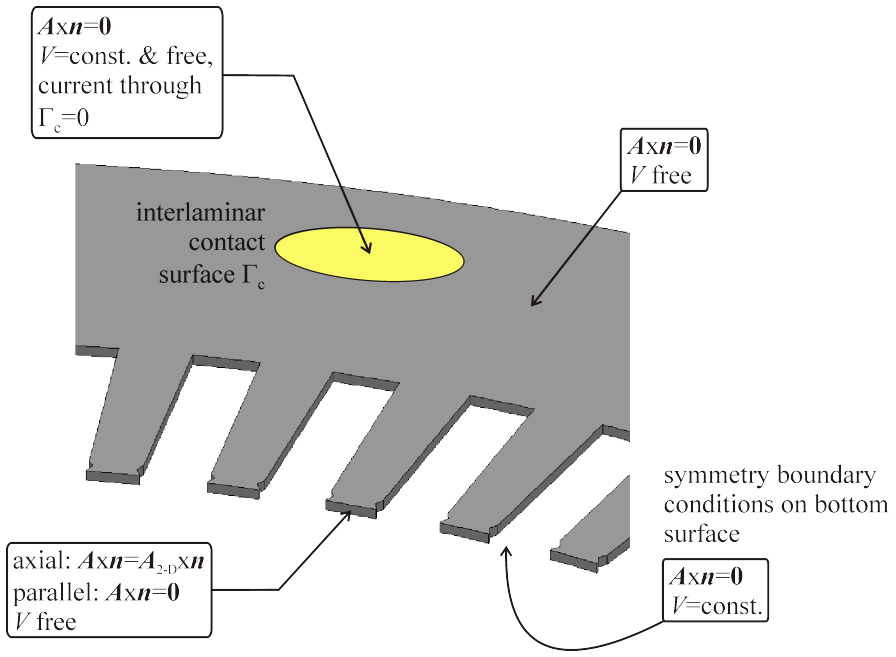

Fig. 8.1: Introduction of interlaminar boundary conditions on the stator sheet model. Note that Γ_c does not necessarily needs to be simply connected. The sheet thickness is increased for better visibility.

assumed to be normal to the face, resulting in a constant but unknown electric scalar potential. Moreover, it has to be guaranteed that the current exchanged through the contact spots between the laminations is zero by reformulating (3.35) as

$$\int_{\Gamma_\mathrm{c}} \sigma \left(\mathrm{j}\omega \boldsymbol{A} + \mathrm{j}\omega \nabla V\right) \cdot \boldsymbol{n} \, \mathrm{d}\Gamma = 0. \tag{8.1}$$

The unknown scalar potential is determined by introducing (8.1) as an additional equation into the finite element equations system [167].

For short circuits occurring on the sheet edges like shearing burrs, the effects of the high circulating eddy currents on the given magnetic boundary field cannot be neglected. In such cases, the magnetic vector potential is not prescribed directly on the axial boundaries, but on an additional outer finite element layer surrounding the lamination. This layer is modeled as non-conductive extending the 3-D problem to an $\boldsymbol{A}$,V-$\boldsymbol{A}$ one. Thus, the required independence of the impressed field from the eddy currents is ensured again.

8.2 Validation of the interlaminar model

The proposed interlaminar contact model is validated by means of two different examples: a simple conductive ring and a stator sheet sector of the induction machine investigated. Following the two step approach of chapter 4, the 3-D models are excited by boundary conditions obtained from a preceding 2-D analysis. Linear media are assumed for validation purposes, magnetic non-linearity is taken into account in section 8.3 based on an effective reluctivity method.

8.2.1 Conductive ring

As sketched in Fig. 8.2(a), the 2-D model of the ring is excited by a conductor arranged symmetrically in the bore and separated by an air-gap. The 3-D model (see Fig. 8.2(b)) consists of ten and a half stacked lamination quarters which are short circuited by two conductive joints through the entire core stack. The joint material is the same as that

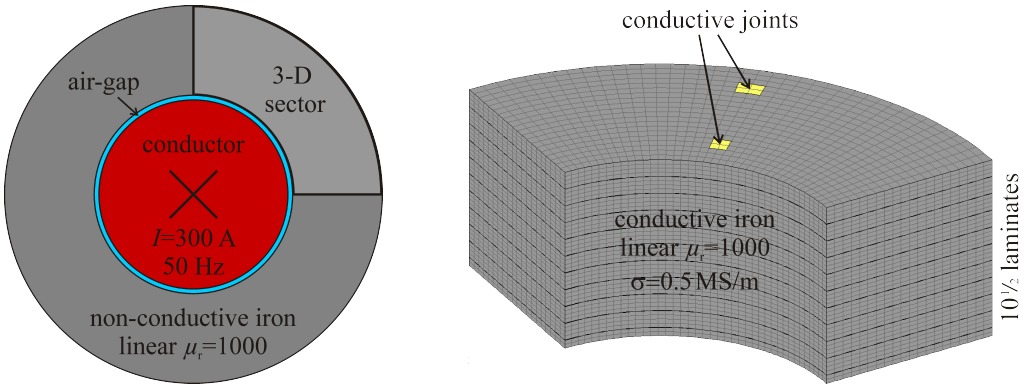

(a) 2-D model (b) 3-D model

Fig. 8.2: Validation geometries of the conductive ring.

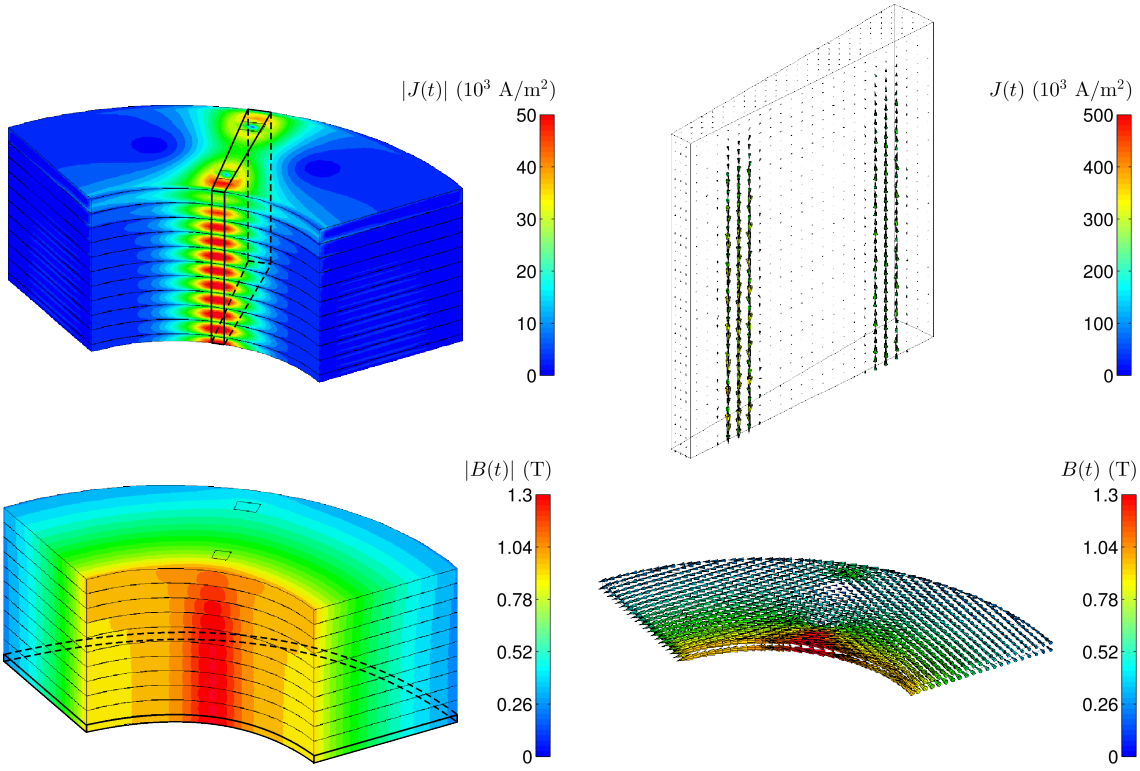

(a) full model (b) sector detail

Fig. 8.3: Current density (above) and flux density (below) at a specific time instant for the full model as well as the corresponding vector plots for the framed sectors.

of the laminates. The insulation between the sheets is modeled as a non-conductive $\boldsymbol{A}$-region having a relative permeability of one and a thickness of one hundredth of that of the laminations. The 2-D field solution is prescribed on the curved boundaries of the 3-D model, and periodic boundary conditions are applied on its left and right hand side. On the top surface, the normal component of $\boldsymbol{B}$ as well as that of $\boldsymbol{J}$ is set to zero; on the bottom surface, the problem is mirrored using symmetric boundary conditions. The 2-D problem is treated with the time-harmonic $\boldsymbol{A}$ formulation, the 3-D one with the $\boldsymbol{A}$,V-$\boldsymbol{A}$ formulation.

The electromagnetic quantities in Fig. 8.3 repeat periodically in the center sheets, suggesting the applicability of the reduced approach. The currents circulating through the contact spots affect the original 2-D field distribution and lead to an increased flux density near the ring edges. The undermost lamination of the full model serves as a validation reference for the proposed single sheet model. The field solutions of both models are com-

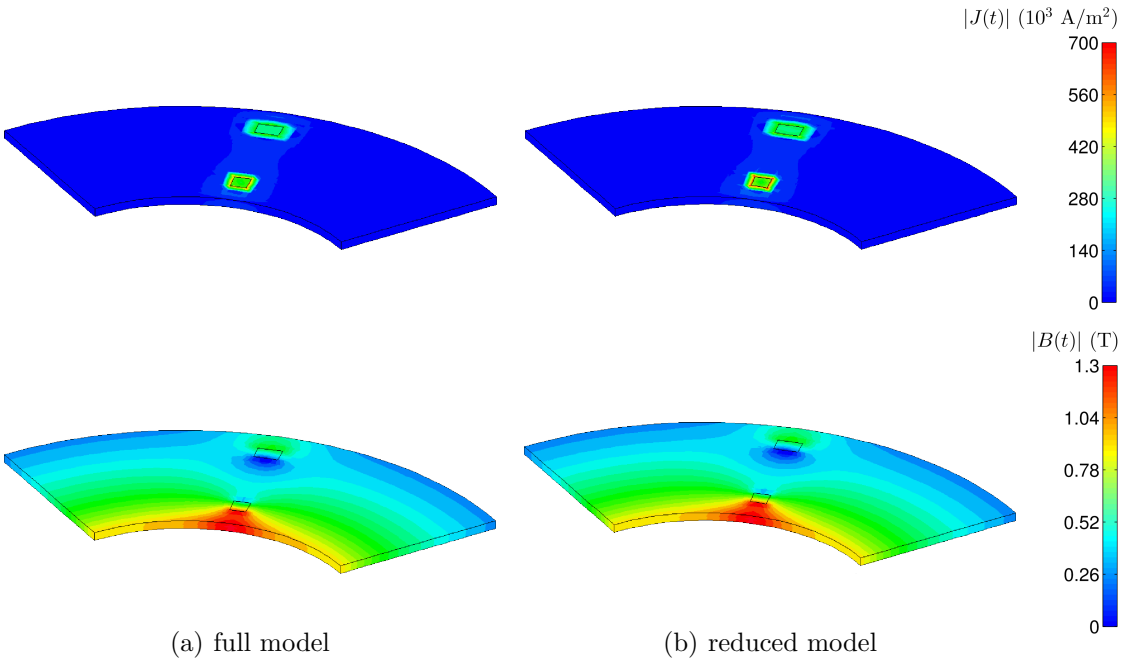

(a) full model (b) reduced model

Fig. 8.4: Current density (above) and flux density (below) distribution computed for the bottom lamination of the full model and for the reduced model proposed.

pared in Fig. 8.4. Their good agreement is also confirmed in terms of losses which are 10.9 mW for the full model and 11.4 mW for the reduced one.

8.2.2 Stator sheet sector

Since 3-D simulations with multiple short circuited stator laminations are hardly feasible, only a small sheet sector is considered in the full model. Fig. 8.5(a) highlights the studied sector, which is extruded in Fig. 8.5(b) to a 3-D model of hundred and a half laminates interconnected by shearing burrs over two teeth. A continuous burr width of 100 μm has been modeled requiring a rather fine mesh near the contact region. Results for different burr widths will be presented in section 8.3.2. Again, the properties of the burr material are assumed to be the same as those of the sheets. The 2-D vector potential is impressed on an outer non-conductive layer enclosing the teeth and on the stator back. The normal component of both $\boldsymbol{B}$ and $\boldsymbol{J}$ is zero on the top surface and on the boundaries intersecting the yoke.

The eddy current distribution computed by the full model is shown in Fig. 8.6, indicating high currents in the burred region which are closing over the teeth (see also Fig. 8.9). The induced currents increase with the number of short circuited laminations and asymptotically approach a final value. Accordingly, the reduced model presents a worst case

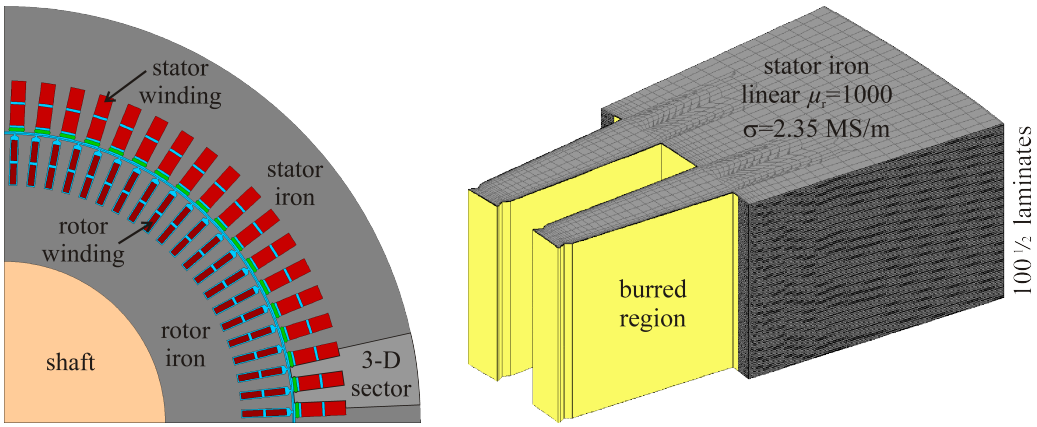

(a) 2-D model (b) 3-D model

Fig. 8.5: Validation geometries of the stator sheet sector.

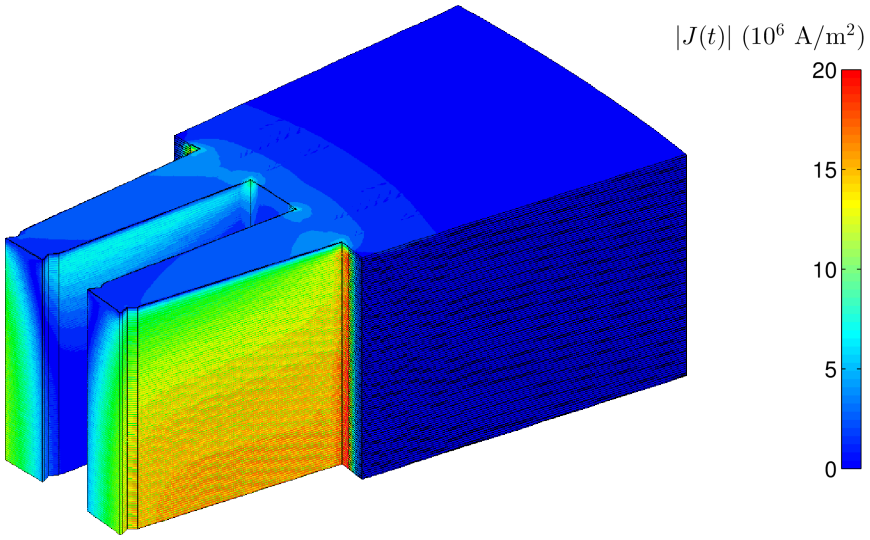

Fig. 8.6: Current density distribution for no load at a specific time instant for the full model.

scenario for a suitably large amount of interconnected sheets. The number of sheets required depends on various factors, such as the short circuit's geometry, sheet dimensions or material properties. The computed losses in the undermost lamination of the full model are 364 mW, the reduced method predicts 392 mW. The full model gives slightly lower loss values due to the limited number of laminations connected.

8.3 Effects of interlaminar short circuits

Two types of short circuits are discussed in more detail. The first one involves conductive joints introduced by clamping bars. Second, the effects of shearing burrs are subjected to a parametric study. All of the analyses below have been performed by using the proposed interlaminar contact model taking into account magnetic non-linearities.

8.3.1 Conductive joints

The iron stacks of mid-power range machines are commonly fixed by clamping bars installed after pressing the core. These clamping plates are mounted uninsulated on the core back representing a conductive connection among the sheets. Here, the ensuing loss increase for different numbers of bars attached along the stator back circumference is examined.

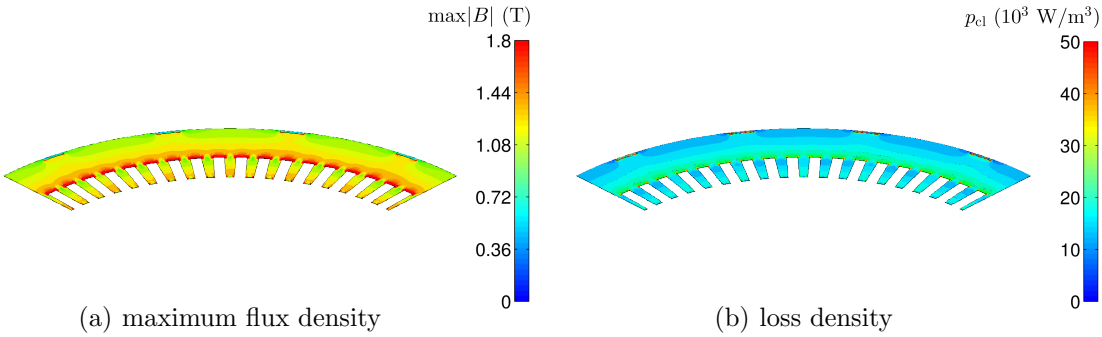

(a) maximum flux density (b) loss density

Fig. 8.7: Flux density and time-averaged loss density distribution in a stator sheet for four clamping bars per pole modeled.

The results for four clamping bars per pole pitch are shown in Fig. 8.7, and demonstrate that, on the one hand, the induced currents in axial direction cause additional losses. On the other hand, they oppose the original field increasing the magnetic flux density and hence the losses near the clamping areas. A detailed view of the electromagnetic quantities near a contact area is given in Fig. 8.8. The eddy current losses rise linearly with the number of bars, reaching from 3.93 % for one, to 13.7 % for four bars installed.

8.3.2 Shearing burrs

In order to quantify the extra losses due to edge burrs, simulations for various burr widths and different numbers of teeth afflicted have been carried out. Contrary to the former validation example, a complete stator sheet quarter has been considered in the computations.

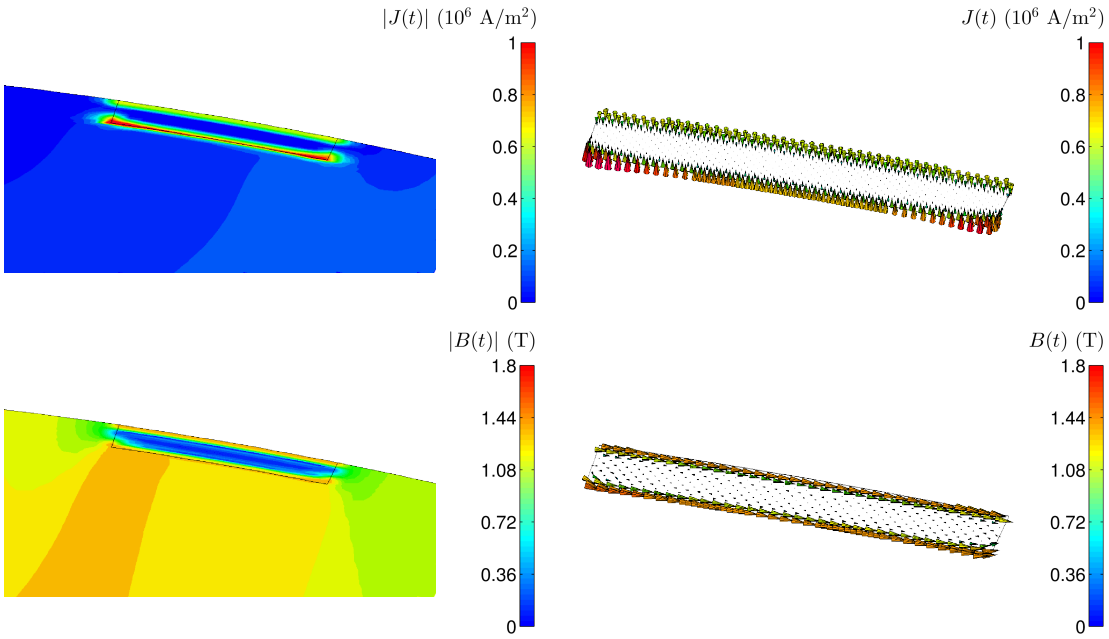

(a) field distribution (b) vector plot

Fig. 8.8: Current density (above) and flux density (below) in the contact spot area at a specific time instant.

Fig. 8.9 shows the eddy current paths in the contact layer for different faulty teeth. The high magnetizing flux in the tooth area induces interlaminar currents enclosing the teeth, leading to a steep loss increase. The trends in Fig. 8.10 exhibit a cubic dependence of the additional losses on the number of teeth burred. Applying burrs on the stator back has led to no significant loss increment owing to the weakened flux density near the outermost rim.

The burr width has been varied in a practically relevant range from 10 to 100 μm. Even broader galvanic contacts may be present in laser cut sheets due to the heat-induced insulation burn-off. As presented in Fig. 8.10, the losses rise linearly with the width of the burr layer, regardless of the amount of teeth afflicted.

One should note that the burrs modeled will not be present to such an extent in a healthy machine. The simulated configurations are worst case approximations giving maximum loss values indicating the strong necessity to minimize burr-induced short circuits as far as practicable. However, the basic trends and findings will still hold, even when the overall problem might be alleviated by its stochastic nature.

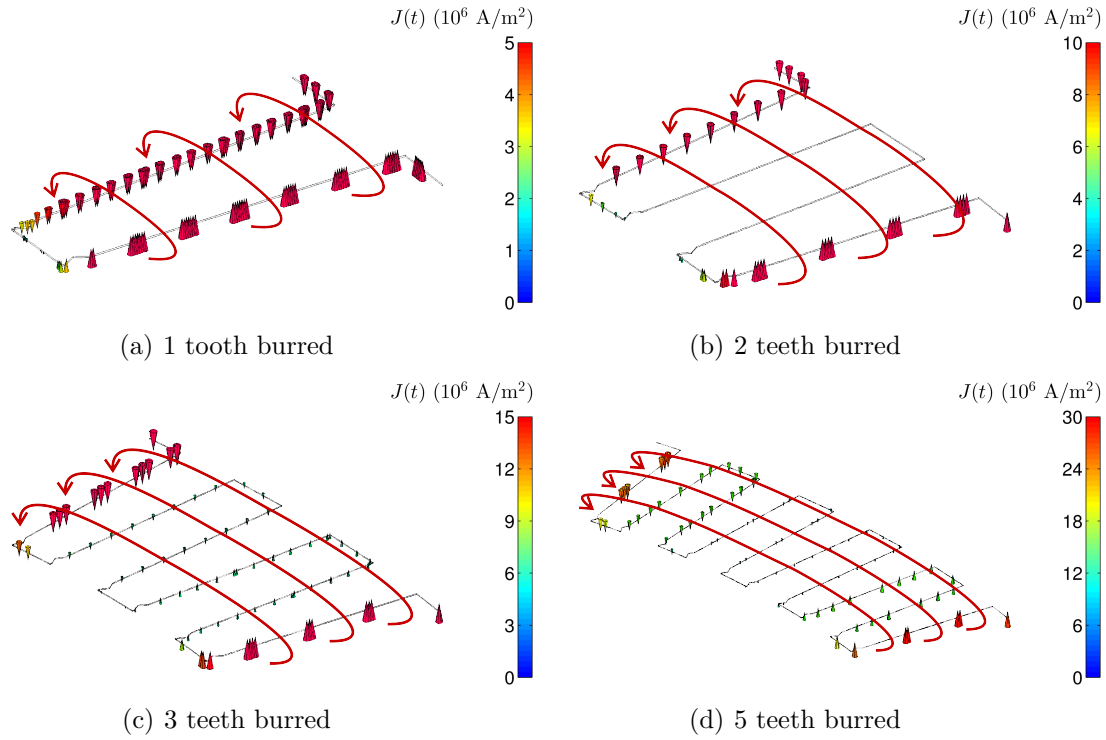

(a) 1 tooth burred (b) 2 teeth burred

(c) 3 teeth burred (d) 5 teeth burred

Fig. 8.9: Current density vector plots for different number of faulty teeth and a burr width of 100 μm. The burr region only is considered in the plot. Red arrows indicate the closing paths of the current loops.

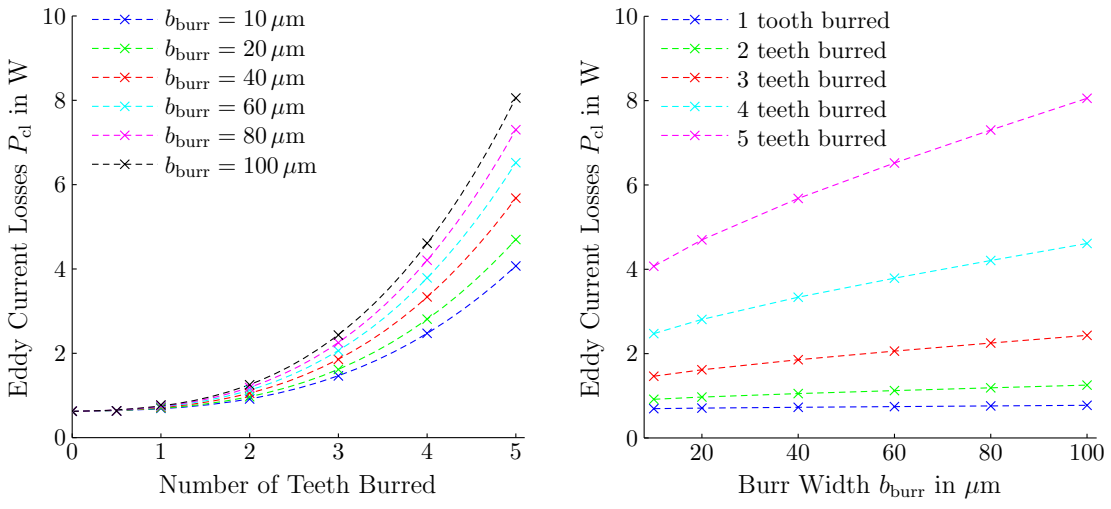

(a) variable teeth number (b) variable burr width

Fig. 8.10: Losses as a function of the number of burred teeth for different burr widths. The given values refer to a single sheet.

9 Discussions and Conclusions

This thesis contributes to an improved iron loss estimation in rotating electrical machines by developing and applying advanced eddy current and hysteresis loss models. This chapter summarizes the main findings obtained, including a discussion on their practical significance. Finally, some proposals for further work are given and the main conclusions are drawn.

9.1 Discussion of the methods and results

To ensure consistency with the previous structure, the following discussions are organized chapter-wise.

9.1.1 3-D eddy current model

The developed eddy current model overcomes some restrictions of the approaches known from literature by considering the true 3-D eddy current distribution in the steel sheets. This ensures correct modeling of the edge effects becoming important in the lamination's tooth tips exposed to high frequency fields. Using the method proposed, a classical 2-D field analysis is carried out first in order to generate a set of boundary conditions for the 3-D model. Then, the 3-D eddy current problem is solved separately for the stator and rotor sheets, thus allowing their parallel treatment avoiding computationally expensive transient 3-D simulations including rotor motion.

Combined with the Preisach hysteresis model, the 3-D eddy current model has been applied to the iron loss estimation of slip-ring induction machines, for which no load measurements were available. Good agreement is observed between the measured and computed values, confirming the validity of the methods presented. Some inevitable differences are caused by the deteriorated material characteristics resulting from manufacturing, and additional losses in inactive construction parts, some of which have also been addressed numerically.

Since measurements hardly enable the segregation of the different core loss components, the proposed eddy current model serves as a validation basis for two simplified loss models: the widely used traditional technique based on the statistical loss theory, and the hybrid model which evaluates the shapes of dynamic hysteresis loops. The identification procedure of the traditional model has shown that it is limited to low frequency applications.

The traditional model might be considerably improved by using modified approaches outlined in the literature review. However, the purpose of this work has been to study a broadly applied and rather simple model requiring a minimum set of parameters. As a representative example of a more advanced technique, the hybrid model gives quite accurate results up to high frequencies and flux densities, and has been found to be a good compromise between computational burden, accuracy and universality.

9.1.2 Anisotropic vector Preisach model

Using a generalized input projection in the vector model enables an efficient treatment of anisotropic material properties by keeping all essential features of the original Preisach model. The generalization presented further improves the rotational loss characteristics at saturation by correcting the phase lag between the $\boldsymbol{B}$ and $\boldsymbol{H}$ vectors. In combination with the hybrid approach for the eddy current and excess effects, the model is able to cope with alternating and rotating flux conditions even for frequencies up to the kilohertz range.

Although studies on how the anisotropy affects the machine's iron losses are still pending, the effects of the rotational loss behavior have been subjected to a detailed analysis. It has been shown that the rotational losses are notably decreasing when using the proposed phase lag correction. However, their reduction contributes to a minor decrease of the overall hysteresis losses, owing to the limited presence of purely rotational fields.

9.1.3 Effects of loading and skewing

The high harmonic content present in the machine cores leads to elevated iron losses, which significantly increase when load is getting applied. The effects of loading have been investigated along with the development of a harmonic decomposition method to efficiently bypass the numerical effort of the original transient eddy current analysis. The harmonic method requires a fractional amount of computation time and gives reliable results under any loading state. Besides its parallelization capabilities, the approach introduced has the further advantage of providing the steady state solution instantaneously without the need to step through starting transients. The time-harmonic problems are solved fastest with the $\boldsymbol{A}$,$\boldsymbol{T}$ instead of the commonly used $\boldsymbol{A}$,V formulation, because the former one allows an explicit satisfaction of the boundary conditions for the current density.

The effects of skewing have been evaluated by applying the iron loss models to a multi-slice solution. The simulation results under load show that skewing leads to a highly non-uniform core loss distribution along the machine length. Even though the overall losses are only marginally influenced by the skew, their axial redistribution can lead to localized overheating which should be remedied by suitable cooling measures.

In the conventional machine design, the additional losses due to loading are usually considered by stray load factors, or even ignored completely. The investigations in this thesis have stressed the crucial importance of correctly modeling the high frequency effects under load. Factors making the conventional approaches inappropriate are complicated machine geometries combined with magnetic non-linear material properties. For instance, it has been observed that particularly the magnetic characteristics of the slot wedges in the stator have a strong influence on the high frequency rotor losses, thus requiring proper measurement and modeling of the wedge material.

9.1.4 Effects of inverter supply

The high frequency effects become even more aggravated when the machine windings are externally supplied by a frequency converter. The additional losses arising have been calculated by coupling a PWM fed machine model to the eddy current and hysteresis loss models presented. Different inverter fed operating modes have been examined by comparing them to sinusoidal supply conditions.

During inverter feeding on the stator side, the iron losses increase by up to about 15 %, whereby the eddy current component is identified to be most affected. Compared to previous work known from literature, the iron losses in doubly fed operation in general, and under inverter supply in particular, have been addressed for the first time. Interestingly, the rotor-sided inverter supply has led to relatively low extra losses, since the different turns ratio of the rotor winding attenuates the harmonic field content induced.

9.1.5 Effects of interlaminar short circuits

Extending the 3-D eddy current model proposed, the effects of interlaminar short circuits have been taken into account by suitable boundary conditions on the contact surface. The reduced single sheet approach avoids full 3-D models of many short-circuited laminations by still considering their geometrically complex structure.

Comparisons of the interlaminar contact model against full models have confirmed the validity of the reduced method as long as the electromagnetic quantities in the short-circuited sheets stay periodic. For a low number of interconnected laminations, the full model yields lower losses than the reduced one. Consequently, the reduced model constitutes a worst case approximation used in practice for the quantification of loss limits.

Applications have revealed a significant loss increase for conductive paths introduced by shearing burrs on the tooth edges. Furthermore, additional losses due to conductive fixing joints have also been detailed, whose effects are usually acknowledged in the industrial praxis, but rarely quantified by numerical means.

9.2 Suggestions for future research

In this thesis, the 3-D eddy current model has been compared to two simplified loss models which represent various methods known from literature. For a more comprehensive assessment of the 3-D effects, comparisons to other advanced approaches, like 1-D lamination models, have to be carried out in future. Moreover, the 3-D model offers high extension capabilities to account for axial fields caused by air-gap fringing and the end winding leakage. To consider their effects, the initial 2-D analysis needs to be replaced by a 3-D laminar continuum model having anisotropic material properties. The eddy currents within each laminate will then be computed by exciting the individual sheet models with both axial and parallel field components.

As already mentioned, applications of the proposed anisotropic vector Preisach model are still missing, making them an attractive topic for subsequent research. When employing the model in postprocessing stage, anisotropic behavior must be considered in the BH-characteristics of the 2-D analysis. Their incorporation is most efficiently achieved by energy/coenergy concepts, such as used in the elliptic model of [99]. In order to sustain the general validity of the anisotropic hysteresis model, further measurements including two other steel grades have been performed, which remain to be identified in future.

The harmonic decomposition method has been developed for sinusoidal supply conditions. Extensions to inverter supply require consideration of the additional harmonics introduced when deriving the boundary conditions for the individual harmonic 3-D problems. The evaluation of skewing effects could be improved by adopting the approach of [204] which analytically reconstructs the field variation along the machine length based on a multi-slice solution. Thus, a finer resolution of the axial loss distribution could be obtained, instead of using the slice solutions only.

The investigations in chapter 7 were limited to a single inverter topology providing the same PWM pattern. In future, the analysis could be expanded to other inverter characteristics comprising different modulation techniques and switching frequencies. These studies will enable establishing an optimization basis for the whole drive system, taking into account additional machine losses as well as switching losses emerging in the frequency converter.

Regarding the effects of interlaminar short circuits, the method introduced needs to be combined with statistical approaches before incorporating them into practical design tools. In particular, the formation of burrs is of highly stochastic nature and has to be identified from a series of measurements. Lately, the deterioration of the steel properties as a result of various manufacturing influences, most importantly the permeability drop due to mechanical stress, have aroused the interest of many researchers [141–144] whose proposals could also be integrated in the methods presented here.

9.3 Conclusion

To conclude, this thesis has tackled some of the main problems encountered during the development of accurate design tools for the prediction of iron losses in rotating electrical machines. Such problems embrace the occurrence of distorted field patterns in a basically 3-D structure, complicated ferromagnetic properties at a microscopic scale, and the lack of reliable measurement data. Traditionally, the complex phenomena arising are treated by simplified analytical or empirical approaches, which do neither allow exact quantification nor segregation of the loss components.

The advanced methods proposed distinguish themselves from pervious approaches by establishing novel numerical procedures founded on a physical or phenomenological basis. The presented eddy current model considers the 3-D field distribution in the individual laminates, thus offering high accuracy but also computational efficiency when realized by the harmonic decomposition approach. The extensions of the vector Preisach model have helped to improve the predictions of hysteresis effects under magnetically anisotropic conditions as well as rotational fields. Combining the two models has proven to correctly reproduce measurement results for the complex field patterns emerging in induction machines.

Applications have addressed various types of additional losses arising under practical working conditions. Under loaded operation and inverter supply, the harmonic field content, and hence the iron losses, increase significantly, emphasising the strong necessity to accurately consider high frequency effects in the models. Within the context of manufacturing influences, the 3-D eddy current model has been extended to the effects of interlaminar short circuits, providing initial studies for a systematical assessment of a relatively unexplored field.

A Machine and sheet data

The main parameters of the studied slip-ring induction machines are listed in Table A.1. Machine 1 has been examined in the main chapters, while some further results for machine 2 are given in appendix B. The same steel sheet type is used in both machines (see Table A.2).

Table A.1: Main parameters of the slip-ring induction machines studied

	machine 1	machine 2
rated power (MW)	1.75	1.75
rated frequency (Hz)	50	60
rated voltage (V)	690	575
rated slip	0.91 %	0.72 %
power factor	0.92	0.90
number of poles	4	6
number of phases	3	3
winding connection stator	delta	star
winding connection rotor	star	star
skewed	yes	yes

Table A.2: Main parameters of the electrical steel sheet used

grade	M400-50A
thickness (mm)	0.5
conductivity @ 20°C ($^{MS}/_{m}$)	2.35
mass density ($^{kg}/_{m^3}$)	7700

B Further simulation and measurement results

Here, additional results for the induction machine 2, detailed in Table A.1, are given. The presented investigations have been carried out for no load operation fed by rated voltage. In contrast to the no load simulations of chapter 4, the initial 2-D problem is voltage driven via an external electrical circuit. Regarding the computed iron losses, no significant differences have been observed when supplying the models with sinusoidal current, since the stator currents of the voltage fed model are characterized by rather low harmonic content [202].

The core losses are again evaluated by postprocessing the 2-D field solution by the methods presented. Fig. B.1 shows the computed 3-D eddy current density in the steel sheets, and Fig. B.2 the simulated hysteresis losses. Both distributions exhibit similar properties as observed for machine 1 whose results have been thoroughly discussed in the previous chapters. The core loss components are segregated in Table B.1 which includes results for machine 1 as well. Again, good agreement is achieved between measurements and simulations evidencing the validity of the proposed methods.

Table B.1: Separated iron losses for both machines

	machine 1		machine 2	
	stator	rotor	stator	rotor
P_{cl} (kW)	0.93	0.83	1.37	1.89
P_{hys} (kW)	2.81	0.58	3.45	1.59
P_{ex} (kW)	0.18	0.13	0.24	0.25
P_{tot} (kW)	5.45		8.80	
measured	5.50		8.37	

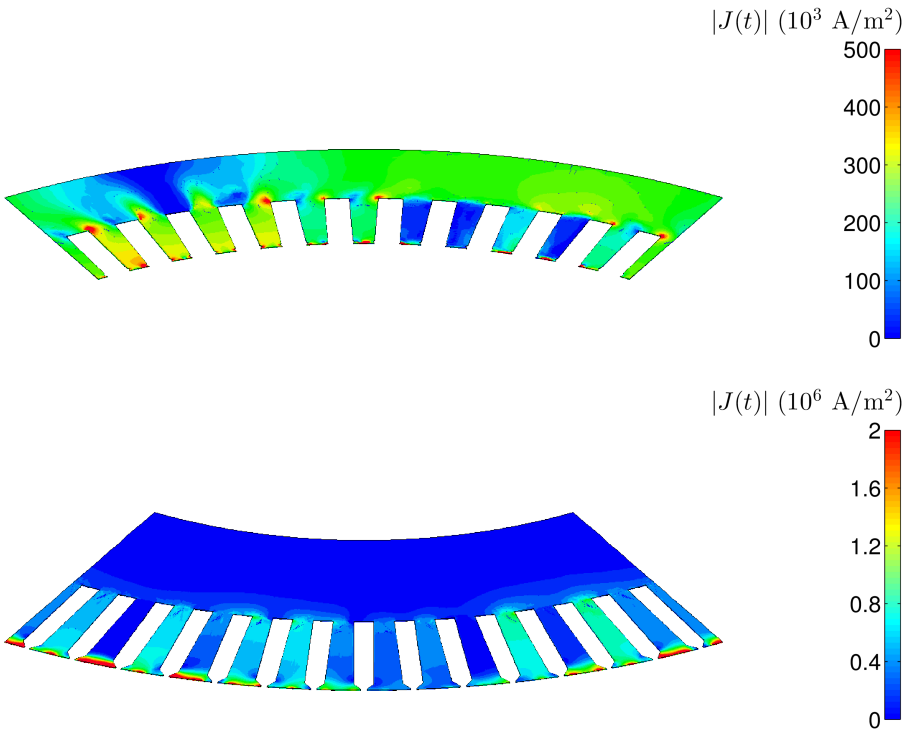

Fig. B.1: 3-D eddy current distribution at a specific time instant for the stator (above) and rotor (below) sheets of machine 2.

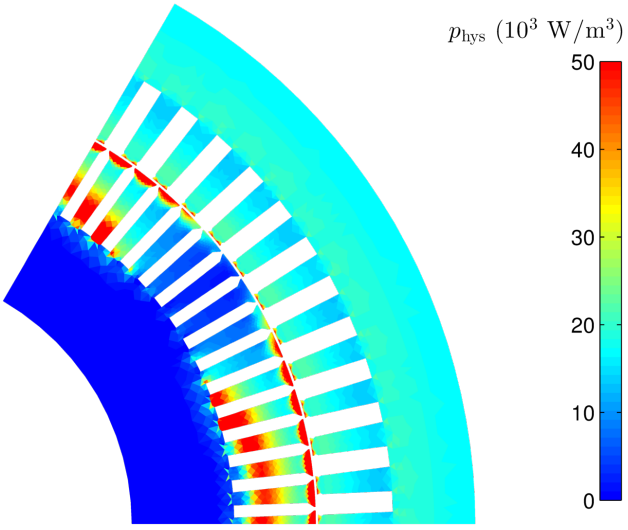

Fig. B.2: Hysteresis losses for machine 2 obtained from the isotropic vector Preisach model without phase lag correction.

C Bibliography

[1] P. Waide and C. U. Brunner, *Energy-Efficiency Policy Opportunities for Electric Motor-Driven Systems*, International Energy Agency, 2011.

[2] *IEC 60034-2-1 Rotating electrical machines. Part 2-1: Standard methods for determining losses and efficiency from tests (excluding machines for traction vehicles)*, International Electrotechnical Comission Std., 2007.

[3] *IEC 60034-2-2 Rotating electrical machines. Part 2-2: Specific methods for determining separate losses of large machines from tests - Supplement to IEC 60034-2-1*, International Electrotechnical Comission Std., 2010.

[4] *IEC 60034-2-3 Rotating electrical machines. Part 2-3: Specific test methods for determining losses and efficiency of converter-fed AC induction motors*, International Electrotechnical Comission Std., 2013.

[5] *IEC 60034-30 Rotating electrical machines. Part 30: Efficiency classes of single-speed, three-phase, cage-induction motors (IE-code)*, International Electrotechnical Comission Std., 2008.

[6] G. Bertotti, *Hysteresis in Magnetism*, Academic Press, 1998.

[7] C. P. Steinmetz, "On the law of hysteresis," *Transactions of the American Institute of Electrical Engineers*, vol. 9, pp. 3–64, 1892.

[8] J. Reinert, A. Brockmeyer, and R. D. Doncker, "Calculation of losses in ferro- and ferrimagnetic materials based on the modifed Steinmetz equation," *IEEE Transactions on Industry Applications*, vol. 37, no. 4, pp. 1055–1061, 2001.

[9] W. A. Roshen, "A Practical, Accurate and Very General Core Loss Model for Nonsinusoidal Waveforms," *IEEE Transactions on Power Electronics*, vol. 22, no. 1, pp. 30–40, 2007.

[10] J. Mühlethaler, J. Biela, J. Kolar, and A. Ecklebe, "Core Losses Under the DC Bias Condition Based on Steinmetz Parameters," *IEEE Transactions on Power Electronics*, vol. 27, no. 2, pp. 953–963, 2012.

[11] K. Venkatachalam, C. R. Sullivan, T. Abdallah, and H. Tacca, "Accurate prediction of ferrite core loss with nonsinusoidal waveforms using only Steinmetz parameters," in *Proceedings of the IEEE Workshop on Computers in Power Electronics*, 2002.

[12] H. Jordan, "Ferromagnetic constants for weak fields," *Elektrische Nachrichtentechnik*, pp. 7–29, 1924.

[13] J. D. Lavers, P. P. Biringer, and H. Hollitscher, "A Simple Method of Estimating the Minor Loop Hysteresis Loss in Thin Laminations," *IEEE Transactions on Magnetics*, vol. 14, no. 5, pp. 386–388, 1978.

[14] G. Bertotti, "General properties of power losses in soft ferromagnetic materials," *IEEE Transactions on Magnetics*, vol. 24, no. 1, pp. 621–630, 1988.

[15] J. Lammeraner and M. Štafl, *Eddy Currents*, Iliffe Books Ltd., 1966.

[16] F. Fiorillo and A. Novikov, "An Improved Approach to Power Losses in Magnetic Laminations under Nonsinusoidal Induction Waveform," *IEEE Transactions on Magnetics*, vol. 26, no. 5, pp. 2904–2910, 1990.

[17] A. Boglietti, A. Cavagnino, M. Lazzari, and M. Pastorelli, "Predicting Iron Losses in Soft Magnetic Materials With Arbitrary Voltage Supply: An Engineering Approach," *IEEE Transactions on Magnetics*, vol. 39, no. 2, pp. 981–989, 2003.

[18] E. Barbisio, F. Fiorillo, and C. Ragusa, "Predicting Loss in Magnetic Steels Under Arbitrary Induction Waveform and With Minor Hysteresis Loops," *IEEE Transactions on Magnetics*, vol. 40, no. 4, pp. 1810–1819, 2004.

[19] D. M. Ionel, M. Popescu, S. J. Dellinger, T. J. E. Miller, R. J. Heideman, and M. I. McGilp, "On the variation with flux and frequency of the core loss coefficients in electrical machines," *IEEE Transactions on Industry Applications*, vol. 42, no. 3, pp. 658–667, 2006.

[20] K. Atallah, Z. Q. Zhu, and D. Howe, "An improved method for predicting iron losses in brushless permanent magnet dc drives," *IEEE Transactions on Magnetics*, vol. 28, no. 5, pp. 2997–2999, 1992.

[21] B. Štumberger, V. Goričan, A. Štumberger, A. Hamler, M. Trlep, and M. Jesenik, "Accuracy of iron loss calculation in electrical machines by using different iron loss models," *Journal of Magnetism and Magnetic Materials*, vol. 254–255, pp. 269–271, 2003.

[22] K. Narita and T. Yamaguchi, "Rotational and Alternating Hysteresis Losses in 4% Silicon-Iron Single Crystal with the {110} Surface," *IEEE Transactions on Magnetics*, vol. 11, no. 6, pp. 1661–1666, 1975.

[23] A. Cecchetti, G. Ferrai, F. Masoli, and G. P. Soardo, "Rotational Power Losses in 3 % SiFe as a Function of Frequency," *IEEE Transactions on Energy Conversion*, vol. 14, no. 5, pp. 356–358, 1978.

[24] R. M. Bozorth, *Ferromagnetism*, Wiley-IEEE Press, 1993.

[25] G. Bertotti, A. Boglietti, M. Chiampi, D. Chiarabaglio, F. Fiorillo, and M. Lazzari, "An improved estimation of iron losses in rotating electrical machines," *IEEE Transactions on Magnetics*, vol. 27, no. 6, pp. 5007–5009, 1991.

[26] O. Bottauscio, M. Chiampi, A. Manzin, and M. Zucca, "Additional Losses in Induction Machines Under Synchronous No-Load Conditions," *IEEE Transactions on Magnetics*, vol. 40, no. 5, pp. 3254–3261, 2004.

[27] J. G. Zhu and V. S. Ramsden, "Improved Formulations for Rotational Core Losses in Rotating Electrical Machines," *IEEE Transactions on Magnetics*, vol. 34, no. 4, pp. 2234–2242, 1998.

[28] N. Soda and M. Enokizono, "Improvement of T-Joint Part Constructions in Three-Phase Transformer Cores by Using Direct Loss Analysis with E&S Model," *IEEE Transactions on Magnetics*, vol. 36, no. 4, pp. 1285–1288, 2000.

[29] A. Belahcen and A. Arkkio, "Comprehensive Dynamic Loss Model of Electrical Steel Applied to FE Simulation of Electrical Machines," *IEEE Transactions on Magnetics*, vol. 44, no. 6, pp. 886–889, 2008.

[30] V. C. Silva, G. Meunier, and A. Foggia, "A 3-D Finite-Element Computation of Eddy Currents and Losses in Laminated Iron Cores Allowing for Electric and Magnetic Anisotropy," *IEEE Transactions on Magnetics*, vol. 31, no. 3, pp. 2139–2141, 1995.

[31] A. G. Jack and B. C. Mecrow, "Calculation of three-dimensional electromagnetic fields involving laminar eddy currents," *IEE Proceedings Part A*, vol. 134, no. 8, pp. 663–671, 1987.

[32] B. C. Mecrow, A. G. Jack, and C. S. Cross, "Electromagnetic design of turbogenerator stator end regions," *IEEE Transactions on Energy Conversion*, vol. 136, no. 6, pp. 361–372, 1989.

[33] G. K. M. Khan, G. W. Buckley, R. B. Bennett, and N. Brooks, "An Integrated Approach for the Calculation of Losses and Temperatures in the End-region of Large Turbine Generators," *IEEE Transactions on Energy Conversion*, vol. 5, no. 1, pp. 183–194, 1990.

[34] V. C. Silva, G. Meunier, and A. Foggia, "A 3D Finite-Element Computation of Eddy Currents and Losses in the Stator End Laminations of Large Synchronous Machines," *IEEE Transactions on Magnetics*, vol. 32, no. 3, pp. 1569–1572, 1996.

[35] E. Schmidt, G. Traxler-Samek, and A. Schwery, "3D nonlinear transient finite element analysis of eddy currents in the stator clamping system of large hydro generators," *COMPEL: The International Journal for Computation and Mathematics in Electrical and Electronic Engineering*, vol. 25, no. 2, pp. 440–451, 2006.

[36] Y. Yao, H. Xia, G. Ni, X. Liang, and Z. Xian, "3-D Eddy Current Analysis in the End Region of a Turbogenerator by Using Reduced Magnetic Vector Potential," *IEEE Transactions on Magnetics*, vol. 42, no. 4, pp. 1323–1326, 2006.

[37] L. Weili, G. Chunwei, and Z. Ping, "Calculation of a Complex 3-D Model of a Turbogenerator With End Region Regarding Electrical Losses, Cooling, and Heating," *IEEE Transactions on Energy Conversion*, vol. 26, no. 4, pp. 1073–1080, 2011.

[38] R. Lin, A. Haavisto, and A. Arkkio, "Analysis of Eddy-Current Loss in End Shield and Frame of a Large Induction Machine," *IEEE Transactions on Magnetics*, vol. 46, no. 3, pp. 942–948, 2010.

[39] ——, "Axial Flux and Eddy-Current Loss in Active Region of a Large-Sized Squirrel-Cage Induction Motor," *IEEE Transactions on Magnetics*, vol. 46, no. 11, pp. 3933–3938, 2010.

[40] P. Dular, J. Gyselinck, C. Geuzaine, N. Sadowski, and J. P. A. Bastos, "A 3-D Magnetic Vector Potential Formulation Taking Eddy Currents in Lamination Stacks Into Account," *IEEE Transactions on Magnetics*, vol. 39, no. 3, pp. 1424–1427, 2003.

[41] K. Hollaus and O. Bíró, "Estimation of 3-D eddy currents in conducting laminations by an anisotropic conductivity and a 1-D analytical model," *COMPEL: The International Journal for Computation and Mathematics in Electrical and Electronic Engineering*, vol. 18, no. 3, pp. 494–503, 1999.

[42] K. Muramatsu, T. Okitsu, H. Fujitsu, and F. Shimanoe, "Method of Nonlinear Magnetic Field Analysis Taking Into Account Eddy Current in Laminated Core," *IEEE Transactions on Magnetics*, vol. 40, no. 2, pp. 896–899, 2004.

[43] O. Bíró, K. Preis, and I. Ticar, "A FEM method for eddy current analysis in laminated media," *COMPEL: The International Journal for Computation and Mathematics in Electrical and Electronic Engineering*, vol. 24, no. 1, pp. 241–248, 2005.

[44] R. M. Del Vecchio, "An efficient procedure for modeling complex hysteresis processes in ferromagnetic materials," *IEEE Transactions on Magnetics*, vol. 18, no. 6, pp. 809–811, 1980.

[45] ——, "The calculation of eddy current losses associated with rotating magnetic fields in thin laminations," *IEEE Transactions on Magnetics*, vol. 18, no. 6, pp. 1707–1709, 1982.

[46] L. R. Dupré, R. Van Keer, and J. A. A. Melkebeek, "An Iron Loss Model for Electrical Machines using the Preisach theory," *IEEE Transactions on Magnetics*, vol. 33, no. 5, pp. 4158–4160, 1997.

[47] J. J. C. Gyselinck, L. R. Dupré, L. Vandevelde, and J. A. A. Melkebeek, "Calculation of No-Load Induction Motor Core Losses Using the Rate Dependent Preisach Model," *IEEE Transactions on Magnetics*, vol. 34, no. 6, pp. 3876–3881, 1998.

[48] K. Yamazaki and N. Fukushima, "Torque and Loss Calculation of Rotating Machines Considering Laminated Cores Using Post 1-D Analysis," *IEEE Transactions on Magnetics*, vol. 47, no. 5, pp. 994–997, 2011.

[49] J. Pippuri, "Finite element analysis of eddy current losses in steel laminations of inverter-fed electrical machines," Ph.D. dissertation, Aalto University, School of Science and Technology, Finland, 2010.

[50] A. Belahcen, E. Dlala, and J. Pippuri, "Modelling eddy-current in laminated nonlinear magnetic circuits," *COMPEL: The International Journal for Computation and Mathematics in Electrical and Electronic Engineering*, vol. 30, no. 3, pp. 1082–1091, 2011.

[51] L. Krähenbühl, P. Dular, T. Zeidan, and F. Buret, "Homogenization of Lamination Stacks in Linear Magnetodynamics," *IEEE Transactions on Magnetics*, vol. 40, no. 2, pp. 912–915, 2004.

[52] J. Gyselinck, R. V. Sabariego, and P. Dular, "A Nonlinear Time-Domain Homogenization Technique for Laminated Iron Cores in Three-Dimensional Finite-Element Models," *IEEE Transactions on Magnetics*, vol. 42, pp. 763–766, 2006.

[53] P. Rasilo, E. Dlala, K. Fonteyn, J. Pippuri, A. Belahcen, and A. Arkkio, "Model of Laminated Ferromagnetic Cores for Loss Prediction in Electrical Machines," *IET Electric Power Applications*, vol. 5, no. 7, pp. 580–588, 2011.

[54] P. Rasilo, A. Belahcen, and A. Arkkio, "Experimental determination and numerical evaluation of core losses in a 150-kVA wound-field synchronous machine," *IET Electric Power Applications*, vol. 7, no. 2, pp. 97–105, 2012.

[55] J. Gyselinck, L. Vandevelde, J. Melkebeek, P. Dular, F. Henrotte, and W. Legros, "Calculation of Eddy Currents and Associated Losses in Electrical Steel Laminations," *IEEE Transactions on Magnetics*, vol. 35, no. 3, pp. 1191–1194, 1999.

[56] O. Bottauscio, M. Chiampi, and D. Chiarabaglio, "Magnetic flux distribution and losses in narrow ferromagnetic strips," *Journal of Magnetism and Magnetic Materials*, vol. 215–216, pp. 46–48, 2000.

[57] T. Chevalier, A. Kedous-Lebouc, and B. Cornut, "Influence of electrical sheet width on dynamic magnetic properties," *Journal of Magnetism and Magnetic Materials*, vol. 215–216, pp. 623–625, 2000.

[58] K. Yamazaki and N. Fukushima, "Iron-Loss Modeling for Rotating Machines: Comparison Between Bertotti's Three-Term Expression and 3-D Eddy-Current Analysis," *IEEE Transactions on Magnetics*, vol. 46, no. 8, pp. 3121–3124, 2010.

[59] K. Yamazaki, Y. Yamato, H. Mogi, C. Kaido, A. Nakahara, K. Takahashi, K. Ide, and K. Hattori, "In-plane eddy current analysis for end and interior stator core packets of turbine generators," *COMPEL: The International Journal for Computation and Mathematics in Electrical and Electronic Engineering*, vol. 29, no. 5, pp. 1218–1231, 2010.

[60] F. Preisach, "Über die magnetische Nachwirkung," *Zeitschrift für Physik*, vol. 94, pp. 277–302, 1935.

[61] M. Krasnosel'skii and A. Pokrovskii, *Systems with Hysteresis*, Nauka, 1983.

[62] G. Bertotti, G. Fiorillo, and G. P. Soardo, "The prediction of power losses in soft magnetic materials," *Journal de physique*, vol. 49, pp. 1915–1919, 1988.

[63] E. Della Torre, *Magnetic Hysteresis*, IEEE Press, 1999.

[64] I. D. Mayergoyz, *Mathematical models of hysteresis and their applications*, Elsevier, 2003.

[65] D. H. Everett, "A general approach to hysteresis Part 4. An alternative formulation of the domain model," *Transactions of the Faraday Society*, vol. 51, pp. 1551–1557, 1955.

[66] E. Madelung, "On the magnetization by fast currents and an operation principle of the magnetodetectors of Rutherford-Marconi," *Annalen der Physik*, vol. 17, no. 5, pp. 861–890, 1905.

[67] S. Bobbio and G. Marrucci, "A possible alternative to Preisach's model of static hysteresis," *Il Nuovo Cimento D*, vol. 15, no. 5, pp. 723–733, 1993.

[68] S. Bobbio, G. Miano, C. Serpico, and C. Visone, "Models of Magnetic Hysteresis Based on Play and Stop Hysterons," *IEEE Transactions on Magnetics*, vol. 33, no. 6, pp. 4417–4426, 1997.

[69] T. Matsuo, D. Shimode, Y. Terada, and M. Shimasaki, "Application of Stop and Play Models to the Representation of Magnetic Characteristics of Silicon Steel Sheet," *IEEE Transactions on Magnetics*, vol. 39, no. 3, pp. 1361–1364, 2003.

[70] S. E. Zirka, Y. I. Moroz, P. Marketos, and A. J. Moses, "Congruency-Based Hysteresis Models for Transient Simulation," *IEEE Transactions on Magnetics*, vol. 40, no. 2, pp. 390–399, 2004.

[71] S. E. Zirka, Y. I. Moroz, and E. Della Torre, "Combination Hysteresis Model for Accommodation Magnetization," *IEEE Transactions on Magnetics*, vol. 41, no. 9, pp. 2426–2431, 2005.

[72] D. C. Jiles and D. L. Atherton, "Theory of ferromagnetic hysteresis," *Journal of Magnetism and Magnetic Materials*, vol. 61, no. 1–2, pp. 48–60, 1986.

[73] M. Pasquale, B. Bertotti, D. C. Jiles, and Y. Bi, "Application of the Preisach and Jiles-Atherton models to the simulation of hysteresis in soft magnetic alloys," *Journal of Applied Physics*, vol. 85, no. 8, pp. 4373–4375, 1999.

[74] E. Dlala, "Magnetodynamic vector hysteresis models for steel laminations of rotating electrical machines," Ph.D. dissertation, Helsinki University of Technology, Finland, 2008.

[75] G. Bertotti, "Dynamic Generalization of the Scalar Preisach Model of Hysteresis," *IEEE Transactions on Magnetics*, vol. 28, no. 5, pp. 2599–2061, 1992.

[76] G. Bertotti and M. Pasquale, "Physical Interpretation of Induction and Frequency Dependence of Power Losses in Soft Magnetic Materials," *IEEE Transactions on Magnetics*, vol. 28, no. 5, pp. 2787–2789, 1992.

[77] G. Bertotti, V. Basso, and M. Pasquale, "Application of the Preisach Model to the Calculation of Magnetization Curves and Power Losses in Ferromagnetic Materials," *IEEE Transactions on Magnetics*, vol. 30, no. 2, pp. 1052–1057, 1994.

[78] A. Bergqvist, "On magnetic hysteresis modeling," Ph.D. dissertation, Royal Institute of Technology, Stockholm, Sweden, 1994.

[79] L. R. Dupré, O. Bottauscio, M. Chiampi, M. Repetto, and J. A. A. Melkebeek, "Modeling of Electromagnetic Phenomena in Soft Magnetic Materials Under Unidirectional Time Periodic Flux Excitations," *IEEE Transactions on Magnetics*, vol. 35, no. 5, pp. 4171–4184, 1999.

[80] S. E. Zirka, Y. I. Moroz, P. Marketos, and A. J. Moses, "Viscosity-Based Magnetodynamic Model of Soft Magnetic Materials," *IEEE Transactions on Magnetics*, vol. 42, no. 9, pp. 2121–2132, 2006.

[81] D. C. Jiles, "Frequency Dependence of Hysteresis Curves in "Non-Conducting" Magnetic Materials," *IEEE Transactions on Magnetics*, vol. 29, no. 6, pp. 3490–3492, 1993.

[82] E. C. Stoner and E. P. Wohlfarth, "A Mechanism of Magnetic Hysteresis in Heterogeneous Alloys," *Philosophical Transactions of the Royal Society*, vol. 240, no. 826, pp. 599–642, 1948.

[83] A. A. Adly and I. D. Mayergoyz, "A new vector Preisach-type model of hysteresis," *Journal of Applied Physics*, vol. 73, no. 10, pp. 5824–5826, 1993.

[84] E. Dlala, A. Belahcen, K. A. Fonteyn, and M. Belkasim, "Improving Loss Properties of the Mayergoyz Vector Hysteresis Model," *IEEE Transactions on Magnetics*, vol. 46, no. 3, pp. 918–924, 2010.

[85] T. Matsuo and M. Shimasaki, "Generalization of an Isotropic Vector Hysteresis Model Represented by the Superposition of Stop Models–Identification and Rotational Hysteresis Loss," *IEEE Transactions on Magnetics*, vol. 43, no. 4, pp. 1389–1392, 2007.

[86] J. Oti and E. Della Torre, "A vector moving model of both reversible and irreversible magnetizing processes," *Journal of Applied Physics*, vol. 67, no. 9, pp. 5364–5366, 1990.

[87] A. Bergqvist, "Magnetic vector hysteresis model with dry friction-like pinning," *Physica B*, vol. 233, pp. 342–347, 1997.

[88] F. Henrotte, A. Nicolet, and K. Hameyer, "An energy-based vector hysteresis model for ferromagnetic materials," *COMPEL: The International Journal for Computation*

and Mathematics in Electrical and Electronic Engineering, vol. 25, no. 1, pp. 71–80, 2006.

[89] A. Visintin, *Differential models of hysteresis*, Springer, 1994.

[90] E. Dlala, "A Simplified Iron Loss Model for Laminated Magnetic Cores," *IEEE Transactions on Magnetics*, vol. 44, no. 11, pp. 3169–3172, 2008.

[91] T. Matsuo and M. Miyamoto, "Dynamic and Anisotropic Vector Hysteresis Model Based on Isotropic Vector Play Model for Nonoriented Silicon Steel Sheet," *IEEE Transactions on Magnetics*, vol. 48, no. 2, pp. 215–218, 2012.

[92] E. Dlala, A. Belahcen, J. Pippuri, and A. Arkkio, "Interdependence of Hysteresis and Eddy-Current Losses in Laminated Magnetic Cores of Electrical Machines," *IEEE Transactions on Magnetics*, vol. 46, no. 2, pp. 306–309, 2010.

[93] O. Bottauscio and M. Chiampi, "Laminated core modeling under rotational excitations including eddy currents and hysteresis," *Journal of Applied Physics*, vol. 89, no. 11, pp. 6728–6730, 2001.

[94] F. Henrotte and K. Hameyer, "A Dynamical Vector Hysteresis Model Based on an Energy Approach," *IEEE Transactions on Magentics*, vol. 42, no. 4, pp. 899–902, 2006.

[95] J. J. C. Gyselinck, L. Vandevelde, D. Makaveev, and J. A. A. Melkebeek, "Calculation of No Load Losses in an Induction Motor Using an Inverse Vector Preisach Model and an Eddy Current Loss Model," *IEEE Transactions on Magnetics*, vol. 36, no. 4, pp. 856–860, 2000.

[96] J. Saitz, "Magnetic Field Analysis of Electric Machines Taking Ferromagnetic Hysteresis into Account," Ph.D. dissertation, Helsinki University of Technology, Finland, 2001.

[97] M. Enokizono and N. Soda, "Magnetic Field Analysis by Finite Element Method using Effective Anisotropic Field," *IEEE Transactions on Magnetics*, vol. 31, no. 3, pp. 1793–1796, 1995.

[98] P. P. Silvester and R. P. Gupta, "Effective computational models for anisotropic soft B-H curves," *IEEE Transactions on Magnetics*, vol. 27, no. 5, pp. 3804–3807, 1991.

[99] O. Bíró, S. Außerhofer, K. Preis, and Y. Chen, "A modified elliptic model of anisotropy in nonlinear magnetic materials," *COMPEL: The International Journal for Computation and Mathematics in Electrical and Electronic Engineering*, vol. 29, no. 6, pp. 1482–1492, 2010.

[100] A. A. Adly and A. Hafiz, "Efficient Implementation of Anisotropic Vector Preisach-Type Models Using Coupled Step Functions," *IEEE Transactions on Magnetics*, vol. 43, no. 6, pp. 2962–2964, 2007.

[101] C. Ragusa and M. Repetto, "Accurate analysis of magnetic devices with anisotropic vector hysteresis," *Physica B: Condensed Matter*, vol. 275, pp. 92–98, 2000.

[102] M. Kuczmann, "Simulation of uniaxial anisotropy by vector preisach model," *POLLACK PERIODICA: An International Journal for Engineering and Information Sciences*, vol. 5, no. 2, pp. 97–106, 2010.

[103] E. Cardelli, E. Della Torre, and A. Faba, "Numerical Modeling of Hysteresis in Si-Fe Steels," *IEEE Transactions on Magnetics*, vol. 50, no. 2, pp. 329–332, 2014.

[104] T. Matsuo, "Anisotropic Vector Hysteresis Model Using an Isotropic Vector Play Model," *IEEE Transactions on Magnetics*, vol. 46, no. 8, pp. 3041–3044, 2010.

[105] C. Vernescu-Spornic, A. Kedous-Lebouc, S. A. Spornic, and F. Ossart, "Anisotropic and vector hysteresis model for magnetic materials application to a cubic textured NiFe sheet," *Physica B*, vol. 275, pp. 99–102, 2000.

[106] A. Bergqvist, "Experimental testing of an anisotropic vector hysteresis model," *IEEE Transactions on Magnetics*, vol. 33, no. 5, pp. 4152–4154, 1997.

[107] A. V. Leite, N. Sadowski, P. Kuo-Peng, and J. P. A. Bastos, "A New Anisotropic Vector Hysteresis Model Based on Stop Hysterons," *IEEE Transactions on Magnetics*, vol. 41, no. 5, pp. 1500–1503, 2005.

[108] P. Rasilo, J. Ekström, A. Haavisto, A. Belahcen, and A. Arkkio, "Calorimetric system for measurement of synchronous machine losses," *IET Electric Power Applications*, vol. 6, no. 5, pp. 286–294, 2012.

[109] E. Dlala, O. Bottauscio, M. Chiampi, M. Zucca, A. Belahcen, and A. Arkkio, "Numerical Investigation of the Effects of Loading and Slot Harmonics on the Core Losses of Induction Machines," *IEEE Transactions on Magnetics*, vol. 48, no. 2, pp. 1063–1066, 2012.

[110] A. M. Knight and Y. Zhan, "Identification of Flux Density Harmonics and Resulting Iron Losses in Induction Machines With Nonsinusoidal Supplies," *IEEE Transactions on Magnetics*, vol. 44, no. 6, pp. 1562–1565, 2008.

[111] K. J. Binns, R. Hindmarsch, and B. P. Short, "Effect of skewing slots on flux distribution in induction machines," *Proceedings of the Institution of Electrical Engineers*, vol. 118, pp. 543–549, 1971.

[112] F. Piriou and A. Razek, "A Model for Coupled Magnetic-Electric Circuits in Electric Machines with Skewed Slots," *IEEE Transactions on Magnetics*, vol. 26, no. 2, pp. 1096–1100, 1990.

[113] J. J. C. Gyselinck, L. Vandevelde, and J. A. A. Melkebeek, "Multi-Slice FE Modeling of Electrical Machines With Skewed Slots - The Skew Discretization Error," *IEEE Transactions on Magnetics*, vol. 37, no. 5, pp. 3233–3237, 2001.

[114] B.-I. Kown, B.-T. Kim, C.-S. Jun, and S.-C. Park, "Analysis of Axially Non-uniform Loss Distribution in 3-phase Induction Motor Considering Skew Effect," *IEEE Transactions on Magnetics*, vol. 35, no. 3, pp. 1298–1304, 1999.

[115] S. L. Ho, W. N. Fu, and H. C. Wong, "Estimation of Stray Losses of Skewed Rotor Induction Motors Using and 3-D Time Stepping Finite Element Methods," *IEEE Transactions on Magnetics*, vol. 34, no. 5, pp. 3102–3105, 1998.

[116] C. I. McClay and S. Williamson, "Influence of rotor skew on cage motor losses," *IEE Proceedings - Electric Power Applications*, vol. 145, no. 5, pp. 414–422, 1998.

[117] ——, "The variation of cage motor losses with skew," *IEEE Transactions on Industry Applications*, vol. 36, no. 6, pp. 1563–1570, 2000.

[118] I. Kiss, "Calculation of eddy-current losses in laminated iron core materials of induction machines by FEM," Master's thesis, Budapest University of Technology and Economics, Hungary, 2009.

[119] S. Williamson, C. Y. Poh, and A. S. Smith, "Estimation of the Inter-Bar Resistance of a Cast Cage Rotor," *IEEE Transactions on Industry Applications*, vol. 40, no. 2, pp. 558–564, 2004.

[120] K. Yamazaki and Y. Watanabe, "Interbar Current Analysis of Induction Motors Using 3-D Finite-Element Method Considering Lamination of Rotor Core," *IEEE Transactions on Magnetics*, vol. 42, no. 4, pp. 1287–1290, 2006.

[121] A. Boglietti, P. Ferraris, M. Lazzari, and F. Profumo, "Iron losses in magnetic materials with six-step and PWM inverter supply," *IEEE Transactions on Magnetics*, vol. 27, no. 6, pp. 5334–5336, 1991.

[122] A. Boglietti, O. Bottauscio, M. Chiampi, M. Pastorelli, and M. Repetto, "Computation and measurement of iron losses under PWM supply conditions," *IEEE Transactions on Magnetics*, vol. 32, no. 5, pp. 4302–4303, 1996.

[123] A. Boglietti, M. Chiampi, M. Repetto, O. Bottauscio, and D. Chiarabaglio, "Loss Separation Analysis in Ferromagnetic Sheets under PWM Inverter Supply," *IEEE Transactions on Magnetics*, vol. 34, no. 4, pp. 1240–1242, 1998.

[124] A. Boglietti, P. Ferraris, and M. Lazzari, "Induction Motor Iron Losses Measurement with a Static Converter Supply using a Slotless Rotor Test Bench," *IEEE Transactions on Magnetics*, vol. 30, no. 6, pp. 4599–4601, 1994.

[125] A. Boglietti, P. Ferraris, M. Lazzari, and M. Pastorelli, "Influence of the Inverter Characteristics on the Iron Losses in PWM Inverter-Fed Induction Motors," *IEEE Transactions on Industry Applications*, vol. 32, no. 5, pp. 1190–1994, 1996.

[126] M. Amar and R. Kaczmarek, "A General Formula for Prediction of Iron Losses Under Nonsinusoidal Voltage Waveform," *IEEE Transactions on Magnetrics*, vol. 31, no. 5, pp. 2504–2509, 1995.

[127] M. Popescu, D. M. Ionel, A. Boglietti, A. Cavagnino, C. Cossar, and M. I. McGilp, "A General Model for Estimating the Laminated Steel Losses Under PWM Voltage Supply," *IEEE Transactions on Industry Applications*, vol. 46, no. 4, pp. 1389–1396, 2010.

[128] R. Kaczmarek, M. Amar, and F. Protat, "Iron Loss Under PWM Voltage Supply on Epstein Frame and in Induction Motor Core," *IEEE Transactions on Magnetics*, vol. 32, no. 1, pp. 189–194, 1996.

[129] A. Boglietti, A. Cavagnino, D. M. Ionel, M. Popescu, D. A. Staton, and S. Vaschetto, "A General Model to Predict the Iron Losses in PWM Inverter-Fed Induction Motors," *IEEE Transactions on Industry Applications*, vol. 46, no. 5, pp. 1882–1890, 2010.

[130] O. Bottauscio, A. Canova, M. Chiampi, and M. Repetto, "Rotational hysteresis and eddy current losses in electrical motor stators under non-conventional supply," *Journal of Magnetism and Magnetic Materials*, vol. 254–255, pp. 241–243, 2003.

[131] J. Pippuri and A. Arkkio, "Time-Harmonic Induction-Machine Model Including Hysteresis and Eddy Currents in Steel Laminations," *IEEE Transactions on Magnetics*, vol. 45, no. 7, pp. 2981–2989, 2009.

[132] K. Yamazaki and N. Fukushima, "Iron Loss Model for Rotating Machines Using Direct Eddy Current Analysis in Electrical Steel Sheets," *IEEE Transactions on Energy Conversion*, vol. 25, no. 3, pp. 633–641, 2010.

[133] E. Dlala and A. Arkkio, "A General Model for Investigating the Effects of the Frequency Converter on the Magnetic Iron Losses of a Squirrel-Cage Induction Motor," *IEEE Transactions on Magnetics*, vol. 45, no. 9, pp. 3303–3315, 2009.

[134] Z. Gmyrek, A. Boglietti, and A. Cavagnino, "Estimation of Iron Losses in Induction Motors: Calculation Method, Results, and Analysis," *IEEE Transactions on Industrial Electronics*, vol. 57, no. 1, pp. 161–171, 2010.

[135] A. Schoppa, J. Schneider, and J.-O. Roth, "Influence of the cutting process on the magnetic properties of non-oriented electrical steels," *Journal of Magnetism and Magnetic Materials*, vol. 215–216, pp. 100–102, 2000.

[136] A. Kedous-Lebouc, B. Cornut, J. C. Perrier, P. Manfé, and T. Chevalier, "Punching influence on magnetic properties of the stator teeth of an induction motor," *Journal of Magnetism and Magnetic Materials*, vol. 254–255, pp. 124–126, 2003.

[137] K. H. Schmidt, "Influence of punching on the magnetic properties of electric steel with 1 % silicon," *Journal of Magnetism and Magnetic Materials*, vol. 2, no. 1–3, pp. 136–150, 1976.

[138] A. Belhadj, P. Baudouin, F. Breaban, A. Deffontaine, M. Dewulf, and Y. Houbaert, "Effect of laser cutting on microstructure and on magnetic properties of grain non-

oriented electrical steels," *Journal of Magnetism and Magnetic Materials*, vol. 256, pp. 20–31, 2003.

[139] F. Ossart, E. Hug, O. Hubert, C. Buvat, and R. Billardon, "Effect of Punching on Electrical Steels: Experimental and Numerical Coupled Analysis," *IEEE Transactions on Magnetics*, vol. 36, no. 5, pp. 3137–3140, 2000.

[140] M. Bali, H. De Gersem, and A. Muetze, "Finite-Element Modeling of Magnetic Material Degradation Due to Punching," *IEEE Transactions on Magnetics*, vol. 50, no. 2, pp. 745–748, 2014.

[141] K. Fujisaki, R. Hirayama, T. Kawachi, S. Satou, C. Kaidou, M. Yabumoto, and T. Kubota, "Motor Core Iron Loss Analysis Evaluating Shrink Fitting and Stamping by Finite-Element Method," *IEEE Transactions on Magnetics*, vol. 43, no. 5, pp. 1950–1954, 2007.

[142] K. Yamazaki and Y. Kato, "Iron Loss Analysis of Interior Permanent Magnet Synchronous Motors by Considering Mechanical Stress and Deformation of Stators and Rotors," *IEEE Transactions on Magnetics*, vol. 50, no. 2, pp. 909–912, 2014.

[143] Y. Kai, Y. Tsuchida, T. Todaka, and M. Enokizono, "Influence of Stress on Vector Magnetic Property Under Alternating Magnetic Flux Conditions," *IEEE Transactions on Magnetics*, vol. 47, no. 10, pp. 4344–4347, 2011.

[144] A. Belahcen, K. Fonteyn, R. Kouhia, P. Rasilo, and A. Arkkio, "Magnetomechanical coupled FE simulations of rotating electrical machines," *COMPEL: The International Journal for Computation and Mathematics in Electrical and Electronic Engineering*, vol. 32, no. 5, pp. 1484–1499, 2013.

[145] P. Beckley, *Electrical Steels for Rotating Machines*, The Institution of Engineering and Technology, 2002.

[146] A. C. Beiler and P. L. Schmidt, "Interlaminar Eddy Current Losses in Laminated Cores," *Transactions of the American Institute of Electrical Engineers*, vol. 66, pp. 872–78, 1947.

[147] C. A. Schulz, S. Duchesne, D. Roger, and J.-N. Vincent, "Capacitive short circuit detection in transformer core laminations," *Journal of Magnetism and Magnetic Materials*, vol. 320, pp. 911–914, 2008.

[148] R. Romary, S. Jelassi, and J. F. Brudny, "Stator-Interlaminar-Fault Detection Using an External-Flux-Density Sensor," *IEEE Transactions on Industrial Electronics*, vol. 57, no. 1, pp. 237–243, 2010.

[149] A. J. Moses and M. Aimoniotis, "Effects of Artificial Edge Burrs on the Properties of a Model Transformer Core," *Physica Scripta*, vol. 39, pp. 391–393, 1989.

[150] R. Mazurek, P. Marketos, A. Moses, and J.-N. Vincent, "Effect of Artificial Burrs on the Total Power Loss of a Three-Phase Transformer Core," *IEEE Transactions on Magnetics*, vol. 46, no. 2, pp. 638–641, 2010.

[151] R. Mazurek, H. Hamzehbahmani, A. Moses, P. I. Anderson, F. J. Anayi, and T. Belgrand, "Effect of Artificial Burrs on Local Power Loss in a Three-Phase Transformer Core," *IEEE Transactions on Magnetics*, vol. 48, no. 4, pp. 1653–1656, 2012.

[152] C. A. Schulz, D. Roger, S. Duchesne, and J.-N. Vincent, "Experimental Characterization of Interlamination Shorts in Transformer Cores," *IEEE Transactions on Magnetics*, vol. 46, no. 2, pp. 614–617, 2010.

[153] J.-P. Bielawski, S. Duchesne, D. Roger, C. Demian, and T. Belgrand, "Contribution to the Study of Losses Generated by Interlaminar Short-Circuits," *IEEE Transactions on Magnetics*, vol. 48, no. 4, pp. 1397–1400, 2012.

[154] A. Schoppa, J. Schneider, C.-D. Wuppermann, and T. Bakon, "Influence of welding and sticking of laminations on the magnetic properties of non-oriented electrical steels," *Journal of Magnetism and Magnetic Materials*, vol. 254–255, pp. 367–369, 2003.

[155] A. Krings, S. Nategh, O. Wallmark, and J. Soulard, "Influence of the Welding Process on the Performance of Slotless PM Motors With SiFe and NiFe Stator Laminations," *IEEE Transactions on Industry Applications*, vol. 50, no. 1, pp. 296–306, 2014.

[156] M. C. Marion-Pera, A. Kedous-Lebouc, T. Waeckerle, and B. Cornut, "Characterization of SiFe Sheet Insulation," *IEEE Transactions on Magnetics*, vol. 31, no. 4, pp. 2408–2415, 1995.

[157] K. Yamazaki and A. Abe, "Loss Investigation of Interior Permanent-Magnet Motors Considering Carrier Harmonics and Magnet Eddy Currents," *IEEE Transactions on Industry Applications*, vol. 45, no. 2, pp. 659–665, 2009.

[158] P. Rasilo, A. Belahcen, and A. Arkkio, "Importance of iron-loss modeling in simulation of wound-field synchronous machines," *IEEE Transactions on Magnetics*, vol. 48, no. 9, pp. 2495–2504, 2012.

[159] E. Dlala and A. Arkkio, "Analysis of the Convergence of the Fixed-Point Method Used for Solving Nonlinear Rotational Magnetic Field Problems," *IEEE Transactions on Magnetics*, vol. 44, no. 4, pp. 473–478, 2008.

[160] P. Weiss, "The hypothesis of the molecular field and the property of ferromagnetism," *Journal de Physique*, vol. 6, pp. 661–690, 1907.

[161] M. Kornetzki and I. Lucas, "Zur Theorie der Hystereseverluste im magnetischen Drehfeld," *Zeitschrift für Physik*, vol. 142, pp. 70–82, 1955.

[162] Z. Neuschl, "Computer aided experimental methods for determination of load independent iron losses in permanent magnet electrical machines with additionaly axialflux," Ph.D. dissertation, Brandenburg University of Technology, 2007.

[163] O. Bíró and K. R. Richter, "CAD in Electromagnetism," *Advances in Electronics and Electron Physics*, vol. 82, pp. 1–96, 1991.

[164] O. Bíró, "Edge element formulations of eddy current problems," *Computer Methods in Applied Mechanics and Engineering*, vol. 169, no. 3–4, pp. 391–405, 1999.

[165] J. Jin, *The finite element method in electromagnetics*, John Wiley & Sons, Inc., 2002.

[166] O. Bíró and K. Preis, "On the Use of the Magnetic Vector Potential in the Finite Element Analysis of Three-Dimensional Eddy Currents," *IEEE Transactions on Magnetics*, vol. 25, no. 4, pp. 3145–3159, 1989.

[167] I. Bakhsh, O. Bíró, and K. Preis, "Skin Effect Problems with Prescribed Current Condition," in *Proceedings of the 14th International IGTE Symposium on Numerical Field Calculation in Electrical Engineering*, 2010.

[168] O. Bíró, K. Preis, and K. R. Richter, "On the Use of the Magnetic Vector Potential in the Nodal and Edge Finite Element Analysis of 3D Magnetostatic Problems," *IEEE Transactions on Magnetics*, vol. 32, no. 3, pp. 651–654, 1996.

[169] R. Albanese and G. Rubinacci, "Solution of three dimensional eddy current problems by integral and differential methods," *IEEE Transactions on Magnetics*, vol. 24, no. 1, pp. 98–101, 1988.

[170] P. J. Leonard, R. J. Hill-Cottingham, and D. Rodger, "3D Finite Element Models and External Circuits using the $\mathbf{A}\psi$ Scheme with Cuts," *IEEE Transactions on Magnetics*, vol. 30, no. 5, pp. 3220–3223, 1994.

[171] F. Henrotte and K. Hameyer, "An Algorithm to Construct the Discrete Cohomology Basis Functions Required for Magnetic Scalar Potential Formulations Without Cuts," *IEEE Transactions on Magnetics*, vol. 39, no. 3, pp. 1167–1170, 2003.

[172] SAS IP, *ANSYS 13.0 Documentation*, 2010.

[173] A. Arkkio, "Analysis of Induction Motors Based on the Numerical Solution of the Magnetic Field and Circuit Equations," Ph.D. dissertation, Helsinki University of Technology, Finland, 1987.

[174] S. J. Salon, D. W. Burow, R. E. Ashley, L. Ovacik, and M. J. DeBortoli, "Finite Element Analysis of Induction Machines in the Frequency Domain," *IEEE Transactions on Magnetics*, vol. 29, no. 2, pp. 1438–1441, 1993.

[175] A. Stermecki, O. Bíró, K. Preis, S. Rainer, and G. Ofner, "Numerical analysis of steady-state operation of three-phase induction machines by an approximate frequency domain technique," *Elektrotechnik & Informationstechnik*, vol. 128, no. 3, pp. 81–85, 2011.

[176] G. Paoli and O. Bíró, "Time harmonic eddy currents in non-linear media," *COMPEL: The International Journal for Computation and Mathematics in Electrical and Electronic Engineering*, vol. 17, no. 5–6, pp. 567–575, 1998.

[177] N. A. Demerdash and D. Gillott, "A new approach for determination of eddy currents and flux penetration in nonlinear ferromagnetic materials," *IEEE Transactions on Magnetics*, vol. 10, no. 3, pp. 682–685, 1974.

[178] B. Davat, Z. Ren, and M. Lajoie-Mazenc, "The movement in field modeling," *IEEE Transactions on Magnetics*, vol. 21, no. 6, pp. 2296–2298, 1985.

[179] F. Rapetti, F. Bouillault, L. Santandrea, A. Buffa, Y. Maday, and A. Razek, "Calculation of Eddy Currents with Edge Elements on Non-Matching Grids in Moving Structures," *IEEE Transactions on Magnetics*, vol. 36, no. 4, pp. 1351–1355, 2000.

[180] R. Perrin-Bit and J. L. Coulomb, "A Three Dimensional Finite Element Mesh Connection for Problems Involving Movement," *IEEE Transactions on Magnetics*, vol. 31, no. 3, pp. 1920–1923, 1995.

[181] F. Bouillault, A. Buffa, Y. Maday, and F. Rapetti, "The mortar edge element method in three dimensions: application to magnetostatics," *SIAM Journal on Scientific Computing*, vol. 24, no. 4, pp. 1303–1327, 2003.

[182] E. Dlala, "Efficient Algorithms for the Inclusion of the Preisach Hysteresis Model in Nonlinear Finite-Element Methods," *IEEE Transactions on Magnetics*, vol. 47, no. 2, pp. 395–408, 2011.

[183] J. Füzi, "Analytical Approximation of Preisach Distribution Functions," *IEEE Transactions on Magnetics*, vol. 39, no. 3, pp. 1357–1360, 2003.

[184] W. Roshen, "Ferrite Core Loss for Power Magnetic Components Design," *IEEE Transactions on Magnetics*, vol. 27, no. 6, pp. 4407–4415, 1991.

[185] S. R. Naidu, "Simulation of the hysteresis phenomenon using Preisach's theory," *IEE Proceedings Part A*, vol. 137, no. 2, pp. 73–79, 1990.

[186] Z. Szabó, I. Tugyi, G. Kádár, and J. Füzi, "Identification procedures for scalar Preisach model," *Physica B*, vol. 343, pp. 142–147, 2004.

[187] E. Cardelli, E. Della Torre, and G. Ban, "Experimental determination of Preisach distribution functions in magnetic cores," *Physica B*, vol. 275, pp. 262–269, 2000.

[188] N. Takahashi, S. Miyabara, and K. Fujiwara, "Problems in Praetical Finite Element Analysis Using Preisach Hysteresis Model," *IEEE Transactions on Magnetics*, vol. 35, no. 2, pp. 1243–1246, 1999.

[189] M. Kuczmann, "Identification of the 2D vector Preisach hysteresis model," *COMPEL: The International Journal for Computation and Mathematics in Electrical and Electronic Engineering*, vol. 30, no. 2, pp. 538–551, 2011.

[190] E. Dlala, "Comparison of Models for Estimating Magnetic Core Losses in Electrical Machines Using the Finite-Element Method," *IEEE Transactions on Magnetics*, vol. 45, no. 2, pp. 716–725, 2009.

[191] K. Atallah and D. Howe, "Calculation of the rotational power loss in electrical steel laminations from measured H and B," *IEEE Transactions on Magnetics*, vol. 29, no. 6, pp. 3547–3549, 1993.

[192] *IEC 60404-2 Magnetic materials. Part 2: Methods of measurement of the magnetic properties of electrical steel sheet and strip by means of an Epstein frame*, International Electrotechnical Comission Std., 2008.

[193] *IEC 60404-10 Magnetic materials. Part 10: Methods of measurement of magnetic properties of magnetic sheet and strip at medium frequencies*, International Electrotechnical Comission Std., 1988.

[194] V. Goričan, M. Jesenik, A. Hamler, B. Štumberger, and M. Trlep, "Measurement of 2-d magnetic properties of grain oriented silicon steel sheet using RRSST," in *Proceedings of the 11th Symposium on Electromagnetic Fields in Mechatronics, Electrical and Electronic Engineering (ISEF)*, 2003.

[195] V. Goričan, A. Hamler, B. Hribernik, M. Jesenik, and M. Trlep, "2-D measurements of magnetic properties using a round RSST," in *Proceedings of the 6th International Workshop on 1&2-Dimensional Magnetic Measurement and Testing*, 2000.

[196] E. Cardelli and A. Faba, "Vector hysteresis measurements of not oriented grain SiFe steels by a biaxial hall sensors array," *Physica B*, vol. 435, pp. 34–39, 2014.

[197] M. Belkasim, "Identification of loss models from measurements of the magnetic properties of electrical steel sheets," Master's thesis, Helsinki University of Technology, Finland, 2008.

[198] J. F. Gieras, *Noise of Polyphase Electric Motors*, Taylor & Francis, 2006.

[199] S. Rainer, O. Bíró, A. Stermecki, and B. Weilharter, "Frequency Domain Evaluation of Transient Finite Element Simulations of Induction Machines," *IEEE Transactions on Magnetics*, vol. 48, no. 8, pp. 851–854, 2012.

[200] Mathworks, *MATLAB R2012a Documentation*, 2012.

[201] Z. Yu, "Space-Vector PWM With TMS320C24x/F24x Using Hardware and Software Determined Switching Patterns," Texas Instruments, Tech. Rep., 1999.

[202] P. Handgruber, G. Ofner, and R. Seebacher, "Harmonic emissions of doubly fed induction machines for wind power plants," in *Proceedings of the 15th International Symposium on Electromagnetic Fields in Mechatronics, Electrical and Electronic Engineering (ISEF)*, 2011.

[203] O. König, "Modeling of a Doubly Fed Induction Generator for Wind Power Plants," Master's thesis, Graz University of Technology, Austria, 2009.

[204] B. Weilharter, O. Bíró, S. Rainer, and A. Stermecki, "Computation of Rotating Force Waves in Skewed Induction Machines Using Multi-Slice Models," *IEEE Transactions on Magnetics*, vol. 47, no. 5, pp. 1046–1049, 2011.

D List of Publications

[P1] P. Handgruber, A. Stermecki, O. Bíró, A. Belahcen, and E. Dlala, "3-D Eddy Current Analysis in Steel Laminations of Electrical Machines as a Contribution for Improved Iron Loss Modeling," in *Proceedings of the 20th International Conference on Electrical Machines (ICEM)*, 2012.

[P2] ——, "3-D Eddy Current Analysis in Steel Laminations of Electrical Machines as a Contribution for Improved Iron Loss Modeling," *IEEE Transactions on Industry Applications*, vol. 49, no. 5, pp. 2033–2036, 2013.

[P3] P. Handgruber, A. Stermecki, O. Bíró, V. Goričan, E. Dlala, and G. Ofner, "Anisotropic Generalization of Vector Preisach Hysteresis Models for Non-Oriented Steels," in *Proceedings of the 16th Biennial IEEE Conference on Electromagnetic Field Computation (CEFC)*, 2014.

[P4] ——, "Anisotropic Generalization of Vector Preisach Hysteresis Models for Non-Oriented Steels," *IEEE Transactions on Magnetics*, vol. 51, no. 3, 2015, in press.

[P5] P. Handgruber, A. Stermecki, O. Bíró, and G. Ofner, "Frequency Domain Decomposition of 3-D Eddy Current Problems in Steel Laminations of Induction Machines," in *Proceedings of the 19th Conference on the Computation of Electromagnetic Fields (COMPUMAG)*, 2014.

[P6] ——, "Frequency Domain Decomposition of 3-D Eddy Current Problems in Steel Laminations of Induction Machines," *IEEE Transactions on Magnetics*, vol. 50, no. 2, pp. 901–904, 2014.

[P7] ——, "Three-Dimensional Eddy Current Loss Modeling in Steel Laminations of Skewed Induction Machines," in *Proceedings of the 15th Biennial IEEE Conference on Electromagnetic Field Computation (CEFC)*, 2012.

[P8] ——, "Three-Dimensional Eddy Current Loss Modeling in Steel Laminations of Skewed Induction Machines," *IEEE Transactions on Magnetics*, vol. 49, no. 5, pp. 2033–2036, 2012.

[P9] P. Handgruber, S. Schernthanner, A. Stermecki, O. Bíró, and G. Ofner, "Effects of Inverter Supply on the Iron Loss Characteristics of Doubly Fed Induction Machines," in *Proceedings of the 16th International IGTE Symposium*, 2014.

[P10] P. Handgruber, A. Stermecki, O. Bíró, and G. Ofner, "Additional Eddy Current Losses in Induction Machines Due to Interlaminar Short Circuits," in *Proceedings of the 15th International IGTE Symposium*, 2012.

[P11] ——, "Evaluation of Interlaminar Eddy Currents in Induction Machines," in *Proceedings of the 39th Annual Conference of the IEEE Industrial Electronics Society (IECON)*, 2013.